

ISOLATION ENHANCEMENT TECHNIQUES FOR PRINTED MIMO ANTENNA SYSTEMS

BY

AHMED BILAL NUMAN

A Thesis Presented to the
DEANSHIP OF GRADUATE STUDIES

KING FAHD UNIVERSITY OF PETROLEUM & MINERALS

DHAHRAN, SAUDI ARABIA

In Partial Fulfillment of the
Requirements for the Degree of

MASTER OF SCIENCE

In

ELECTRICAL ENGINEERING DEPARTMENT

APRIL 2013

KING FAHD UNIVERSITY OF PETROLEUM & MINERALS
DHAHRAN 31261, SAUDI ARABIA

DEANSHIP OF GRADUATE STUDIES

This thesis, written by **AHMED BILAL NUMAN** under the direction of his thesis adviser and approved by his thesis committee, has been presented to and accepted by the Dean of Graduate Studies, in partial fulfillment of the requirements for the degree of **MASTER OF SCIENCE IN ELECTRICAL ENGINEERING DEPARTMENT**.

Thesis Committee

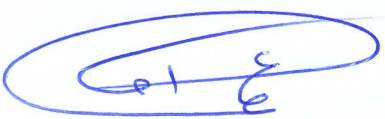

Dr. M. S. Sharawi (Adviser)

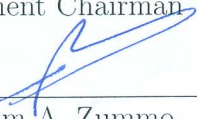
(Co-adviser)


Dr. M. A. Alsunaidei (Member)


Dr. S. S. Iqbal (Member)

(Member)


Dr. Ali Ahmad Al-Shaikhi
Department Chairman


Dr. Salam A. Zummo
Dean of Graduate Studies

9/4/18
Date



©Ahmed Bilal Numan
2013

To Ammi Jaan

ACKNOWLEDGMENTS

With the name of Allah, the most Beneficent, the most Merciful
Blessings and grace on Prophet Muhammad, Ahl-e-bayt, Companions of Prophet
and anyone who follows him.

First of all, I would like to thank my family, especially my mother, for their
support and prayers. Without their prayers, I would not have been able to get
admit in an international institute to earn a post-graduate degree.

I would also like to thank Dr. Mohammad S. Sharawi for allowing me to
pursue my masters thesis with him and providing complete support and guidance
to accomplish my thesis requirements. It was a nice experience to work under
his supervision because he was completely involved in my work and we never lost
track throughout my thesis work. In addition to his technical support, I would
like to specifically thank him for his effort to improve my writing and presentation
skills. In addition to my supervisor, I would also like to thank my thesis committee
members, Dr. Mohammad Abdul Aziz Alsunaidi and Dr. Sheikh Sharif Iqbal to
rigorously review and improve my thesis work.

TABLE OF CONTENTS

LIST OF TABLES	vii
LIST OF FIGURES	viii
LIST OF ABBREVIATIONS	xii
ABSTRACT (ENGLISH)	xiv
ABSTRACT (ARABIC)	xvii
CHAPTER 1 INTRODUCTION	1
1.1 Multiple Antenna Technologies	1
1.2 MIMO Technology	4
1.3 Antenna Systems for MIMO	8
1.4 Design Challenges for MIMO Antenna Systems	9
1.5 Thesis Contributions	10
1.6 Thesis Outline	12
CHAPTER 2 PERFORMANCE METRICS FOR MIMO AN-	
TENNA SYSTEMS	13
2.1 Isolation	14
2.2 Correlation Coefficient	15
2.3 Mean Effective Gain (MEG)	18
2.4 Total Active Reflection Coefficient (TARC)	21
2.5 Channel Capacity	22

2.6	Diversity Gain	25
2.7	Antenna Size, Gain and Efficiency	25
2.8	Summary	26
CHAPTER 3 LITERATURE REVIEW		28
3.1	Antenna configurations	29
3.2	Decoupling Networks	32
3.3	Parasitic Elements	34
3.4	Defected Ground-plane Structures (DGS)	37
3.5	Neutralization Line	43
3.6	Metamaterials	45
3.7	Summary	50
CHAPTER 4 THE 4-SHAPED REFERENCE MIMO ANTENNA SYSTEM		51
4.1	4-Shaped MIMO Antenna System	52
4.2	Characteristics of the 4-Shaped MIMO Antenna System	53
4.3	Isolation Enhancement for the 4-Shaped MIMO Antenna System	60
4.4	Summary	61
CHAPTER 5 NON-METAMATERIAL BASED ISOLATION ENHANCEMENT STRUCTURES		62
5.1	Requirements for an Isolation Enhancement Structure	63
5.2	Design of the DGS based Isolation Enhancement Structure	64
5.2.1	Test Setup	64
5.2.2	Parametric Analysis of Proposed DGS	65
5.2.3	MIMO Antenna System with Proposed DGS	71
5.2.4	Results and Discussion	72
5.3	Neutralization Line (NL) based Isolation Enhancement Structure	80
5.3.1	MIMO Antenna System with NL Based Isolation Enhancement Structure	81

5.3.2	Results and Discussion	81
5.4	Summary	87
CHAPTER 6 METAMATERIAL BASED ISOLATION EN-		
HANCEMENT STRUCTURES		90
6.1	Introduction to Metamaterials	90
6.2	Design of an Isolation Enhancement Structure using Capacitively Loaded Loop (CLL) based Metamaterial	92
6.2.1	Selection of the Unit Element(UE)	92
6.2.2	The Proposed CLL UE	93
6.2.3	Dispersion Diagram for UE	93
6.2.4	Parametric Analysis of the Proposed UE	104
6.2.5	Test Setup for the Proposed Structure	106
6.2.6	MIMO Antenna System with Metamaterial based Isolation Enhancement Structure	110
6.3	Magnetic Wall based Isolation Enhancement structure	118
6.3.1	UE for Magnetic Wall	119
6.3.2	MIMO Antenna System with Magnetic Wall	121
6.3.3	Results and Discussion	121
6.4	Comparison between the proposed isolation methods	125
6.5	Summary	128
CHAPTER 7 CONCLUSIONS AND FUTURE WORK		130
7.1	Future Work	133
REFERENCES		134
VITAE		144

LIST OF TABLES

4.1	Summary for Model_A performance parameters	60
5.1	Summary for Model_B performance parameters	79
5.2	Summary for Model_C performance parameters	88
6.1	Summary for Model_D performance parameters	119
6.2	Summary for Model_E performance parameters	125
6.3	Antenna parameters comparison	127

LIST OF FIGURES

1.1	Block Diagram for MIMO Systems.	4
1.2	Effect of correlation on channel capacity	9
3.1	Summary of the literature review and work contribution region. .	49
4.1	Simulation model for Model_A.	52
4.2	Fabricated prototype for Model_A, (a) Top side (b) Bottom side .	53
4.3	Low band S-parameters for Model_A.	54
4.4	High band S-parameters for Model_A.	54
4.5	Low band TARC for Model_A.	55
4.6	High band TARC for Model_A.	56
4.7	Low band correlation coefficient for Model_A.	57
4.8	High band correlation coefficient for Model_A.	57
4.9	Current distribution for Model_A at 775MHz.	58
4.10	Current distribution for Model_A at 2.55GHz.	58
4.11	Measured gain patterns for Model_A, Dots:vertical polariza- tion for element 1, Circles:vertical polarization for element 2, Solid:horizontal element 1, Dashes:horizontal polarization element 2.	59
5.1	Test setup for DGS	65
5.2	Effect of the DGS length on the stop band frequency; pri- mary rectangles= $6.67 \times 6.67mm^2$; auxiliary rectangle= $7 \times 16mm^2$; width= $4.5mm$	66

5.3	Effect of the DGS width on the stop band frequency; primary rectangles= $6.67 \times 6.67mm^2$; auxiliary rectangle= $7 \times 16mm^2$; length= $40mm$	66
5.4	Effect of the primary rectangle size on the stop band frequency; auxiliary rectangle= $7 \times 16mm^2$; width= $4.5mm$; length= $40mm$. . .	67
5.5	Effect of the auxiliary rectangle size on the stop band frequency; primary rectangles= $6.67 \times 6.67mm^2$; length= $40mm$; width= $4.5mm$..	69
5.6	Behaviour of spiral loaded modified DGS; primary rectangles= $6.67 \times 6.67mm^2$; auxiliary rectangle= $7 \times 16mm^2$; length= $40mm$; width= $4.5mm$	70
5.7	Simulation model for Model_B.	71
5.8	Fabricated prototype for Model_B (a)Top (b)Bottom.	72
5.9	Low band S-parameters for Model_B.	73
5.10	High band S-parameters for Model_B.	73
5.11	Low band TARC for Model_B.	74
5.12	High band TARC for Model_B.	75
5.13	Low band correlation coefficient for Model_B.	75
5.14	High band correlation coefficient for Model_B.	76
5.15	Current distribution for Model_B at $820MHz$	77
5.16	Current distribution for Model_B at $2.65GHz$	77
5.17	Measured gain patterns for Model_B. Dots:vertical polarization for element 1, Circles:vertical polarization for element 2, Solid:horizontal element 1, Dashes:horizontal polarization element 2.	78
5.18	Antenna model with neutralization line (Model_C)	82
5.19	Low band S-parameters for Model_C.	83
5.21	Current distribution at $2.54GHz$, (a) Model_A (b) Model_C . . .	84
5.20	High band S-parameters for Model_C.	84
5.22	Response of Model_C at $774MHz$, Hax= $10mm$, (a) Current distribution (b) S-parameters	85

5.23	Response of Model_C at $774MHz$, $H_{ax}=15mm$, (a) Current distribution (b) S-parameters	86
5.24	Response at of Model_C $774MHz$, $H_{ax}=20mm$, (a) Current distribution (b) S-parameters	86
6.1	Unit Element with [ABCD] parameters [57]	96
6.2	Circuit equivalent model for unit element [57]	99
6.3	Typical dispersion diagram for unbalanced metamaterial unit element [57]	100
6.4	Brillouin Zone (a) and irreducible (first) brillouin zone (b)	104
6.5	UE (top) and Brillouin Zone and irreducible Brillouin Zone (bottom) for metamaterial	105
6.6	Effect of spacing on the fundamental mode; $UL=9, UW=4.5$, edges=27	106
6.7	Effect of structure size on the first mode; spacing= $0.15mm$; spiral edges=27	107
6.9	Test setup for metamaterial.	107
6.8	Effect of spiral edges on the fundamental mode; $UL=9mm$; Gap= $0.15mm$	108
6.10	Transmission coefficient of the test setup.	109
6.11	Dispersion diagrams for the proposed structures (a) High band (b) Low band	110
6.12	Simulation model for Model_D	111
6.13	Fabricated prototype for Model_D, (a) Top side (b) Bottom side. .	111
6.14	Low band S-parameters for Model_D.	112
6.15	High band S-parameters for Model_D.	113
6.16	Low band TARC for Model_D.	113
6.17	High band TARC for Model_D.	114
6.18	Low band Correlation coefficient for Model_D.	114
6.19	High band Correlation coefficient for Model_D.	115

6.20	Current distribution for Model_D at $840MHz$	116
6.21	Current distribution for Model_D at $2.85GHz$	116
6.22	Measured gain patterns for Model_D. Dots:vertical polarization for element 1, Circles:vertical polarization for element 2, Solid:horizontal element 1, Dashes:horizontal polarization element 2.	118
6.23	UE for the magnetic wall[43].	120
6.24	Simulation model for Model_E.	122
6.25	Low band S-parameters for Model_E.	122
6.26	High band S-parameters for Model_E.	123
6.27	Magnetic field distribution between 4-shaped radiators at $2.54GHz$.	124

LIST OF ABBREVIATIONS

CDF	Cumulative Distribution Function
CLL	Capacitively Loaded Loop
CPDF	Cumulative probability Distribution Function
DGS	Defected Ground Structure
FCC	Federal Communication Commission
HFSS	High Frequency Structure Simulator
IFA	Inverted F Antennas
LH	Left Hand
LoS	Line of Sight
MEG	Mean Effective Gain
MIMO	Multiple Input Multiple Output
MISO	Multiple Input Single Output
NL	Neutralization Line
NLoS	Non-Line of Sight

OCSR	Open Complementary Split Ring Resonator
PIFA	Planar Inverted F Antennas
RH	Right Hand
SIMO	Single Input Multiple Output
SNR	Signal to Noise Ratio
SRR	Split Ring Resonator
TARC	Total Active Reflection Coefficient
UC	Unit Cell
UE	Unit Element
UMTS	Universal Mobile Telecommunications System
UWB	Ultra Wide Band
VNA	Vector Network Analyzer
WiMax	Worldwide Interoperability for Microwave Access
WLAN	Wireless Local Area Network

THESIS ABSTRACT

NAME: Ahmed Bilal Numan

TITLE OF STUDY: Isolation Enhancement Techniques for Printed MIMO Antenna Systems

MAJOR FIELD: Electrical Engineering Department

DATE OF DEGREE: April 2013

The performance of a Multiple-Input-Multiple-Output (MIMO) system relies on the multiple channels that are established between the multiple radiating elements of the transmitter and the receiver. If the multiple radiators in a MIMO antenna system are highly coupled with each other then the whole antenna system will merely act as an antenna array. Thus the radiators of a MIMO antenna system should be strongly decoupled so that the signals from the radiating elements are different and independent from each other. These independent signals exhibit low correlation to utilize the benefits of MIMO technology.

In this work, isolation enhancement structures are designed for printed MIMO antenna systems. The isolation structures are based on the defected ground structure (DGS), neutralization line, metamaterials and a magnetic wall. The isolation

structures are applied to a 4-shaped, dual-band and dual-element printed MIMO antenna system. This antenna system resonates at two bands centered approximately at 800MHz and 2.7GHz, respectively. The antenna system suffers from low isolation levels in both bands that is not acceptable for MIMO applications. And thus, the isolation enhancement structures are investigated to improve its performance.

The DGS and metamaterial based isolation enhancement structures provide experimentally measured minimum isolation (least achievable isolation in the band of interest) improvement of 7dB in the low band. Similarly, a minimum of 2dB isolation improvement is observed in the high band in both cases. In addition to isolation, the correlation coefficient, mean effective gain (MEG), radiation characteristics and total active reflection coefficient (TARC) values are investigated for the MIMO antenna system with integrated isolation structures. All these parameters satisfied the requirements for a MIMO antenna system with good diversity performance.

In addition to the DGS and metamaterial, neutralization line and magnetic walls are also investigated for their isolation enhancement characteristics on the 4-shaped MIMO antenna system. The results for these isolation structures are not promising due to the fact that their isolation mechanism does not match the radiation mechanism of the MIMO antenna system. Performance parameters such as correlation coefficient, MEG, TARC are also analyzed to evaluate their performance for MIMO applications. A performance comparison between the four

methods is also presented in this work.

خلاصة أطروحة

الاسم : احمد بلال نعمان

عنوان الدراسة: طرق تخمين العزل لنظام هوائيات متعدد المداخل والمخارج (MIMO)

الميدانية الرئيسية: الهندسة الكهربائية

التاريخ الدرجة: نيسان، ٢٠١٣

تعتمد كفاءة النظام متعدد المداخل والمخارج (MIMO) على القنوات المتعددة التي يتم انشاؤها بين العناصر المتعددة المشعة للمرسل والمستقبل. إذا كانت هذه العناصر المشعة في نظام نظام الهوائيات المتعدد المتعدد (MIMO) مرتبطة معا ارتباطا قويا فإن نظام الهوائيات كاملا سوف يعمل وكأن عبارة عن مصفوفة هوائيات واحدة. لذلك فإن العناصر المشعة في نظام الهوائيات المتعدد (MIMO) يجب أن تكون معزولة بقوة عن بعضها البعض بحيث أن الإشارة من عنصر مشع تكون مختلفة تماما ومستقلة عن الإشارة في بقية العناصر. هذه الإشارات المستقلة يكون بينها ارتباط ضعيف جدا لتحسين الاستفادة من تكنولوجيا النظام المتعدد (MIMO) .

في هذا العمل، تم عمل تصاميم مختلفة لتحسين العزل لنظام الهوائيات المتعدد (MIMO) . تصاميم العزل هذه تقوم على ما يسمى بالهيكل الأرضي المنشق (DGS) ، خط التعادل، الجدار المغناطيسي، و الميتاماتيريال (Metamaterial) . تم تطبيق هذه الهياكل على نظام هوائيات متعدد (MIMO) رباعي الشكل مزدوج النطاق ومزدوج العناصر. نظام الهوائي هذا يشع عند نطاقين مختلفين أحدهما عند 800 ميغاهيرتز تقريبا والآخر عند 2.7 جيجاهيرتز. هذا النظام يعاني من مستوى عزل ضعيف في كلا النطاقين والغير مقبول في نظام الهوائيات المتعدد (MIMO) . ولذلك، فإن هذه الهياكل مقترحة لتحسن العزل وتطوير الأداء.

كلا الهيكلين المقترحين ، (DGS) و الميتاماتيريال (Metamaterial) ، اعطوا بالقياسات

المعملية تحسين في عزل على الأقل (أقل عزل تم تحقيقه في النطاق المطلوب) حوالي 7dB في النطاق المنخفض. بينما في النطاق المرتفع، تم تحسين العزل بحوالي 2dB في كلتا الهيكلين. ذلك بالإضافة الى تحقيق قيم العزل، معامل الارتباط، متوسط التكبير المؤثر (MEG)، خصائص الانبعاث، و معامل الانعكاس النشط الكلي (TARC). كل هذه العوامل حققت مطالب نظام الهوائيات المتعدد مع تنوع جيد في الأداء.

بالإضافة إلى الهيكلين السابقين، فخط التعادل والحدار المغناطيسي تم تحقيق تحسين العزل لهم لنظام الهوائيات المتعدد (MIMO) الرباعي الشكل. لكن النتائج لهيكل العزل هاذان لم تكن مرضية وذلك نتيجة لأن تقنية العزل لم تطابق تقنية الانبعاث لنظام الهوائيات المتعدد (MIMO). أيضا تم تحقيق كل العوامل السابقة للهيكلين السابقين مثل (TARC) و (MEG) ومعامل الارتباط، تم تحليلهم لتقدير أدائهم لتطبيقات النظام المتعدد (MIMO). أيضا في هذا العمل مقارنة بين الأربع طرق السابقة.

CHAPTER 1

INTRODUCTION

1.1 Multiple Antenna Technologies

Communication systems are rapidly shifting from one antenna systems to multiple antenna systems to fulfill the bandwidth and reliability requirements within the limited frequency spectrum. There are a number of technologies that use multiple antennas such as Single Input Multiple Output (SIMO), Multiple Input Single Output(MISO) and Multiple Input Multiple Output(MIMO). In SIMO, there is one transmitter antenna and multiple receiver antennas. This configuration is known as receiver diversity. This technique enables the receiver to fight against fading by receiving multiple signals coming from different independent channels. In SIMO, the received signal can either be the combination of multiple received signals or data is received through the channel that has maximum signal strength. So SIMO uses switch diversity or maximum ratio combining (weighted sum of both signals) to receive the signal. In MISO, there are multiple transmitter and a single

receiver antenna. The redundant data is transmitted through multiple transmitter antennas. Thus the receiver has greater probability to receive the transmitted data correctly and hence mitigates the effects of multipath signal propagation. MIMO utilizes multiple antennas at the transmitter and multiple antennas at the receiver. This technology allows to transmit multiple data streams simultaneously in a multipath environment. Multiple copies of transmitted data are received at the receiver due to multipath then they get decoded to get the transmitted data back using MIMO algorithms. Hence a high data rate is achieved with reliability at the cost of increased complexity and computational power.

According to [1], the channel capacity is given by the Shannon channel capacity equation

$$C = W \log_2 \left(1 + \frac{P}{N_0 W} \right) \quad (1.1)$$

Where C is the channel capacity in bits/Hz/s, W is the bandwidth, P is the transmitted power and N_0 is the power spectral density of noise. The term (P/WN_0) is known as signal to noise ratio (SNR). The channel capacity can be increased by either increasing the SNR or the bandwidth of the channel. The capacity and the SNR has logarithmic relation. This means that after a certain value of SNR, the channel capacity saturates and further increase in the SNR has negligible effect on the capacity. Secondly the transmission of high energy signals is not efficient [2] and may cause interference to other communication systems.

Bandwidth is the second factor that can be used to increase the channel capacity. Increasing the bandwidth linearly increases the channel capacity but this

option is highly expensive. First of all, the frequency spectrum is very crowded due to the large number of wireless technologies and spectrum regulations. Purchasing a new spectrum is very costly. Secondly, wideband signals undergo selective fading in multipath environment. Selective fading severely distorts the signal and it requires computational power and other resources to mitigate this type of fading[3]. Moreover there is a strict control on the transmitted energy of the wideband signals to avoid interference with the other existing signals. For example the Federal Communications Commission (FCC) has enforced an energy mask on ultra wideband(UWB) indoor and outdoor signals to avoid interference. Low energy signals severely limit the range of communication.

The limitation in the availability of the frequency spectrum emphasizes the improvement of the channel capacity within the restricted bandwidth and signal energy. Multiple antenna systems improve the channel capacity or error rate with a fixed bandwidth and signal energy. The multiple channels between the transmitter and receiver can either be used to enhance the data rate by sending different data on each channel or it can improve the error rate by simultaneously sending multiple redundant copies of data on different channels as in case of SIMO and MISO. These technologies usually rely on the weight selection algorithm that weights the received signals through multiple channels depending upon the signal strength. Using multiple antennas on both the transmitter and receiver combines increased channel capacity with reliability. MIMO uses multipath to enhance the reliability and range and parallel connections between the transmitter and

receiver to enhance the data rate. It uses space-time algorithms as compared to weight selection algorithm to improve the quality of communication. MIMO antenna systems are a key enabling technology in all modern and 4G based wireless standards.

1.2 MIMO Technology

The MIMO system consists of multiple antennas at the transmitter and the receiver. The information data is fed to the encoder that encodes it according to some modulation scheme and feeds the data to multiple antennas. The transmitter transmits parallel data streams and each receiver antenna possibly receives data from multiple transmitter antennas. The received signal is decoded by reversing the encoder process, using strong computation power and a priori knowledge of channel at the receiver. The block diagram of a MIMO system is shown in Figure 1.1 In the case of an $N \times M$ MIMO antenna system, the data is split into N

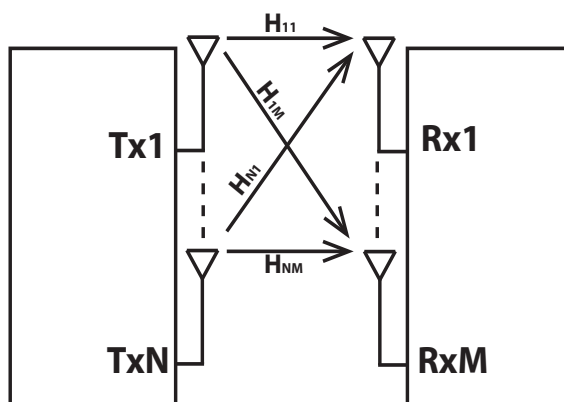


Figure 1.1: Block Diagram for MIMO Systems.

parallel streams. The contents of the parallel streams is determined by the MIMO

algorithm. The M receiving antennas receive data possibly from all the transmitting antennas. The received signal at the receiver can be written as follows [4]

$$\begin{aligned}
R_1 &= H_{11} \times T_1 + H_{12} \times T_2 + \dots + H_{1N} \times T_N \\
R_2 &= H_{21} \times T_1 + H_{22} \times T_2 + \dots + H_{2N} \times T_N \\
&\vdots \\
R_M &= H_{M1} \times T_1 + H_{M2} \times T_2 + \dots + H_{MN} \times T_N
\end{aligned} \tag{1.2}$$

where R_i is the received signal by the i^{th} antenna, T_j is the transmitted signal from the j^{th} antenna and H_{ij} is the complex weight representing the channel between the i^{th} and j^{th} antennas.

The received data at each antenna in the receiver is the weighted summation of the data transmitted by all the transmitter antennas. The relation between the transmitted and received signal can also be expressed in matrix form as.

$$[R]^t = [H][T]^t \tag{1.3}$$

where $R_{1 \times M}$ and $T_{1 \times N}$ are the received and transmitted vectors and $H_{M \times N}$ is the channel matrix and $[*]^t$ is conjugate transpose operation. The transmitted signal can be recovered by

$$[T]^t = [H]^{-1}[R]^t \tag{1.4}$$

Form these expressions it can be seen that MIMO uses spatial diversity and spatial multiplexing to enhance the link quality. The regeneration of the transmitted

signal is in fact the solution of K independent equations where K is the rank for the matrix 'H'. The rank of the matrix represents the independent equations represented by the matrix. If there is correlation between the channels then the number of the independent rows in the matrix will reduce and the rank will be lower. This means that smaller number of parallel independent data streams can be transmitted if the rank of H matrix is low. Hence the correlation between the channels reduces the MIMO system performance and its throughput.

Let us see why multipath is important for MIMO. Consider that there is no multipath between the transmitter and receiver. In this case the above equations become

$$\begin{aligned}
R_1 &= \alpha_1 \times \{T_1 + T_2 + \dots + T_N\} \\
R_2 &= \alpha_2 \times \{T_1 + T_2 + \dots + T_N\} \\
&\vdots \\
R_M &= \alpha_M \times \{T_1 + T_2 + \dots + T_N\}
\end{aligned} \tag{1.5}$$

where α_i will be constant that represent loss in air. It will be approximately the same for all the antennas as the distance between adjacent antennas is considered much smaller than the distance between the transmitter and receiver. If we express the above equation set in the matrix form and find the rank of the matrix, it will be one. This means that only one effective channel exists between the transmitter and receiver and the multi-antenna system just behaves like single antenna system. Hence the multi-path propagation is required to attain the spatial multiplexing for MIMO systems.

The expression for the channel capacity in case of MIMO is given by [4]

$$C = NW \log_2 \left(1 + \frac{P}{N_0 W} \right) \quad (1.6)$$

where N is the number of the parallel, uncorrelated and identical streams formed by the independent channels between the transmitter and receiver i.e. the rank of the H matrix. It is related to the number of highly isolated antennas in the system. According to equation (1.6) the capacity of the channel increases linearly with the number of transmitter and receiver antennas. Hence the channel capacity can be increased while keeping the bandwidth and SNR constant. MIMO technology not only increases the capacity but also improves the reliability and range by using multipath between the transmitter and receiver.

The advantages of MIMO come at certain costs. MIMO is a computationally intensive technique. First of all, the channel matrix H needs to be known at the receiver in order to decode the received data. Secondly, a set of linear equations is solved in order to recover the transmitted data and the computational power requirement increases exponentially as the number of antennas increases. These costs become severe especially in battery powered mobile devices where the battery-life is an important performance measuring metric.

1.3 Antenna Systems for MIMO

The benefits of MIMO come with certain challenges. One of the basic requirements for MIMO systems is that the channels between the transmitter and receiver should be uncorrelated so that the different radiators behave differently and do not actually act as a single radiator or reduce the rank of the channel matrix. In other words the radiating elements should receive signals that are uncorrelated. Correlated signals affect the advantages of MIMO systems. The Cumulative distribution function (CDF) of the channel capacity for an 8×8 MIMO is shown in Figure 1.2 [4]. The CDF is generated by using the random nature of the channel. The shift of the CDF curves to the right side shows improved channel capacity. Maximum capacity can be achieved with completely independent channels (i.i.d. in Figure 1.2). The curves in Figure 1.2 are plotted for different spread angles. The higher the spread angle(Δ), the lower is the correlation between the channels. So, curves with higher spread angles show greater channel capacity for the MIMO system.

The antenna system has an important role in the channel isolation. Antennas can increase the channel correlation by two ways, either by coupling through their structure or by the radiation characteristics. The antenna structure can provide direct path between the different ports that will increase the correlation. This factor is known as antenna isolation. The isolation is measured through the s-parameters of the antenna system. The radiation pattern characteristics are the second mechanism that increases the correlation between the antennas. It is

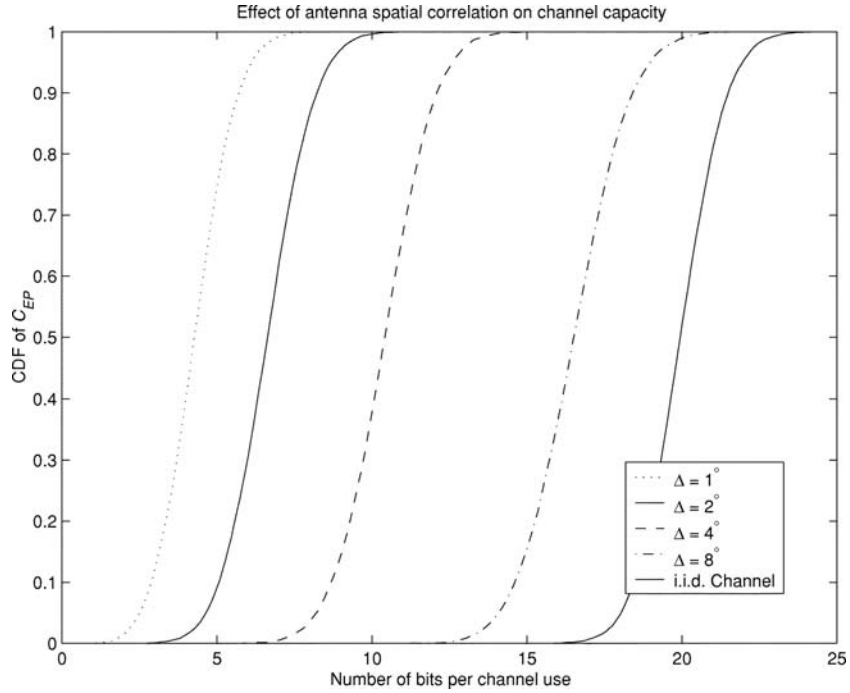


Figure 1.2: Effect of correlation on channel capacity

possible that the radiators are well isolated but their radiation patterns are such that the transmit or receive energy is coupled with the transmit or receive fields of a neighbouring antenna in the near or far field. In this way the radiators are coupled through the radiation patterns instead of their antenna structure. This type of coupling is measured by the correlation coefficient of the antenna system. These antenna performance parameters will be discussed in Chapter 2.

1.4 Design Challenges for MIMO Antenna Systems

It is desirable to have high isolation and low correlation coefficient values to reduce the coupling between the channels. In an antenna system, the isolation between

the radiators can be improved by placing them far apart (at least $\lambda/2$). But the space is not always available, specially on handheld devices.

MIMO technology is being deployed in mobile communication systems. This means that we have multiple antennas at the base station and at the mobile terminal as well. Cellular communication systems tend to operate at low frequencies (in 700-900MHz range) to provide better coverage and quality of service (QoS). Design of a MIMO antenna system for the base station operating at low frequencies is not a big issue as there is no strict restriction on space. So radiators can be placed far apart to achieve high isolation. The real challenge is to design a well isolated antenna system for mobile terminals operating in sub-GHz frequency range. Mobile terminals apply strict limitations on the area of the antenna system. The low frequency of operation reduces the electric length between the radiators. So they cannot be simply placed adjacent to each other. An isolation structure is required to enhance the isolation between the radiators to achieve the acceptable performance of the antenna system working in a MIMO system.

1.5 Thesis Contributions

Multiple radiators in a compact space, like in handheld devices, operating at sub-GHz frequency ranges, that is common in existing communication systems, exhibit very low isolation [5]. This isolation is not acceptable to achieve spatial diversity that is a primary requirement for MIMO technology. Isolation enhancement techniques for closely packed antennas are one of the major research topics in modern

communication systems these days.

The objective of this work is to investigate practical isolation methods that can be used for printed MIMO antennas to enhance the isolation of adjacent radiators within the user equipment to provide better diversity performance. In particular, two metamaterial based isolation techniques, based on capacitively loaded loops and magnetic wall, will be investigated. Non-metamaterial based isolation techniques, based on defected ground structure (DGS) and neutralization line (NL) will be investigated as well. A recently developed 4-shaped MIMO antenna system [5] will be used to draw the conclusions.

The thesis objectives can be summarized as

1. Investigate and implement two metamaterial based isolation enhancement methods for a planar printed MIMO antenna system.
2. Redesign the metamaterial structures to make them operate at dual bands in order to be applied to a dual-band dual-element printed MIMO antenna system
3. Investigate and implement two isolation enhancement methods that are based on DGS and NL for dual band MIMO antenna system.
4. Compare the performance of the four isolation enhancement methods and draw conclusions on the advantages and disadvantages of these methods.

1.6 Thesis Outline

This thesis presents performance evaluation for four different isolation enhancement structures on a printed MIMO antenna system. The organization of the work is as follows, MIMO antenna system performance evaluation metrics are discussed in Chapter 2. Chapter 3 includes a detailed literature review in this area. The antenna system, on which the isolation enhancement structures are applied, is described in Chapter 4. Chapter 5 discusses two non-metamaterial based isolation enhancement techniques. Metamaterial based isolation enhancement structures are discussed in Chapter 6 and finally conclusions and future work are discussed in Chapter 7.

CHAPTER 2

PERFORMANCE METRICS

FOR MIMO ANTENNA

SYSTEMS

The performance of a single antenna or antenna array is measured by analyzing its s-parameters and gain patterns. These parameters are not sufficient to evaluate the performance of MIMO antenna systems. There are a number of reasons for this. First, s-parameters curves increase rapidly as the number of antennas increase. For example the 2 element antenna system has four s-parameters and a 3 element antenna system has nine s-parameter curves. Analysis of such large number of parameters is not convenient. Similarly the performance of an isolated antenna is not the only important factor in the MIMO antenna system. Analysis of the mutual effects on the performance of different radiating elements is also important. Moreover the isolated radiation pattern of a single antenna does not

show the complete picture. The presence of other radiation patterns need to be taken into account. The effect of the channel in which the antenna system operates is also important. So, the following are the performance metrics used to evaluate MIMO antenna systems.

1. Isolation
2. Correlation Coefficient
3. Mean Effective Gain (MEG)
4. Total Active Reflection Coefficient (TARC)
5. Channel Capacity
6. Diversity Gain
7. Antenna Size, Gain and Efficiency

Each of these metric will be discussed in detail

2.1 Isolation

Isolation measures how much signal couples between the radiators within the antenna system structure. It does not represent the coupling through the radiation patterns. Isolation is measured through the s-parameters. The transmission coefficient (S_{xy}) between the two radiators' feeding ports (radiator x and radiator y) measures this quantity.

The isolation can be compromised by a number of factors. The radiating elements can be coupled with each other through electric and/or magnetic fields within the antenna structure. Ground plane currents can also be a major factor in coupling the radiating elements as the ground plane size is small in compact antenna systems. So it is important to know the exact cause of the coupling before neutralizing it. There are a large number of techniques available in literature that address this issue. Some of them uses defects in the ground plane, parasitic elements in the antenna structure, lumped components, frequency selective materials, magnetic wall between the radiators and many others. These techniques will be discussed in detail in the literature review (Chapter 3) and some will be used in this work.

2.2 Correlation Coefficient

Correlation coefficient is a measure that describes how much the communication channels are isolated from each other. This metric deals with the radiation pattern of the antenna system. The square of the correlation coefficient is known as envelop correlation coefficient. The envelop correlation coefficient(ρ_e) can be calculated by the following formula [6],

$$\rho_e = \frac{\left| \iint_{4\pi} [\vec{F}_1(\theta, \phi) * \vec{F}_2(\theta, \phi)] d\Omega \right|^2}{\iint_{4\pi} |\vec{F}_1(\theta, \phi)|^2 d\Omega \iint_{4\pi} |\vec{F}_2(\theta, \phi)|^2 d\Omega} \quad (2.1)$$

where $F_i(\theta, \phi)$ is the field radiation pattern of the antenna when the i^{th} port is excited and all other ports are terminated to matched load. This is a complicated expression that requires three dimensional radiation pattern measurements and numerical integration to get the envelop correlation coefficient. Simple derivation in [6] proves that the correlation coefficient can be calculated by using the s-parameters and radiation efficiency. The general expression becomes

$$|\rho_{(ij)}|^2 = \rho_{(eij)} = \left| \frac{|S_{ii}^* S_{ij} + S_{ji}^* S_{jj}|}{|(1 - |S_{ii}|^2 - |S_{ji}|^2)(1 - |S_{jj}|^2 - |S_{ij}|^2)\eta_{radi}\eta_{radj}|^{(1/2)}} \right|^2 \quad (2.2)$$

where ρ_{ij} is correlation coefficient, ρ_{eij} is envelop correlation coefficient, S_{ij} is the S-parameter between the i and j elements and η_{radi} is radiation efficiency for i^{th} element. In this formula we need to know only the S-parameters and the radiation efficiencies that can be evaluated easily as compared to 3D radiation patterns required by Equation (2.1). It is important to mention that though the Equation 2.2 involves isolation (S_{ij}) yet no direct relation can be established between the isolation and correlation coefficient as there are a number of other factors involved in this equation. Change in the isolation will also affect the other parameters such as resonance (S_{ii}) and radiation efficiencies.

However [7] questioned the accuracy of the correlation coefficient calculated using S-parameters for antenna system having radiation efficiency less than 50%. The author provided the upper and lower bounds on the correlation coefficient

that is given as

$$|\rho_{rec}|_{max,min} = |\rho_{rec,0}| \pm \sqrt{\left(\frac{1}{\eta_{rad1}} - 1\right) \left(\frac{1}{\eta_{rad2}} - 1\right)} \quad (2.3)$$

Following the condition

$$0 \leq |\rho_{rec}| \leq 1 \quad (2.4)$$

Where ρ_{rec} is correlation coefficient and $\rho_{rec,0}$ is correlation coefficient given in Equation (2.2). The factor $\sqrt{\left(\frac{1}{\eta_1} - 1\right) \left(\frac{1}{\eta_2} - 1\right)}$ adds to formula by considering loss correlation that is normally ignored. This factor determines the degree of uncertainty in the calculation for correlation coefficient using the S-parameters. This factor is 1 for antenna system having radiation efficiency of 50% for both radiators. The unity factor of uncertainty is very high for any calculation. This factor grows rapidly as the radiation efficiency reduces below 50%. So for antenna systems with low radiation efficiencies, the correlation coefficient values calculated using S-parameters do not provided meaningful information. In these cases, the correlation coefficient values should be calculated using the 3D radiation pattern using formula given in Equation (2.1). However in spite of this ambiguity in the calculation of the correlation coefficient values using S-parameters, many researchers used this method for electrically small antennas [8].

It is important to mention that the isolation and correlation coefficient are two different things. High isolation does not guarantee a high correlation coefficient and vice versa. High isolation and low correlation coefficient is required for the

MIMO antenna system.

2.3 Mean Effective Gain (MEG)

Standalone antenna gain is not a good measure of antenna performance as the antenna is not used in an anechoic chamber in practical applications. The antenna is used in a certain environment for a specific application. So the study of the effect of the environment on the antenna radiation characteristics is important to evaluate the antenna performance. One way to do this is to fabricate an antenna, operate it under the specific conditions along with another standard antenna with known characteristics, and get the antenna performance. We have to fabricate a prototype, test it to get the results, tune the antenna and repeat the process to get the desired design. This procedure is very time consuming and costly. The practical method of calculating MEG is described in [9].

The solution of this problem was proposed in [10]. Here the author proposed a probabilistic model for the environment and using the three dimensional radiation pattern with the proposed statistical model in a mathematical expression, we can get MEG numerically. This numerical method allows us to get MEG using the simulated/measured gain patterns along with a model of the environment suitable for the application for which antenna is being designed. The mathematical expression for MEG is shown Equations (2.5) and (2.6).

$$MEG = \int_0^{2\pi} \int_0^\pi \left\{ \frac{\Gamma}{1+\Gamma} G_\theta(\theta, \phi) P_\theta(\theta, \phi) + \frac{1}{1+\Gamma} G_\phi(\theta, \phi) P_\phi(\theta, \phi) \right\} \quad (2.5)$$

Satisfying the conditions

$$\begin{aligned} \int_0^{2\pi} \int_0^\pi \{G_\theta(\theta, \phi) + G_\phi(\theta, \phi)\} \sin \theta d\theta d\phi &= 4\pi \\ \int_0^{2\pi} \int_0^\pi P_\theta(\theta, \phi) \sin \theta d\theta d\phi &= \int_0^{2\pi} \int_0^\pi P_\phi(\theta, \phi) \sin \theta d\theta d\phi = 1 \end{aligned} \quad (2.6)$$

where $\Gamma = (\text{Vertical mean incident power}) / (\text{Horizontal mean incident power})$ is the cross-polarization power ratio that represents the distribution of the incoming power, $G_\theta(\theta, \phi)$ and $G_\phi(\theta, \phi)$ are antenna gain components and $P_\theta(\theta, \phi)$ and $P_\phi(\theta, \phi)$ represent the channel model.

There are a number of channel models available in literature. A channel model suites a particular environment such as urban, rural etc. A general channel model is given by [10]. This model assumes uniform distribution of the signals in azimuth direction and Gaussian distribution in elevation direction. This represents a regular Rayleigh fading channel for cellular communications. Mathematically it can be written as,

$$\begin{aligned} P_\theta(\theta, \phi) &= A_\theta \exp \left[-\frac{\{\theta - [(\pi/2 - m_v)]\}^2}{2\sigma_v^2} \right], (0 < \theta < \pi) \\ P_\phi(\theta, \phi) &= A_\phi \exp \left[-\frac{\{\theta - [(\pi/2 - m_H)]\}^2}{2\sigma_H^2} \right], (0 < \theta < \pi) \end{aligned} \quad (2.7)$$

where m_i and σ_i are horizontal or vertical mean and standard deviation, respectively, of the Gaussian distribution representing the statistical model for horizontal or vertical signal distribution.

The above model requires 3D radiation pattern measurement and processing. To simplify the process, the incoming waves are assumed to be concentrated on

the horizontal plane only. This assumption significantly reduces the complexity of MEG calculation. The formula (2.5) for MEG becomes [11],

$$G_e = \int_0^{2\pi} \left\{ \frac{\Gamma}{1+\Gamma} G_\theta(\theta_1, \phi) P_\theta(\theta_1, \phi) + \frac{1}{1+\Gamma} G_\phi(\theta_1, \phi) P_\phi(\theta_1, \phi) \right\} d\phi \quad (2.8)$$

where θ_1 is the elevation angle of the incident wave. This angle depends on the orientation of the antenna, radiation pattern and coordinate system. In this work, the antenna lies in the xy-plane and radiates in the +z direction. So θ_1 is selected as 0° where the maxima is expected. However if the maximum does not occur at $\theta = 0^\circ$ then lower values of MEG are expected or vice versa.

Furthermore if we assume a uniform distribution in the horizontal plane then the channel model becomes

$$P_\theta(\theta_1, \phi) = P_\phi(\theta_1, \phi) = \frac{1}{2\pi} \quad (2.9)$$

In [11], MEG is calculated for a mobile antenna under an urban environment model. A statistical model for the multipath line-of-sight urban environment is proposed and experimental MEG was also calculated to compare the results with the theoretical model. In [12], MEG was analyzed in a Ricean channel that represents mixed environment that represents both line of sight (LoS) and non line of sight (NLoS) situations. Interpretation of MEG under Rayleigh fading is also provided in this reference. MEG will also be discussed in literature review while describing the performance of MIMO antenna systems.

2.4 Total Active Reflection Coefficient (TARC)

TARC is defined as the square root of the ratio of the sum of the power available at all the ports minus the radiated power to the total available power [13],

$$\Gamma_a^t = \sqrt{\frac{\text{available power} - \text{radiated power}}{\text{available power}}} \quad (2.10)$$

TARC is a real number between 0 and 1. When the TARC value is zero, this means that all the available power is radiated. The available power is the sum of powers available on all the ports of the antenna system.

The S-parameters matrix grow exponentially with the increase in the number of antennas. For two antenna systems, the S-parameters matrix is of order 2×2 and for three element antenna system the matrix size grows to the order of 3×3 . It is very difficult to track all the curves for large number of radiating elements in an antenna system. TARC is a method to manipulate all the S-parameters for N port networks and display a single curve that has all the information of S-parameters. In addition to compressing the information from many curves to a single curve, TARC also includes the effect of feeding phase to the antenna port. Hence a single curve of TARC can be used to determine the resonance frequency and impedance bandwidth of the whole antenna system[13].

The expression of TARC, introduced in [13], can be evaluated by following

formula for two port networks [14].

$$\Gamma_a^t = \sqrt{\frac{(|S_{11} + S_{12}e^{j\theta}|^2) + (|S_{21} + S_{22}e^{j\theta}|^2)}{2}} \quad (2.11)$$

where θ is input feeding phase, S_{xx} and S_{xy} are s-parameters associated with the antenna structure.

The general formula for TARC from the measured S-parameters is given by [13]

$$\Gamma_a^t = \frac{\sqrt{\sum_{i=1}^N |b_i|^2}}{\sqrt{\sum_{i=1}^N |a_i|^2}} \quad (2.12)$$

where

$$[b] = [S][a] \quad (2.13)$$

where vector $[a]$ is the excitation for the antenna structure. This excitation does not affect the TARC value as it will be eventually be cancelled out by the same value in the numerator provided all the ports are equally excited. This is why the formula for the two port does not depend on excitation. TARC will also be referred to in the literature review (Chapter 3) to demonstrate the MIMO antenna system performance.

2.5 Channel Capacity

Channel capacity is a measure of how many bits can be sent per 1 Hz of the bandwidth. It is used to compare the performance improvement of a MIMO system

relative to a single antenna system. It is also a convenient measure to determine the performance of the MIMO system relative to ideal all-independent-channels system. The channel capacity is usually measured in the form of cumulative distribution function(CDF) or relative to the SNR. The first step to measure the channel capacity is to determine the channel matrix. The channel matrix is determined by the radiation patterns of the antenna system. The channel matrix can be determine as [15]

$$H = \psi_R^{1/2} G \psi_T^{1/2} \quad (2.14)$$

where $\psi_{RM \times M}$ and $\psi_{TN \times N}$ are the receive and transmit coefficient matrices respectively and $G_{M \times N}$ is a matrix containing complex Gaussian random numbers representing the randomness of the channel.

The correlation coefficient entries can be written as

$$\psi^{i,j} = \frac{\mu_{ij}}{\sqrt{\mu_{ii}\mu_{jj}}} \quad (2.15)$$

where

$$\mu_{ij} = \int E\{[A_i(\Omega).h(\Omega)][A_j^*(\Omega).h^*(\Omega)]\}d\Omega \quad (2.16)$$

$A_i(\Omega)$ represents the field pattern of the i^{th} element and $h(\Omega)$ represents the incoming waves. This integral is very complicated and requires complete three dimensional radiation pattern. However certain assumptions, under certain practical conditions, allow us to simplify this integral. So if we assume a Rayleigh fading envelop, only horizontal incoming waves, uncorrelated orthogonal polar-

ization of incoming waves and constant time average power density per steradian then the correlation coefficient expression becomes [15]

$$\mu_{ij} = \int_0^{2\pi} [\Gamma A_{i\theta}(\pi/2, \phi) A_{j\theta}^*(\pi/2, \phi) + A_{i\phi}(\pi/2, \phi) A_{j\phi}^*(\pi/2, \phi)] d\phi \quad (2.17)$$

where Γ is the cross-polarization discrimination and $A_{\theta}(\pi/2, \phi)$ and $A_{\phi}(\pi/2, \phi)$ are theta and phi E-field pattern at theta=90°.

Once the 'H' is known, the capacity can be found by the following formula.

$$C = \log_2 \left[\det \left(I_R + \frac{\rho}{N_T} H H^T \right) \right] \quad (2.18)$$

where I_R is $N_R \times N_R$ identity matrix, N_R and N_T are the number receive and transmit antennas and H^t is conjugate transpose of H matrix. It is clear from the formula that if H is an identity matrix then the capacity is the number of antennas (rank of 'H') times the capacity of one antenna.

To get the CDF, a sequence of the capacity values is generated by calculating the capacity several times. This is a random sequence due to the dependence of the capacity on the channel that is modeled by Gaussian random variable. This random sequence is used to get the CDF for the capacity. For calculating the capacity relative to the SNR, the SNR is increased in regular intervals and the capacity is calculated with new value of SNR. In this way capacity is plotted against the SNR.

2.6 Diversity Gain

The diversity gain is a measure of the effect of diversity on the communication system performance. Diversity gain is defined as the effect on the time averaged SNR of combined signals from the diversity antenna system relative to a single antenna system on one diversity channel provided the SNR is above a reference level. Mathematically the diversity gain is defined as follows [16]

$$DiversityGain = \left[\frac{\gamma_C}{\Gamma_C} - \frac{\gamma_1}{\Gamma_1} \right]_{P(\gamma_C < \gamma_S/\Gamma)} \quad (2.19)$$

where γ_C and Γ_C are the instantaneous and mean SNR for the diversity system respectively and γ_1 and Γ_1 are the instantaneous and mean SNR for the single branch with maximum values in the diversity system. γ_S/Γ is the reference level. Assuming uncorrelated signals with Rayleigh distribution, the $P(\gamma_C < \gamma_S/\Gamma)$ can be approximated as

$$P\left(\gamma_C < \frac{\gamma_S}{\Gamma}\right) = \left(1 - e^{-\frac{\gamma_S}{\Gamma}}\right)^M \quad (2.20)$$

The diversity gain and correlation coefficient are related to each other. The lower the correlation coefficient, the higher is the diversity gain. The relation (2.20) is usually met if $|MEG1 - MEG2| < 3dB$ [17].

2.7 Antenna Size, Gain and Efficiency

Antenna gain and size are related to each other. Antenna dimensions are a func-

tion of the operating wavelength. Antenna size increases as the operating frequency is reduced. However mobile devices cannot afford large sized antenna systems. So designs have to compromise between the size and the gain of the antenna. But the antenna gain has direct relation with the efficiency of the antenna. Lower gain means smaller radiation efficiency[18]. So the antenna should be optimized for gain and size.

2.8 Summary

The performance metrics for MIMO antenna systems are discussed in this chapter. The performance metrics for single radiator antenna systems do not completely describe the performance of multi-radiator antenna systems. In addition to the reflection coefficient and radiation characteristics, the effect of coupling on the antenna performance is also important. The isolation level indicates how much the radiators are isolated within the structure of the antenna system. The correlation coefficient value indicated that how much the radiation patterns of the radiators are isolated. MEG describes the behaviour of the antenna system within a specific environment. TARC relates the radiated power with the total input power and it is the optimum method to see the behaviour of the multi-port antenna system. The channel capacity is a measure to compare the improvements in the data rate achieved by using different technologies and configurations. The diversity gain is a measure of the effect of diversity on the communication system performance. In addition to these metrics, antenna size, dimensions, gain, radiation efficiencies

are also important parameters to evaluate the performance of the multi-element antenna system.

CHAPTER 3

LITERATURE REVIEW

There are a number of techniques available in literature that target MIMO antenna isolation improvement. This is a very active area as MIMO is going to be the future of communication technology. Antenna isolation techniques can be broadly classified into the following major categories[8].

1. Antenna configuration
2. Decoupling Networks
3. Parasitic elements
4. Defected Ground Plane Structures
5. Neutralization lines
6. Metamaterials

In this chapter we will review what has been done in these areas and what will be our contribution.

3.1 Antenna configurations

Antenna orientation is important in MIMO antenna systems. If the antenna system is operating at high frequencies (above 1GHz) then placing radiating elements wide apart within the maximum available space (typically $100 \times 50 \text{mm}^2$ for a user terminal) usually improves the antenna isolation. Moreover antenna orientation can make use of polarization to improve the correlation coefficient of the antenna system.

In [19], the effect of the position of planar inverted-F antennas (PIFA) and monopoles is studied. The PIFAs are arranged in collinear, parallel and orthogonal arrangements. Mixed arrangements of monopole and PIFA and two monopoles configurations are also studied in this work. In the collinear arrangement, the two PIFAs are arranged along a straight line passing through the feeding points. In this configuration it was found that minimum coupling is achieved when the open ends of the PIFAs are at the opposite sides (farthest apart) i.e. the feeding points facing each other. Same thing was for parallel arrangements. In this arrangement, the PIFAs are placed side by side with parallel edges. The maximum isolation is achieved when the open ends are farthest apart (when the PIFA are rotated by 180°). In the orthogonal configuration, the radiator axis (line along the radiator structure passing through the feeding point) form 90° angles with each other. In this configuration the minimum isolation is achieved when the feeding points of both radiators are facing each other at the corner of 90° . Two monopoles and one monopole and one PIFA configurations are also studied in this work. It was

found that the monopole and PIFA configuration exhibits slightly better isolation. Isolation of all the configurations was studied with respect to the spacing between the radiating elements and, as expected, the isolation improves with the increase in spacing.

The effect of the position of the printed antenna within the board is discussed in [20]. In this work an antenna system for personal digital assistant (PDA) is discussed. This antenna system consists of two radiators, one operating in GSM/DCS (890-960MHz/1710-1880MHz) band and the other operating in WLAN(2400-2484MHz) band. The WLAN radiator is moved along the periphery of the antenna system board and the isolation between the two radiators is observed using S-parameters. It was found that maximum isolation is achieved when the radiators are configured along the diagonal of the antenna system board as it provides maximum distance between the radiators. This reference also studied the cause of coupling between the particular radiator under test. The authors found that the radiators are coupled through the ground plane currents as the two radiators share the same ground plane. The authors excite one radiator and study the ground plane currents due to this excitation. They found that in the case when the radiators are closely placed, there is a strong ground plane current coupling between the two radiators that significantly reduces the isolation. We get maximum isolation if we place the radiators far apart such that the ground plane current of two antennas do not couple with each other.

In [21], a dual-band antenna system, operating at 2.45GHz and 5.5GHz is

presented. Three isolation improvement techniques were applied on the antenna structure to enhance isolation at both bands. Two of them are the neutralization line at the feed point and connecting the plane at the bottom of the antenna system. The third technique is orthogonal orientation of the radiating elements. This arrangement generates polarization and radiation pattern that are orthogonal to each other and hence improve the isolation. Isolation of more than 15dB is achieved after applying all the isolation techniques.

The position of radiating elements in an inverted-F antennas (IFA) MIMO antenna array of two elements is studied in [22]. The antenna system operates at 3GHz and has a ground plane size of $100 \times 50mm$. Five different cases were studied in this work. In Case-A, radiating elements with open ends in the same direction were configured along opposite, longer sides of the ground plane. In Case-B the elements were placed on the same longer side and with the same direction of the open end. In Case-C the elements, with the same open end direction, were arranged along opposite, shorter sides of the ground plane. In Case-D the elements were arranged on adjacent sides with the same direction of open end of IFA. And Case-F was the same as Case-D but with an opposite direction of the open end. The result of this study was same as that of [20] that says that the farther the radiating elements, the lower is the ground plane interaction currents. Smaller coupling in the ground plane currents causes minimum isolation. So Case-C provided maximum distance between the radiating elements and hence had minimum isolation. Case-E and Case-D provides minimum isolation when

they were close to the corner common between the radiators.

3.2 Decoupling Networks

Theoretical analysis of decoupling networks was presented in [23]. In this reference, the scattering matrix was used to develop theoretical background related to decoupling networks. A decoupling network is represented by a network that neutralizes the coupling terms S_{ij} of the original network. This decoupling network is inserted between the original network and its feeds. With the required properties of the feed network (network should be decoupled i.e. S_{ij} should be zero) and known properties of the original network, theoretical expressions are derived for the decoupling network. Decoupling networks with losses are also treated in this reference.

In [24], another theoretical analysis for decoupling networks was represented. In this reference certain assumptions were made on the antenna and feeding network. Based on these assumptions an impedance (Z) matrix is derived and a decoupling network is realized to show the effectiveness of the described theory. The network is assumed to be lossless.

A four port decoupling structure that is realized using the S-parameters was proposed in [25]. The proposed structure consisted of two transmission lines and a shunt impedance. The authors derived the formulae for this network using known input scattering matrix and required scattering matrix at the input of the antenna system. The proposed decoupling network is placed between the input feed and

the antenna input. The general expressions in the scattering matrix of a shunt impedance placed between the two transmission lines was also known. Using these three scattering matrices, we can derive the expression for the unknown shunt impedance in the decoupling network and the length of the transmission line. The reference provides an example of a decoupling network designed for two monopole antenna closely packed with each other. The antenna system operates at 2.45 GHz. Without the decoupling network the minimum isolation in the required band was approximately 3dB. By applying the decoupling network the isolation at the resonance frequency improved to 30dB and the overall isolation improvement within the operating band was greater than 10dB. The same technique is also successfully applied to closely packed miniaturized antennas.

In [26], isolation between two meander line monopole antenna operating at 710MHz was improved using a branch-line coupler. The gap between the radiators was only $\lambda/45$. With such a small length between the radiating elements, achieving high isolation is a real challenge. The authors realize the coupler using lumped components as distributed components will take a lot of space that is not acceptable for mobile applications. Without the coupler, the achievable isolation was about 5dB. The minimum isolation was improved by more than 10dB throughout the band. At the resonance approximately 40dB isolation was achieved as compared to 5dB isolation without the coupler. The authors also included the envelop correlation coefficient and channel capacity curves to prove the validity of their design.

A different coupling structure was proposed in [27]. Instead of placing the decoupling structure at the feed point, the authors placed a mushroom like structure on the ground plane between the two miniaturized MIMO radiators. The MIMO antennas were split ring resonator (SRR) shaped antenna operating at 2.5GHz. The antenna elements were designed for WiMAX applications and high bands of LTE. Without the decoupling structure, the isolation of the antenna system was about 8dB. The planar mushroom like structure, placed in the ground plane between the two radiators, captures the coupling ground currents and hence improved the isolation from 8dB to 19dB. The isolation was below 12dB in the whole band of operation.

3.3 Parasitic Elements

Antenna isolation can be improved by placing properly shaped parasitic elements on proper locations within the structure. In [28], a parasitic element is introduced between the two monopoles to enhance the isolation. The parasitic element, placed in between the radiators, provides an additional coupling path between the radiators such that it cancels the original coupling. This mechanism is the same as that of neutralization line but there is no physical link between the radiating elements in this case. The dimensions, shape and location of parasitic element should be such that it produces 180° out of phase currents on the other radiating element to cancel out unwanted currents that cause the coupling. To demonstrate the efficiency of this method of enhancing the isolation, the authors proposed an

antenna structure and applied this technique on that structure. The proposed structure consisted of two printed monopoles and a parasitic element in between them. The antenna system operated in WLAN frequency band (2.4-2.48GHz) and the maximum isolation achieved was 30dB within the desired band. The authors have also provided the comparison of their proposed technique with other isolation techniques such as slit in the ground plane and with the split ground plane. In both cases the isolation was only 6dB that is not acceptable for MIMO applications.

In [15], another example is provided to enhance the isolation between the dual-slot-element antennas using monopoles as parasitic elements. The mechanism to reduce the isolation is same as described in [28]. The designed antenna operated in the UMTS band (1920-2170MHz) and the mutual coupling was below 20dB in the whole band of operation. The authors measured the channel capacity to validate the isolation improvement as channel capacity has a direct relation with isolation. The channel capacity CDF for a random channel is presented along with the curve showing the increase in the channel capacity with SNR. In both graphs the performance of the antenna system relative to the ideal uncorrelated channel is presented. It was clear that the antenna performance was close to the performance of the ideal uncorrelated channel that validates the effectiveness of the isolation technique proposed in the paper.

The authors investigated transmission lines as parasitic elements in [29]. For the test setup they designed four patch antenna elements resonating at 5GHz for

WLAN frequency. Then they formed a four element MIMO antenna by placing these patch elements on the same substrate with a common ground. The parasitic transmission lines are placed between the two antennas horizontally. The effect of length and number of transmission lines between the radiators was investigated in this study. In this case, the parasitic elements act as resonators that capture the coupling energy at resonance. The current distribution on the antenna structure and parasitic elements was also shown to prove the fact that the parasitic elements are canceling the coupling currents on the antenna structure. The resonance of the transmission line depends on its length. Increasing the length lowers the resonance frequency. Hence tuning the parasitic elements reduces the isolation within the required band by 10dB. The effect of vertical transmission lines as parasitic elements was also studied in this work. Different positions and lengths of vertical transmission line were investigated to have good isolation. Finally a combination of horizontal and vertical transmission lines as parasitic elements was proposed to get maximum isolation.

In [30], two PIFAs are combined to form an integrated dual PIFA for WLAN applications. The operating band of the antenna system was 2.4-2.484GHz. In this antenna system, the shorting point was shared by both PIFAs. The isolation was increased by introducing a folded resonator near the antenna structure. This folded resonator acted as a parasitic element that canceled the coupling current. Without the folded resonator, the isolation range in the operating band was 10-13dB. Remarkable improvement in the isolation was observed with the application

of the folded resonator with isolation range of 15-35dB within the band of operation. In this study the effect of the ground plane size was also presented. It was shown that varying the ground plane size significantly affects the resonance frequency.

A dual band isolation example was presented in [31] using parasitic element. In this reference a dual-band dual-element antenna system covering WLAN bands (2.4/5.2/5.8) was designed for laptops. The isolation of this antenna was improved by using a parasitic meander line resonator placed between the radiating elements. The meander line resonator was designed to provide isolation at 2.4 and 5.5 GHz. The last section of the resonator was meandered to tune the second resonance at 5.5GHz while keeping the 2.4 GHz resonance unchanged. The isolation was improved from 11.7dB to 17dB and from 14.3 to 18.2dB at the low band (2.4GHz) and high band(5.2-5.8GHz), respectively, compared to the reference model without the parasitic resonator. The current distribution on the antenna element and the parasitic resonator was also shown to prove that the resonator is cancelling the coupling current. Different configurations of the parasitic resonator were also studied in this work and an optimum configuration for both bands was proposed in the final design.

3.4 Defected Ground-plane Structures (DGS)

Defects in the ground plane are used widely in antenna systems. They can be used to widen the bandwidth, increase isolation and miniaturize the radiator. In

fact the defects in the ground plane add inductances and capacitances within the antenna structures. These additional inductances and capacitances are used to modify the antenna system according to the requirement of interest. Isolation improvement characteristics will be discussed in this section. To increase the isolation at a specific frequency, the additional inductance and capacitance, generated by the defects in the ground plane, are used to realize a band-stop filter at that frequency. This band-stop filter improves the isolation.

In [32], slits in the ground plane were introduced to enhance the isolation. Two closely packed IFA are placed on the same ground. There were two set of slits in the ground plane separated by a small gap. The antenna system was operating at the 2.27-2.35GHz band with isolation of 5dB without any isolation structure. The isolation was improved by more than 15dB by applying the proposed DGS. The DGS proposed, act as an LC resonator that resonate at a frequency where the isolation is required. The slits act as a distributed capacitance and the space between the two set of slits acts as distributed inductance and the combined LC act as a band-stop filter. The characteristics of this filter were also studied in this work. To prove the effectiveness of the proposed structure, the authors compared the performance of proposed isolation structure with a conventional ground plane(without any defect) and a split ground plane. The proposed structure performance was better than other two by at least 15dB and 7.5dB, respectively. The proposed structure was also applied on non-printed monopole and printed patch radiators to show that the isolation structure is valid for general antenna

elements. Slight shift of the resonance frequency towards the high frequency was also observed after applying the proposed structure.

Isolation was improved by implementing a high impedance line using a low impedance line with a DGS in [33]. The length and width of a dual-polarized patch antenna are adjusted to have resonance at 2 and 2.5GHz. The feed port with DGS was used to feed the 2GHz port. The equivalent lumped component circuit consisted of an inductor and a short circuited stub line. The microstrip line with a spiral DGS were simulated separately to see the effect of the DGS on the antenna response. It was shown that such a DGS integrated transmission line acts as a band-stop filter that can be used to improve the isolation. When this type of transmission line is applied to feed the antenna at the 2GHz port, more than 20dB isolation improvement was achieved. Hence this type of feed can be used to enhance the port isolation.

In [34], a novel DGS was introduced between two PIFAs. The DGS was based on a modified dumbbell shaped structure. To increase the distance from the radiating ends of the antenna, the PIFAs were fed at the opposite ends relative to each other. By applying the DGS, the resonating frequency of the antennas lowers. The reason might be the change in the material characteristics such as the effective permittivity due to the DGS. The antenna isolation at 7.5GHz was about 23 dB without the DGS. By applying the DGS more than 17dB isolation improvement was observed. The current distribution on the ground plane with DGS was also included for better understanding its operation. It is clear that

the DGS captures the majority of the coupling current and hence improves the isolation. A parametric study of different parameters of DGS was also presented in the paper to better understand the behavior of the DGS. In the end, a comparison was made between different types of DGS such as split ground, metallic wall on the ground and simple dumbbell shaped DGS. It was shown that the proposed DGS performance is better than other other's.

A four element multi-layer antenna system was presented in [35]. There were two types of radiating elements within the antenna system. Two radiating elements were proximity fed microstrip square ring patch antennas and the other two were microstrip slot antennas. The best isolation was achieved by two techniques. Firstly the radiators were placed on the edge and among the different layers to reduce the edge coupling. The square ring patch radiators were placed diagonally on the opposite corners of the antenna system. This arrangements minimized the edge coupling between the patch radiators. The slot radiators were placed on separate layer so that there is no edge coupling between the slot radiators and patch radiators. The second technique, used to improve the isolation, was a DGS. Slits were etched in the ground plane to capture the coupling ground plane currents. The slits in the ground plane act as band-stop filter as shown by the S-parameters of the test setup containing ground plane slits. The length and the width were designed such that the stop-band lies within the desired frequency range. The paper shows the ground plane current distribution for the antenna system with and without the slits in the ground plane. The introduction of slits in the ground

place forces the currents of each radiating element not to couple with the other an radiating element. This technique improved the isolation. The maximum isolation achieved without slits was about 12dB due to the proper arrangements for radiating elements. Slits further improved the isolation by 10dB.

In [36], a DGS was used to enhance the isolation and miniaturization of an antenna. A simple dumbbell shaped DGS was used in this work. Two dumbbell shaped DGS were placed below the radiating patches, one under each patch, to reduce the dimensions of the radiators. This thing lowered the center resonant frequency from 6GHz to 5.25GHz. One DGS was placed between the radiating elements. This DGS act as stop-band filter at a specific frequency defined by its dimensions. The isolation improved by about 12dB from 15.3 to 27.5 dB. The lumped component equivalent for dumbbell shaped DGS was also included in work that was a parallel LC network .

A novel DGS was introduced in [37] that not only reduced the mutual coupling but also improved the impedance bandwidth. The radiating element in the antenna system was dual-branch monopole. To improve the properties of the antenna system, the authors added a 90° bent slit close to the antenna feed. These bents capture majority of the coupling current in the ground plane. These slits also act as slot radiator as they get coupled with the feeding line. This thing improved the bandwidth of the system. However there can be a strong coupling between the slot radiators formed by the bent slits. To overcome this problem, the bents were made of 90° so that the coupling signals from the two slot radiators are

orthogonal to each other. Hence the coupling was reduced and impedance bandwidth was increased using novel slits in the ground plane. The authors introduced a metallic line between the monopoles to reduce near field coupling. The metallic trace between the monopole acted as a reflector and prohibited the radiation pattern of two radiating elements to interact and hence provide smaller correlation coefficient. In addition to the novel bent slits and a metallic trace between the radiators, a triangular defect in the ground was also introduced at the base of the metallic trace. These defects provide the designer additional control to the ground plane current distribution. The performance of the antenna system varies with the variation of the currents in the ground plane. The dimensions of the triangular defects were optimized to get maximum performance. The antenna system provided 10dB impedance bandwidth from 2.4 to 6.55GHz with isolation better than 18dB in the band of operation. MIMO antenna performance characteristics such as MEG, correlation coefficients were calculated by the authors to evaluate their antenna performance for MIMO applications.

In [38], mutual coupling between rectangular patch radiators was reduced using rectangular slits in the ground placed between the two radiators. The patch radiators were designed to resonate at 9.1GHz. The position, dimensions and number of slits were parametrically studied in this reference. Approximately 16.5dB improvement in isolation was observed by applying DGS between the radiation elements.

3.5 Neutralization Line

In principle, a neutralization line is just like the decoupling parasitic element. A neutralization line takes the current at a certain point on the radiating element structure, inverts its phase along its length and cancels out the current at the same location of the adjacent radiating element. Cancellation of unwanted currents on the radiator's structure usually cause improvement in isolation provided that the unwanted currents on the radiators are the major reason of high coupling. There are several examples in literature that validate this method.

The neutralization line was introduced in [39] to improve the isolation between two PIFAs operating on slightly different frequency bands (1710-1880MHz (DSC) and 1920-2170MHz (UMTS)). The two radiating elements were placed in different configurations to get an idea about the reason of low isolation. The isolation was improved by adding a line connecting specific points on the radiator's surface. The point should be selected by considering following factors.

1. The point should be located at maximum current area i.e. for PIFA it should be away from the open end and close to the feed point.
2. The location should not affect the resonance frequency and bandwidth of the antenna.
3. The location should have maximum current for maximum frequency range so that the isolation improvement structure can handle wider bandwidth.

Two different cases were studied. In one case, the PIFAs were arranged such that

their feeding points were facing each other and in another case the shorting strips were facing one another. Extensive tuning was required to get the appropriate position to connect the neutralization line. Observing the isolation curve of the two cases, it can be concluded that wideband isolation improvement was achieved by placing the shorting strips facing each other as in this case the connection point of the neutralization line remains at low impedance for wider range of frequencies and hence the three factors associated with this point remains stable for the wider bandwidth.

In [14], a 2x1 monopole based MIMO antenna system was presented. The monopole antennas were designed and optimized individually then they were placed on the upper portion of common substrate to form a MIMO antenna system. The band of operation for the monopole was WLAN varying from 2.4 to 2.48GHz. Isolation was achieved using a neutralization line connecting the two radiators near the feeding point. The connecting point selection criteria was same as discussed in [39]. The current distribution and the direction of current helps in understanding the concept. Using these current distribution diagrams, it can be seen that the direction of the current is opposite at the both ends of the neutralization line and this opposite current is cancelling the current coupling on the other radiating structure. The isolation range was improved from 7-9dB to 19-40dB by applying the neutralization line. The antenna performance was evaluated on the basis of TARC, cumulative probability distribution function (CPDF) and gain patterns.

A neutralization line was used to enhance the port isolation between the two port rectangular patch based antenna system in [40]. The rectangular patch radiators were designed to resonate at 5.75 GHz. The neutralization line connects the feed line of the two patch radiators. The isolation was improved from 9dB to more than 20dB. The current distribution was shown. This current distribution showed that the neutralization line canceled out the unwanted currents and enhanced the port isolation.

In [41], a neutralization line was used to connect the two monopole radiators forming a MIMO antenna system. The band of operation for the monopole was 2.4-2.497GHz. In this reference the authors considered the neutralization line as a band-stop filter. The band-stop properties of the stop-band filter were determined by the dimensions of the neutralization line. Maximum isolation improved from 13dB to 30dB due to the application of the neutralization line.

3.6 Metamaterials

Metamaterials are artificially engineered materials that are generally realized by periodic repetition of a basic building block known as a Unit Element (UE) or unit cell (UC). The UE determines the properties of the metamaterials. Metamaterials have the property to provide a stop band at a specific frequency determined by the UE. This stop-band can be utilized to provide isolation if the metamaterial is designed properly. In literature there are many practical examples that uses metamaterials to enhance the isolation.

In [42], a multi-layer antenna structure was proposed. One layer was 1.6mm thick FR-4 and the other layer was 0.8mm thick FR-4. The rectangular radiating elements with L-shaped slots were printed on the top of the 0.8mm thick substrate. The bottom of the 0.8mm thick substrate act as the ground plane. Split ring resonators (SRRs) were etched on the 1.6mm thick substrate and connected to the ground plane through vias. The frequency band of operation for the radiating elements was mobile WiMAX band of (3.4-3.6GHz). A set of six SRRs was printed between the radiating elements creating a metamaterial. This metamaterial is responsible for increasing the isolation between the radiating elements. The isolation range improved from 12-13dB to 15-35dB after applying the metamaterial. Hence a significant improvement in the isolation was achieved by deploying the metamaterial in between the radiating elements.

Printed loop radiators resonating at 2.5GHz were isolated using an artificial magnetic wall created by periodically placing a novel UC in [43]. The UC consisted of interdigital capacitors printed on the plane shared by the radiating elements. The ends of these interdigital capacitors are connected to the ground plane using vias. The interdigital capacitor along with via and ground plane form a UE. The periodic repetition of the UE created the metamaterial. In this particular case the metamaterial acted as an artificial magnetic wall that will not allow the magnetic field to pass through. The creation of this wall depends on the operation of the UE. In fact when the magnetic field passes through the UE in the direction that is perpendicular to the axis of the UE (supposing that the axis of UE passes

through the center of interdigital capacitor parallel to the line connecting the two radiators), currents are generated in the opposite direction of the UE to cancel the applied field according to Lenz's law. These currents excite the UE and it resonates at a specific frequency depending on its dimensions. So if the dimensions of the UE are properly designed then the UE is able to create a stop-band filter at that frequency provided that the magnetic field properly excites the UE. Hence the isolation was improved using this magnetic wall.

In [44], a novel UE based metamaterial is used to enhance the isolation between two loop radiators. The loop antenna consisted of an inner loop and an SRR shaped outer loop resonating at 2.45GHz. The outer loop provided distributed capacitance that is used for impedance matching as the inner loop radiator exhibits inductive behavior. The UE for the absorber cell consisted of open complementary split ring resonator (OCSRR) and an SRR placed on the other sides of the substrate. The OCSRR is derived from the open split ring resonator(OSRR) and complementary split ring resonator(CSRR). The OCSRR is compact in size and exhibits negative permittivity. The SRR on the top side provides negative permeability. Hence the UE was capable of providing a double negative material. This UE and its array of three elements were tuned to resonate at 2.45GHz. A significant isolation improvement was observed by placing an array of three UEs between the radiators. The isolation was improved by more than 10dB from (11dB to 22.2 dB) using the absorbers. However the absorber also reduced the radiation efficiency from 87% to 60%. The size of the antenna system was $51 \times 24 \times 2 \text{ mm}^3$.

Different configurations of capacitively loaded loops (CLLs) were used to enhance the isolation between two monopoles, resonating at approximately 2.6GHz as demonstrated in [45]. The volume occupied by the antenna was $16 \times 50 \times 0.8 \text{ mm}^3$. An array of 2x3 UE was placed between the monopoles to enhance the isolation. Approximately 6dB isolation improvement was observed with this configuration. In another configuration, the second element of middle column was removed. More than 10dB isolation improvement was observed in this configuration. As the metamaterial absorbs the electromagnetic fields, the antenna gain is degraded with the use of a metamaterial.

In [46], a three-layer antenna system is proposed with a novel SRR providing negative permeability. The two meander strip radiating elements were placed on the top two corners of the antenna system. Two L-shaped sections were placed in the ground plane that was at the bottom side of the third layer. A single segment interdigital capacitor, forming one section of the SRR was placed between the meander strip radiating elements. This section of the SRR was connected to the middle layer strip using vias to form a complete SRR. The overall volume of the antenna was $45 \times 80 \times 1.2 \text{ mm}^3$. The authors have shown the effective negative permeability of the interdigital SRR in the band of interest. The isolation improvement for the desired band (2.3-2.4GHz) was from 15-17dB to 15-27dB with 10dB improvement at the resonance frequency. The literature review is summarized in Figure 3.1. The figure divides the references into two major categories. One is based on the number of bands and the other is based on the resonance

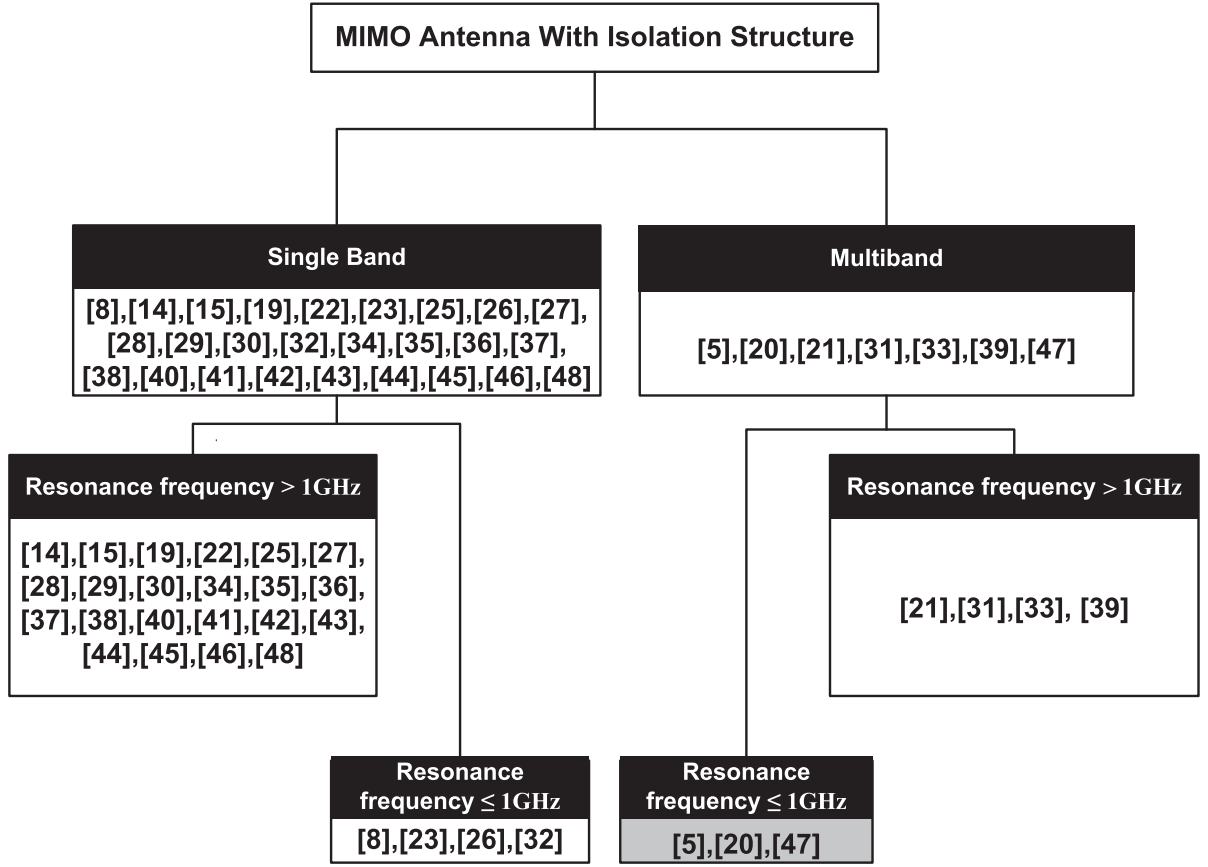


Figure 3.1: Summary of the literature review and work contribution region.

frequency range.

It can be seen from Figure 3.1 that there has been a lot of work in the high frequency single band antennas. While multi-band MIMO antenna systems, specially with one of their bands of operation under 1GHz frequency are not covered well in the literature. MIMO antenna systems with these characteristics (multi-band with one band of operation in sub-GHz frequency range) are among the research challenges that communication systems designers and the research community are currently working on. The grayed box in the Figure 3.1 show the contribution aspects of this work. In the grayed box, there are three references

only. References [5] and [47] are the baselines of this work while [20] covers the GSM band (890-960MHz).

3.7 Summary

In this chapter, research and previous work related to isolation enhancement techniques for MIMO antenna systems are presented. In literature, these techniques are divided into six classes. These classes are antenna configurations, decoupling networks, parasitic elements, defected ground structures, neutralization lines and metamaterials. Research work related to each class is discussed in a separate section. Finally, all the research work is categorized in a tree to illustrate the importance of this work. The categorization is performed based on the bands and operating frequency of the antenna system. It can be concluded from Figure 3.1 that very little work is available for multi-band, multi-element antenna systems operating in sub-GHz frequency ranges. Thus contribution of this work adds more to this region.

CHAPTER 4

THE 4-SHAPED REFERENCE MIMO ANTENNA SYSTEM

In this work, isolation structures are designed and applied to the 4-shaped antenna structure that appeared in 2×1 configuration in [47]. This 4-shaped antenna system resonates in the frequency band (-6dB bandwidth) of 853-920MHz and 2933-3130MHz. This is a novel antenna system derived from the PIFA antenna geometry. The volume of the structure in [47] is $50 \times 50 \times 0.8mm^3$. However the isolation of the antenna system is very low. The minimum isolation (least achievable isolation) is approximately 3dB and 5dB for the low band and high band respectively. This level of isolation is not acceptable for MIMO antenna systems.

4.1 4-Shaped MIMO Antenna System

The base line of this work is the antenna structure proposed in [47]. This structure is further modified to fit it within the standard antenna size for mobile terminals that is $50 \times 100mm^2$. The modifications involve the extension of the ground plane and tuning of the radiating structures to get the resonance at the desired frequencies. The modified antenna structure is shown in Figure 4.1 by extending its ground plane size. This model is denoted by Model_A from now on.

The dimensions of this model are (in mm): $W = 50$, $L = 100$, $Wt = 2.2$, $H = 2.5493$, $L1 = 40.75$, $L2 = 27$, $Ys = 5.5$, $Xa2 = 1.6716$, $Lf = 15.8$, $Xs = 0.6716$, $Xf = 2.6716$, $Wf = 2.5$, $Ws = 1$, $Yf = 15.5$, $W1 = 10$, $Y = 46$ and $W2 = 17$. This model consists of two 4-shaped radiators arranged in a 2×1 configuration to form a MIMO antenna system. The substrate used is FR-4 one with 1.56mm thickness and 4.4 dielectric constant. The antenna model was created and optimized using $HFSS^{TM}$.

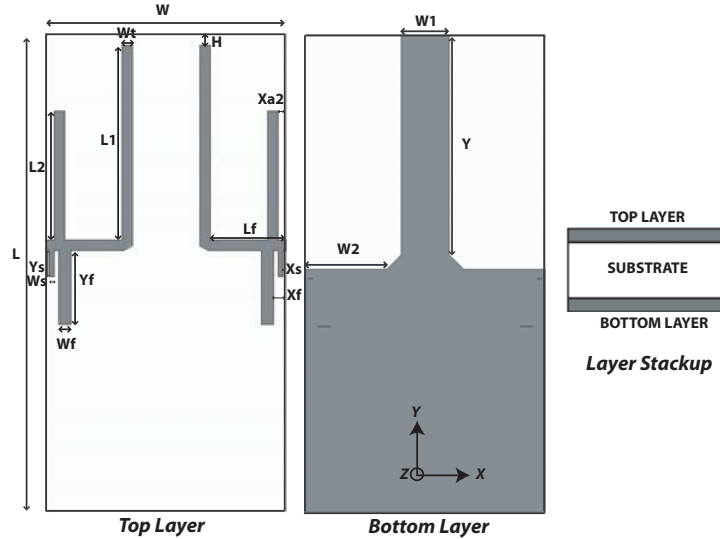


Figure 4.1: Simulation model for Model_A.

4.2 Characteristics of the 4-Shaped MIMO Antenna System

The fabricated prototype for Model_A is shown in Figure 4.2. This prototype was characterized and measured in the laboratory using an HP8510C vector network analyzer (VNA) at KFUPM microwave laboratory. The simulated and measured

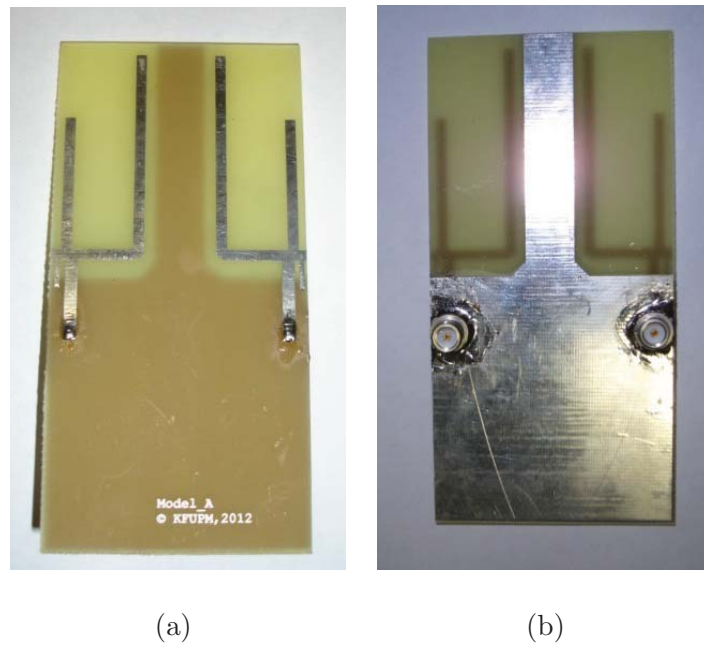


Figure 4.2: Fabricated prototype for Model_A, (a) Top side (b) Bottom side

S-parameters are shown in Figures 4.3 and 4.4 for the low band and high band, respectively. These curves show that the antenna system resonates at 770MHz and 2.54GHz with approximately 30MHz and 150MHz, -6dB bandwidth for the low and high bands, respectively. The isolation was 9.5dB and 7.2dB for the low band and high band, respectively. The difference between the measured and the simulated results is due to the imperfections in the fabrication process and

difference in the dielectric constant values between the simulated and fabricated antennas.

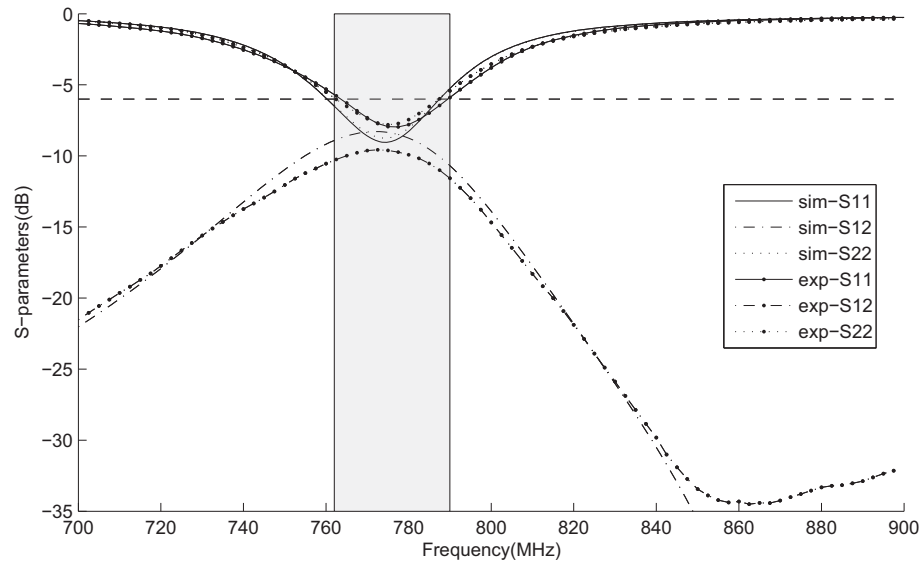


Figure 4.3: Low band S-parameters for Model A.

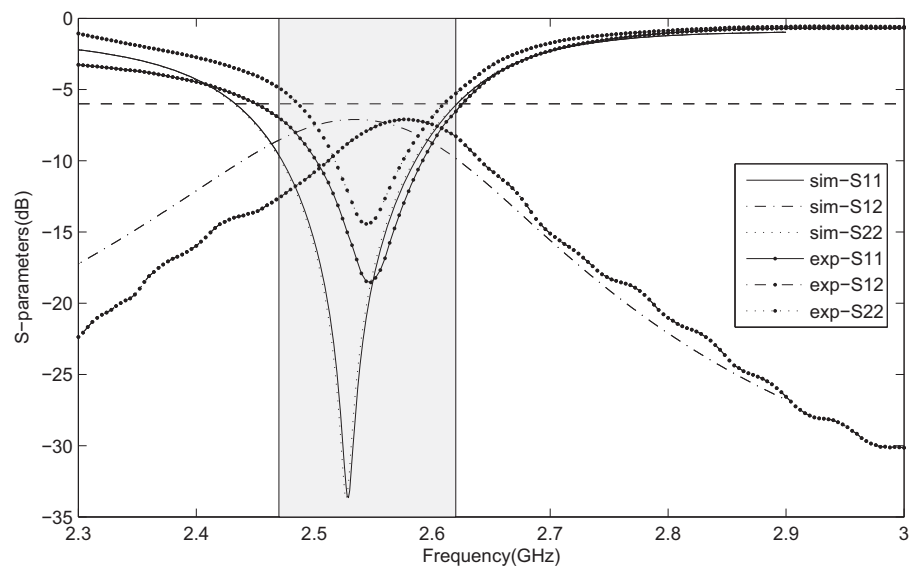


Figure 4.4: High band S-parameters for Model A.

The TARC curves for the reference model are shown in Figures 4.5 and 4.6 for low and high bands, respectively. The TARC curves are generated for different input phases varying from 0° to 180° relative to the phase of the first port using Equation (2.11). The TARC curves for the low band are almost identical for all the input phases but variations in the frequency and magnitude can be observed for the high band curves. The TARC curves at different phases show the antenna system does resonate during all the input phases for the low band with minimum shift. The resonance frequency changes significantly for the high band when port two is excited with different phases. This means that the MIMO antenna system effective bandwidth will change due to such phase shifts. All phases cover the band of interest but some phases show a degradation in the bandwidth covered.

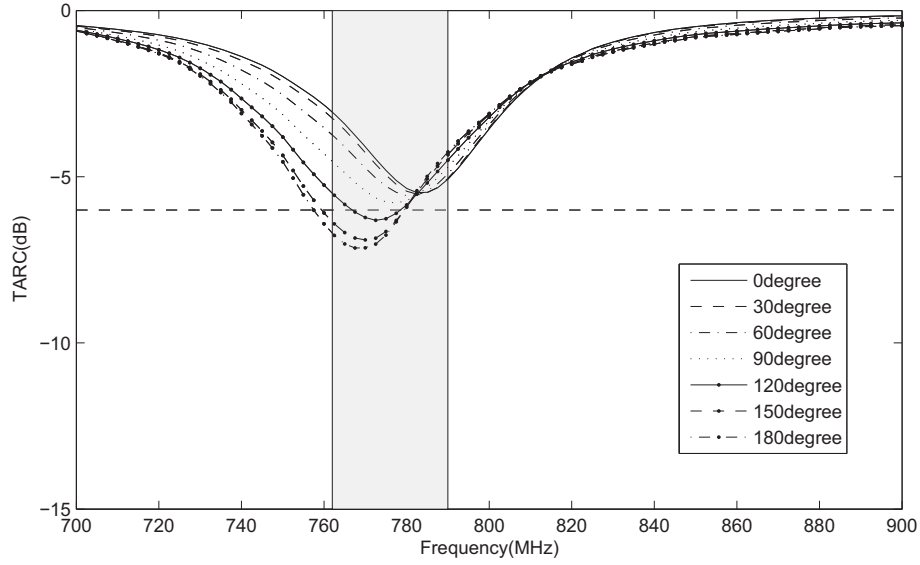


Figure 4.5: Low band TARC for Model A.

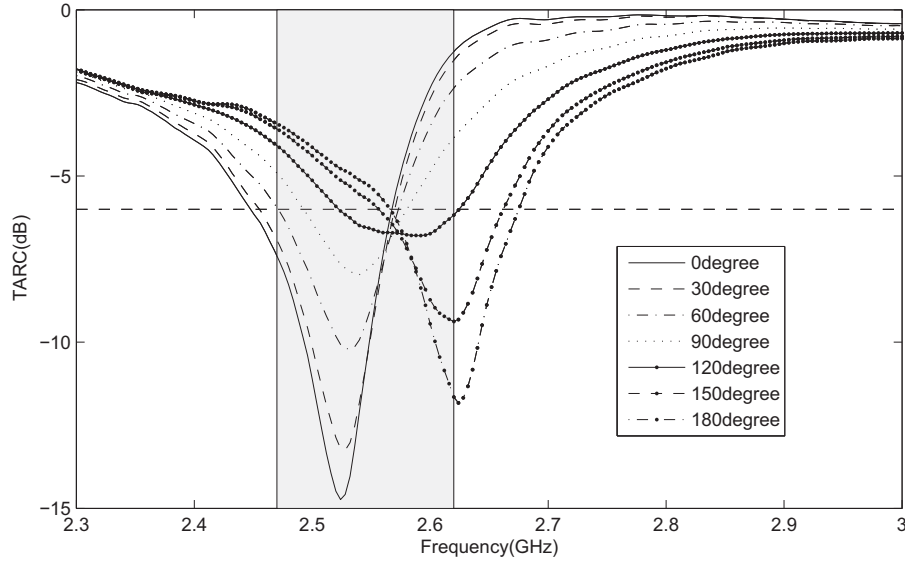


Figure 4.6: High band TARC for Model_A.

The correlation curves are shown in Figures 4.7 and 4.8 for the low band and high band, respectively. They were calculated from S-parameters measurements using Equation (2.2). The correlation curves indicate the independence between the different channels formed by the antenna system. In literature [48], the value of 0.3 is described as an acceptable value for the correlation coefficient for MIMO antenna systems. The correlation coefficient values in the low band are below 0.2 but in the high band, they are approximately 0.35. The curves were created based on the radiation efficiency values of 40% and 75% for the low and high bands, respectively.

The current distribution curves for Model_A are shown in Figures 4.9 and 4.10 at 755MHz and 2.55GHz, respectively. In these figures one 4-shaped radiating element is excited while the other is terminated to matched load. These current

distributions will be compared with other models with isolation enhancement structures to see the effects of these structures.

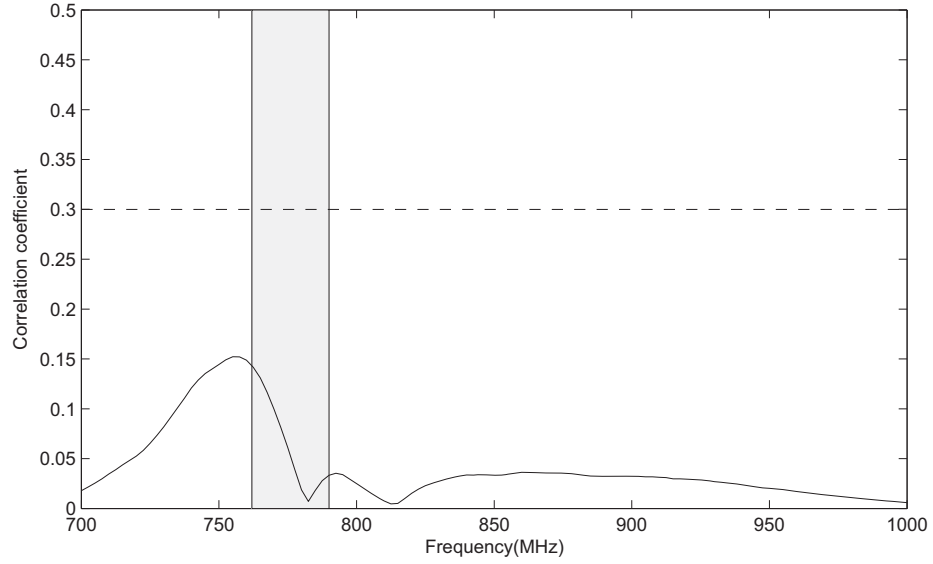


Figure 4.7: Low band correlation coefficient for Model_A.

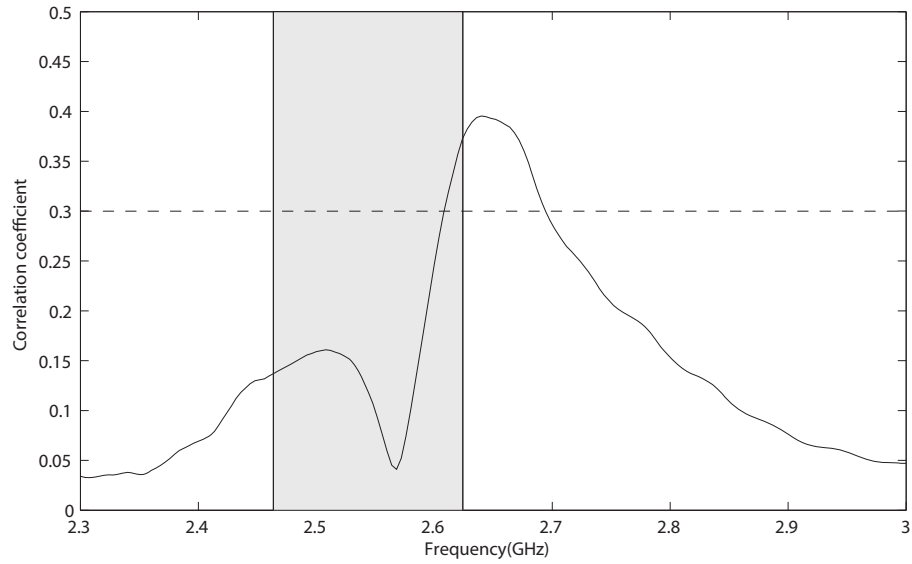


Figure 4.8: High band correlation coefficient for Model_A.

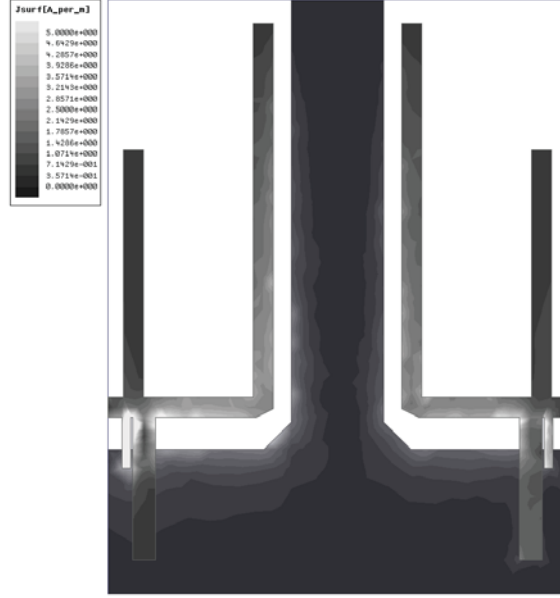


Figure 4.9: Current distribution for Model_A at 775MHz.

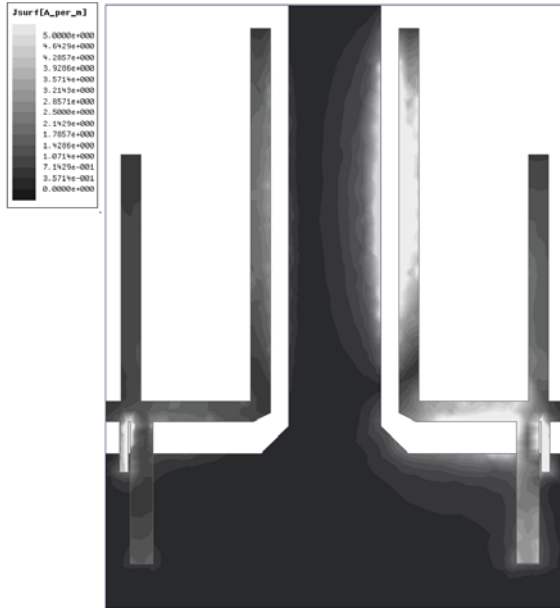


Figure 4.10: Current distribution for Model_A at 2.55GHz.

The 2D cuts of the measured gain pattern are shown in Figure 4.11. The maximum measured gain was -4dBi and 0dBi for the low band and high band respectively. Figures 4.11(a) and 4.11(b) show the principle plane cuts of the measured gain

patterns for Element 1 and 2 for co-polarization (gain theta) and cross polarization (gain phi) at 755 MHz. Similarly Figures 4.11(c) and 4.11(d) show the principle plane cuts of the measured gain patterns for Element 1 and 2 for co-polarization and cross polarization at 2.55 GHz. The measurements were conducted at an outdoor antenna range facility at Oakland University, Michigan, USA.

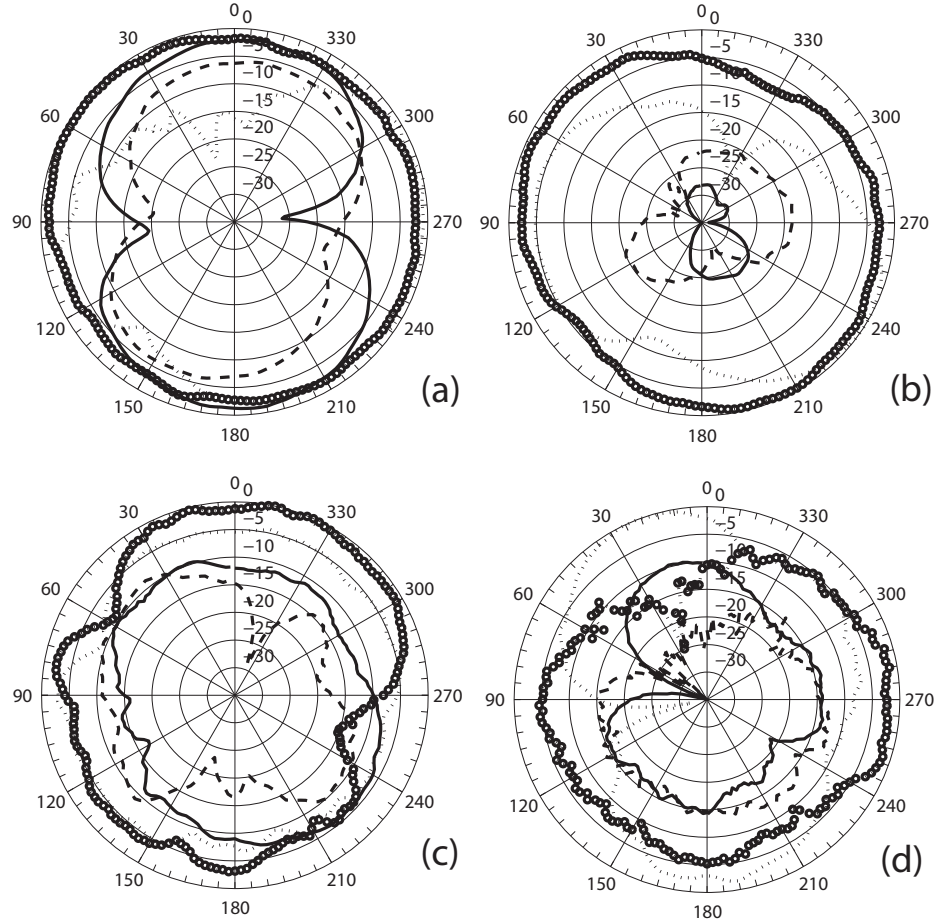


Figure 4.11: Measured gain patterns for Model_A, Dots:vertical polarization for element 1, Circles:vertical polarization for element 2, Solid:horizontal element 1, Dashes:horizontal polarization element 2.

MEG values are calculated according to Equation (2.8) using simulated gain patterns. The calculated MEG for Model_A for the low band with cross-polarization discrimination (Γ) of 0dB were $MEG1_{LOW} = -1.511dB$ and

$MEG2_{LOW} = -1.53dB$, for elements 1 and 2, respectively. For the high band, the values were $MEG1_{HIGH} = -1.7937dB$ and $MEG2_{HIGH} = -1.585dB$, for elements 1 and 2, respectively. With a Γ value of 6 dB, the values were $MEG1_{LOW} = -1.496dB$, $MEG2_{LOW} = -1.516dB$, $MEG1_{HIGH} = -1.804dB$ and $MEG2_{HIGH} = -1.5973dB$, for the low and high bands of elements 1 and 2. It is evident that the ratio of $MEG1/MEG2 < 3dB$ at both bands of operation with both Γ values that provides acceptable diversity gain. All these performance parameters are summarized in Table 4.1.

Table 4.1: Summary for Model_A performance parameters

Parameters	Low-Band	High-Band
Bandwidth (-6dB)	762-792MHz	2.465-2.615GHz
Maximum gain	-4dBi	0dBi
Minimum isolation	9.5dB	7.1dB
Efficiency(η)	40%	75%
Correlation Coefficient	0.15	0.35
MEG1($\Gamma = 0$)	-1.511dB	-1.7937dB
MEG1($\Gamma = 6dB$)	-1.496dB	-1.804dB
MEG2($\Gamma = 0$)	-1.53dB	-1.585dB
MEG2($\Gamma = 6dB$)	-1.516dB	-1.5973dB

4.3 Isolation Enhancement for the 4-Shaped MIMO Antenna System

Four techniques will be used to enhance the isolation of the 4-shaped MIMO antenna system(Model_A). These techniques can be broadly classified into two classes named as

1. Non-Metamaterial based isolation enhancement structures

2. Metamaterial based isolation enhancement structures

Two different techniques from each class are applied to Model_A. Chapter 5 describes the non-metamaterial based structures. The non-metamaterial based isolation structures cover the defected ground structure (DGS) and the neutralization line (NL) techniques. Chapter 6 discusses the metamaterial based techniques covering capacitively loaded loop(CLL) based metamaterial and a magnetic wall.

4.4 Summary

This chapter discusses the reference MIMO antenna system that will be used to test the validity of the isolation enhancement structures. This model is denoted by Model_A. This is dual-band, dual-element MIMO antenna system that is based on 4-shaped printed radiators. The antenna resonates at $762 - 792MHz$ and $2.465 - 2.615GHz$ frequency bands. The minimum measured isolation levels are $9.5dB$ and $7.1dB$ for low and high bands, respectively. The efficiency at the low band is 40%, and is lower than the efficiency at the high band (75%) due to the electrically small size at this band. In addition to these parameters, total active reflection correlation (TARC), correlation coefficient, mean effective gain (MEG), current distribution figures and gain patterns are also presented in this chapter to set a base line for the improvements proposed in this work.

CHAPTER 5

NON-METAMATERIAL BASED ISOLATION ENHANCEMENT STRUCTURES

As described in Section 1.4, the isolation decreases with reduction of electrical length between the radiators of a MIMO antenna system. This reduction in the isolation compromises the benefits of the MIMO technology. Additional structures are introduced in the antenna system to enhance the isolation between the radiators. These additional structures either cancel the coupling signals using polarization/orthogonality or realizing some kind of band-stop filter between the radiators. Hence these structures explicitly reduce the coupling signals between the radiators that result in isolation enhancement.

5.1 Requirements for an Isolation Enhancement Structure

The purpose of this work is to enhance the isolation of the dual-band, dual-element 4-shaped printed MIMO antenna system described in Chapter 4 (Model_A). There are two primary requirements imposed on the isolation enhancement structures for this MIMO antenna system

1. The structure should be compact
2. The structure should be dual-band

The reference MIMO antenna system is very compact ($50 \times 100mm^2$). The isolation enhancement structure should be compact enough to be fit within the limited space between the radiating elements. On the other hand, the size of the structure increases with the decrease in the resonating frequency. So it is a challenging task to design a compact isolation enhancement structure operating at sub-GHz frequency ranges.

In addition to the compactness, the isolation enhancement structure should also be dual band. Both bands of the reference antenna suffer from low isolation. So an effective isolation enhancement structure should be able to suppress the coupling signals at both bands. This requirement further complicates the design of the structure.

5.2 Design of the DGS based Isolation Enhancement Structure

Defects in the ground plane add capacitance and inductance to the structure. This feature is widely used to realize filters and design compact devices. The idea behind the DGS based isolation enhancement structure is to realize a band-stop filter between the radiating elements.

5.2.1 Test Setup

The design of the DGS structure is based on the work that appeared in [49]. The design starts with a modified dumbbell shaped DGS tuned to provide the stop-band at the higher frequency band. The lower band is covered by loading the rectangles of the modified dumbbell shaped DGS with spirals designed to resonate at the required frequency.

The DGS was initially designed on a test setup to facilitate the design procedure. The test setup is shown in Figure 5.1. The DGS test setup consists of a transmission line (black) coupling energy across the defects in the ground plane (gray). The S-parameters of this test setup describe the behaviour of the DGS. The study of the transmission coefficient describes the position and number of the stop-bands covered by the structure. The geometry of the proposed structure was optimized and the effect of each parameter was investigated through a parametric study.

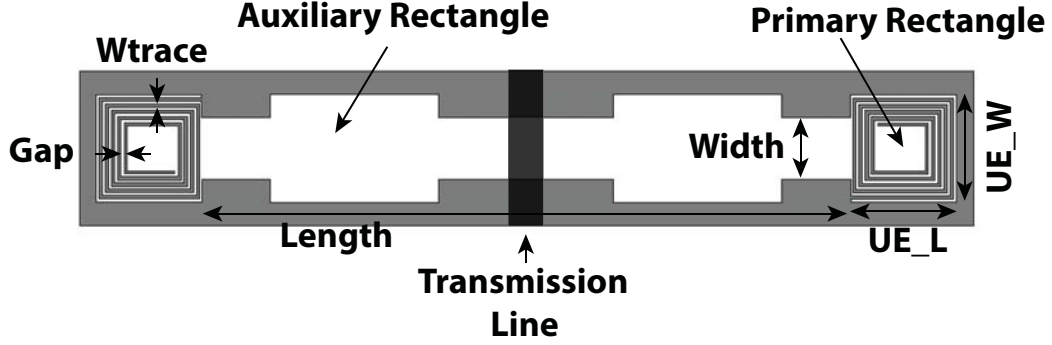


Figure 5.1: Test setup for DGS

5.2.2 Parametric Analysis of Proposed DGS

This section describes the detailed analysis and design procedure of the proposed DGS. The parametric study of the length, width and size of the primary and auxiliary rectangles and gap of the spiral describe the behaviour of the proposed DGS.

The stop-band center frequency of the DGS decreases with the increase in the structure length(Length). The larger the length, the lower is the stop-band of the DGS as shown in Figure 5.2. For this figure the dimensions of the primary rectangles and secondary auxiliary rectangles are $6.77 \times 6.77 \text{ mm}^2$ and $7 \times 16 \text{ mm}^2$, respectively and the width of the DGS is 4.5 mm . The DGS is not loaded with spirals and the length is varied from 40 mm to 60 mm with step size of 10 mm .

The width of the DGS (width) has an inverse effect on the stop-band characteristics. Increasing the width shifts the stop-band to higher frequencies. This effect is shown in Figure 5.3. For this figure the dimensions of the primary rectangles and auxiliary rectangles are $6.77 \times 6.77 \text{ mm}^2$ and $7 \times 16 \text{ mm}^2$, respectively and the Length of the DGS is 40 mm . The DGS is not loaded with spirals and the

width is investigated at 1,3 and 4.5mm. Please note that this DGS is to be placed between the two antennas and the DGS should not exceed 10mm in width.

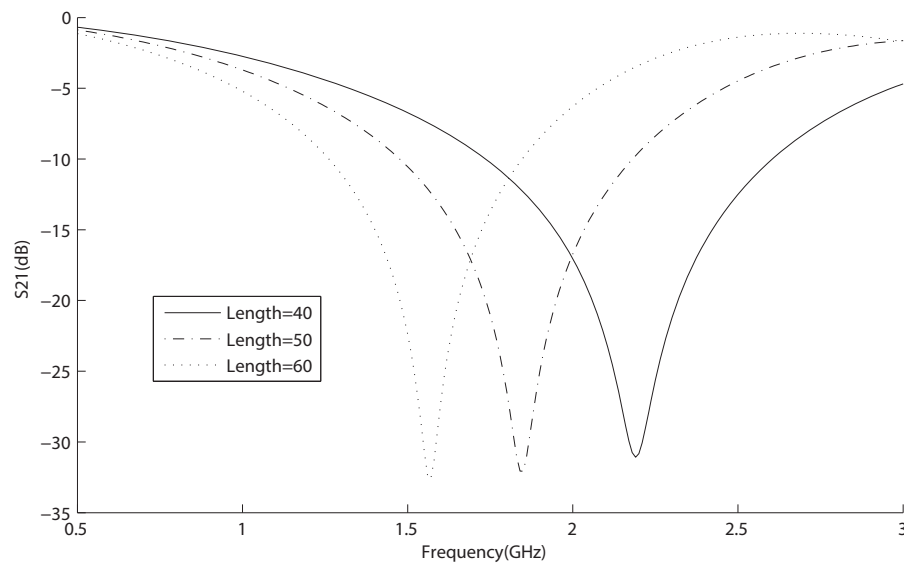


Figure 5.2: Effect of the DGS length on the stop band frequency; primary rectangles= $6.67 \times 6.67mm^2$; auxiliary rectangle= $7 \times 16mm^2$; width=4.5mm.

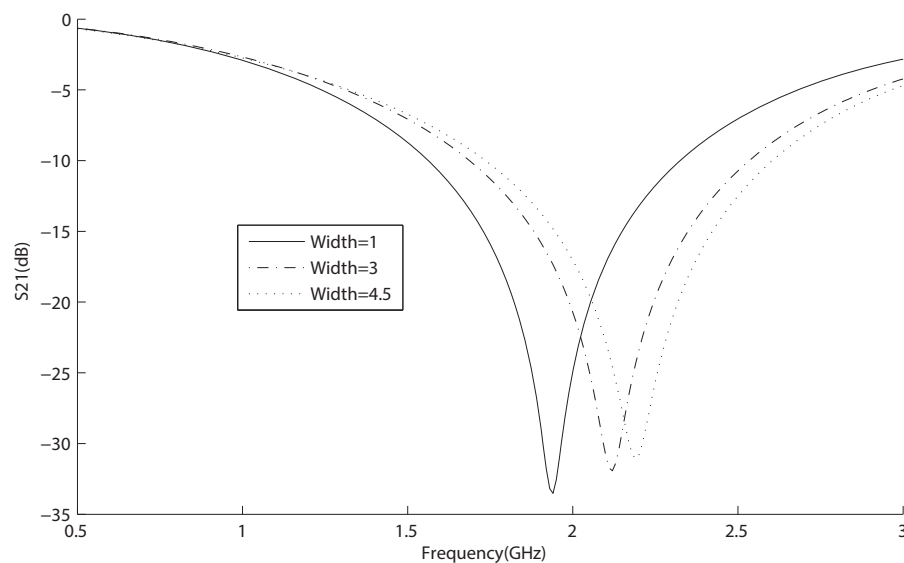


Figure 5.3: Effect of the DGS width on the stop band frequency; primary rectangles= $6.67 \times 6.67mm^2$; auxiliary rectangle= $7 \times 16mm^2$; length=40mm.

Similarly the smaller the size of primary rectangles, the higher is the stop-band center frequency. This effect is shown in Figure 5.4 . For this figure the dimensions of the secondary rectangles is $7 \times 16mm^2$. The Length and width of the DGS are 40 and $4.5mm$. The DGS is not loaded with spirals and the investigated primary rectangle sizes are 6.77×6.77 , 8×8 and $10 \times 10mm^2$.

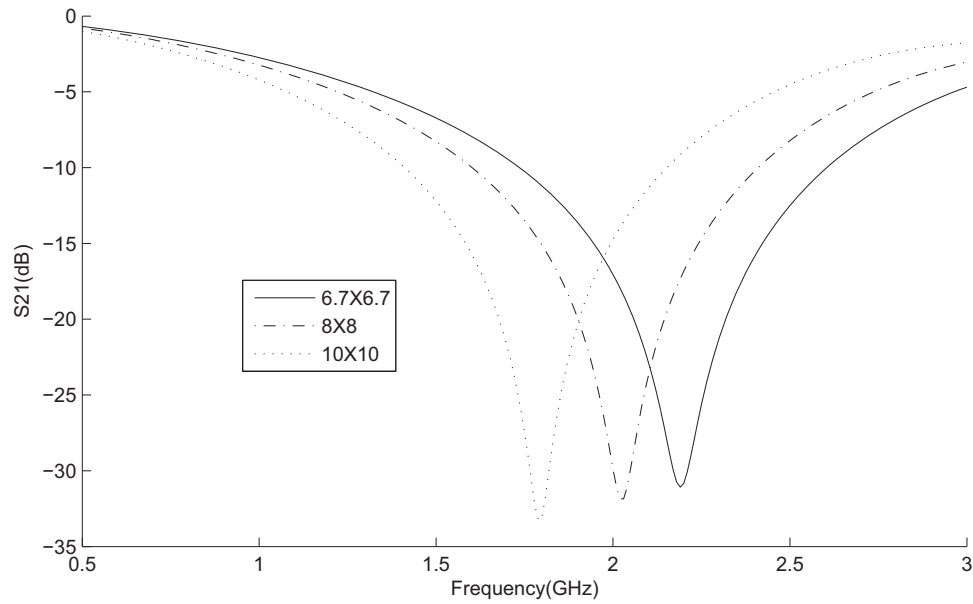


Figure 5.4: Effect of the primary rectangle size on the stop band frequency; auxiliary rectangle= $7 \times 16mm^2$; width= $4.5mm$; length= $40mm$.

The size of the DGS is very important as it has to cover the whole coupling area. If the DGS is smaller than the coupling area then the coupling fields may escape the DGS and cause low isolation. This factor defines the length of the dumbbell. At this length, the stop-band center frequency of the structure is lower than the resonance frequency of the high band as the stop-band frequency reduces with

the increase in the length of the dumbbell. To increase this frequency, we have to either increase the width or lower the size of primary rectangular. The width of the DGS cannot be increased beyond the width of the primary rectangle as in this case the structure will no longer remain dumbbell shaped. Secondly increasing the width has very little effect on the stop-band center frequency after a specific value. So the width cannot be increased above this value. Similarly the dimensions of the primary rectangles cannot be lowered beyond certain values as the primary rectangles are to be loaded with the spiral to handle the low band isolation.

Because the length and width of the dumbbell do not allow tuning the DGS at the desired frequency, the auxiliary rectangles are introduced. The dimensions of auxiliary rectangles can be varied without any limitation (as long as it does not alter the overall geometry). Increasing the dimensions of the auxiliary rectangles increases the stop-band center frequency as shown in Figure 5.5. For this figure the dimensions of the primary rectangles are $6.77 \times 6.77mm^2$. The Length and width of the DGS are 40 and 4.5mm. The DGS is not loaded with spirals and the investigated primary rectangle sizes are 7×7 , 7×10 and $7 \times 16mm^2$. Hence using the length, width and the dimensions of the auxiliary rectangles, the stop-band of the DGS is fine tuned according to the high band resonance frequency of the 4-shaped antenna. As mentioned earlier, a DGS adds capacitance (C) and inductance (L) to the structure. These L and C are used to realize a band-stop filter to enhance the isolation. Furthermore the stop-band center frequency, associated with the DGS, is inversely proportional to the values of L and C.

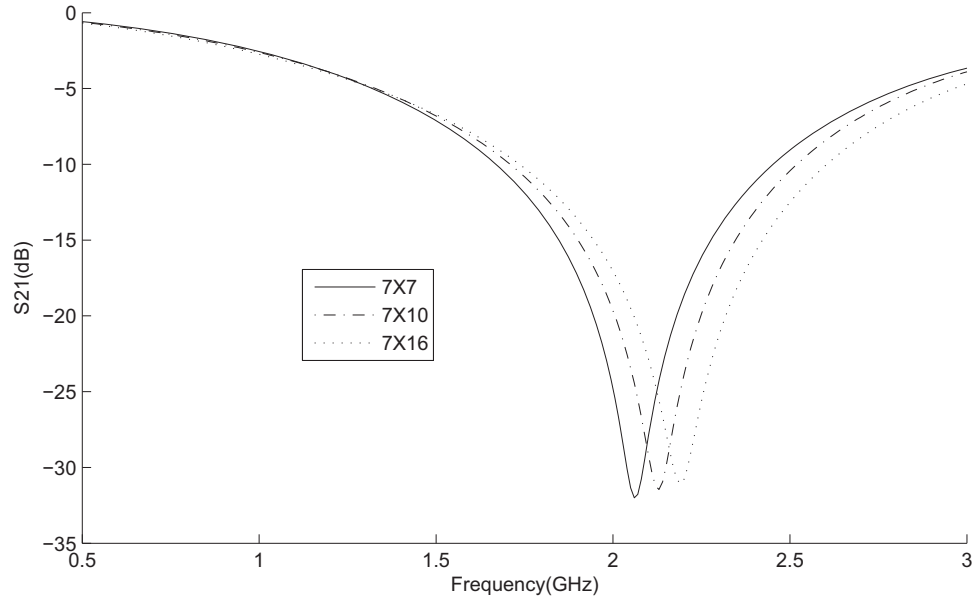


Figure 5.5: Effect of the auxiliary rectangle size on the stop band frequency; primary rectangles= $6.67 \times 6.67mm^2$;length= $40mm$;width= $4.5mm$..

This means we have to have large values of L and C to address the low band of the 4-shaped antenna. To have a high value of L and C, we need to add some complicated structure to the antenna system as done in [46]. To realize a low frequency band-stop filter, a spiral is added to the DGS. The spiral is designed to resonate at the required frequency (approximately $800MHz$).

Once the spiral is designed, the DGS primary rectangles are loaded with this spiral and tested on the test setup. After some tuning, the desired dual-band band-stop filter characteristics were obtained using DGS. The test setup S-parameters of this DGS are shown in Figure 5.6. For this figure the dimensions of the primary rectangles and secondary rectangles are $6.77 \times 6.77mm^2$ and $7 \times 16mm^2$, respectively. The width and length of the DGS are $4.5mm$ and $40mm$, respectively. The DGS is loaded with spirals and the gap for the spiral (as shown in Figure 5.1) is

varied from $2mm$ to $3mm$ with step size of $0.5mm$.

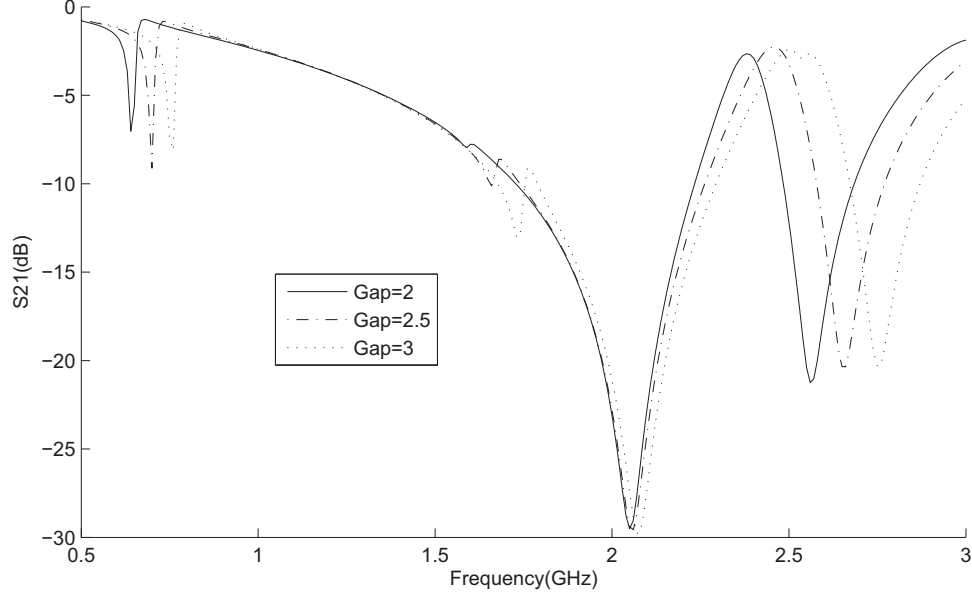


Figure 5.6: Behaviour of spiral loaded modified DGS; primary rectangles= $6.67 \times 6.67mm^2$; auxiliary rectangle= $7 \times 16mm^2$; length= $40mm$; width= $4.5mm$.

There are two stop-bands, one at about $700MHz$ and the other at $2.1GHz$. The third stop-band at approximately $2.6GHz$ is due to higher order modes band-gaps provided by the metamaterial due to its resonant type UE. Here the "Gap" of the spiral is varied. The variation of the low-band stop-band center frequency conforms that this stop-band is the result of loading the DGS with the spiral. This DGS is applied to the antenna structure. Tuning is required again, as the field distribution on the antenna structure is different from that of the test setup. After some tuning, the desired results were achieved.

5.2.3 MIMO Antenna System with Proposed DGS

The model for the antenna structure with DGS is shown in Figure 5.7. This figure shows top and bottom side of two layer FR-4 substrate with 1.56mm thickness and 4.4 dielectric constant. The enlarged view of the spiral is also included in the figure to describe its structural details. The dimensions of the antenna system are (in mm) : $W=50$, $L=100$, $H=13.55$, $Xa2=1.67$, $Lf=15.3$, $Xs=1.0446$, $Xf=2.1716$, $Wt=2.2$, $L1=35.75$, $L2=28$, $Ys=4.5$, $Yf1=14.5$, $Yf2=13.44$, $Yf3=20.56$, $Wf=2.5$, $Wtr=0.7$, $W50=3$, $Y1=6.23$, $Y2=7$, $Y3=16$, $Y4=8$, $Y=52$, $W1=11$, $W2=7$, $W3=3$, $UE_L=6.77$, $UE_W=6.77$, $Wtrace = 0.2$, $Gap = 0.127$. The fabricated antenna model is shown in Figure 5.8. This model is denoted as Model.B.

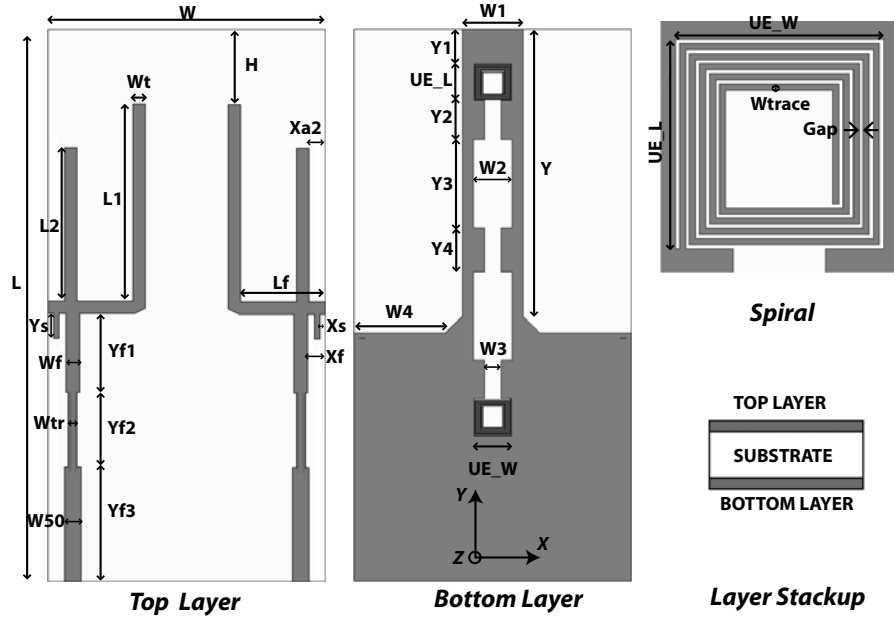


Figure 5.7: Simulation model for Model.B.

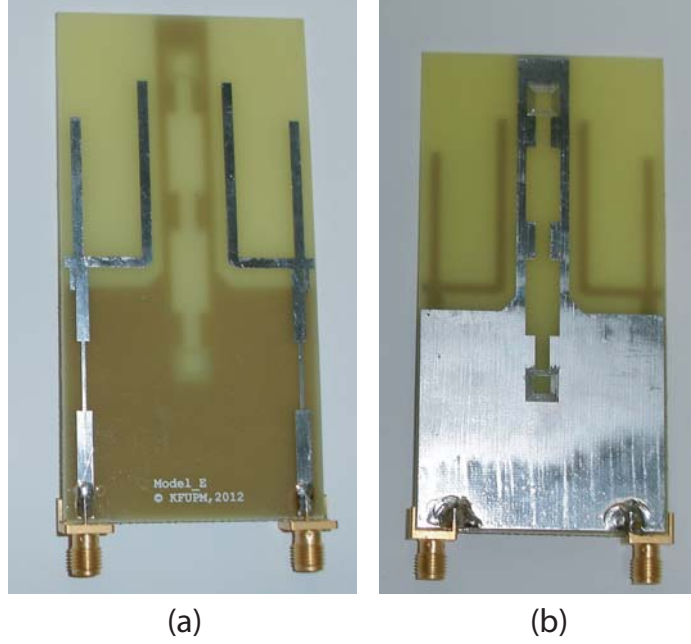


Figure 5.8: Fabricated prototype for Model_B (a)Top (b)Bottom.

5.2.4 Results and Discussion

The prototype is practically fabricated and experimental data is presented in this section except the radiation efficiency that is determined using simulator due to lack of resources to accurately measure the radiation efficiency. The S-parameters of the Model_B are shown in Figures 5.9 and 5.10 for low band and high band, respectively. These figures show the simulated and experimental results. The minimum isolation for the low band was $17dB$ as compare to $3dB$ isolation of the original antenna system in [47] and $9.8dB$ of Model_A described in Chapter 4. Similarly the minimum isolation for the high band was $9.8dB$ as compare to $5dB$ in the original antenna system in [47] and $7dB$ in Model_A. The results show improvement in isolation for both bands of operation. Furthermore, the band-

width for the low-band and high-band were 20MHz and 530MHz respectively. The introduction of the DGS lowered the lowband bandwidth from 30MHz to 20MHz . This inverse relationship between the bandwidth and isolation can also be observed in literature [50].

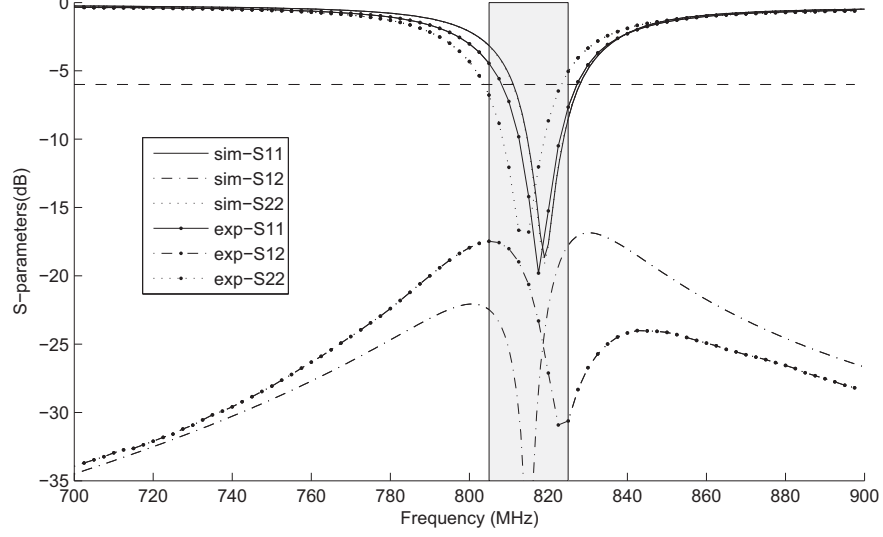


Figure 5.9: Low band S-parameters for Model.B.

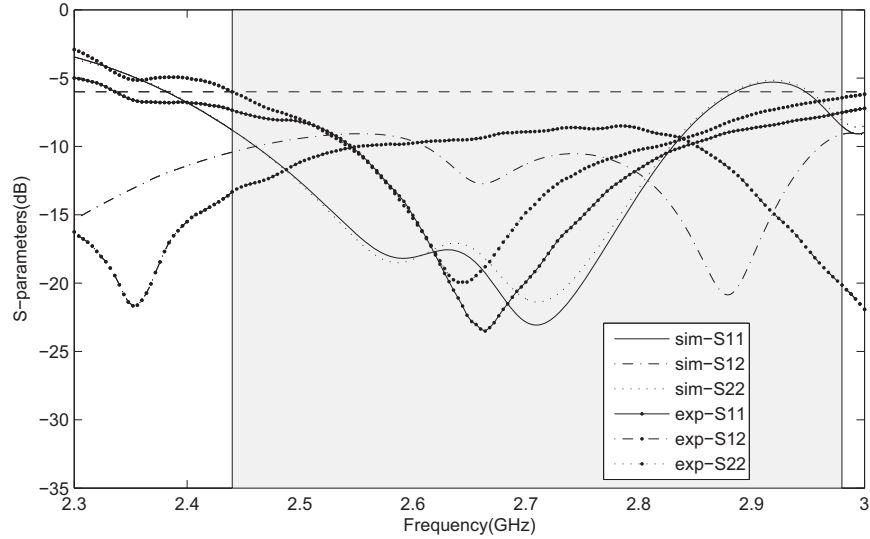


Figure 5.10: High band S-parameters for Model.B.

TARC was also calculated for both bands using Equation (2.11). This is shown in Figures 5.11 and 5.12 for both operating bands. The low band shows stable operation with the change in the input phase. The variations in the high band are better than Model_A as they cover more percentage of the operating bandwidth.

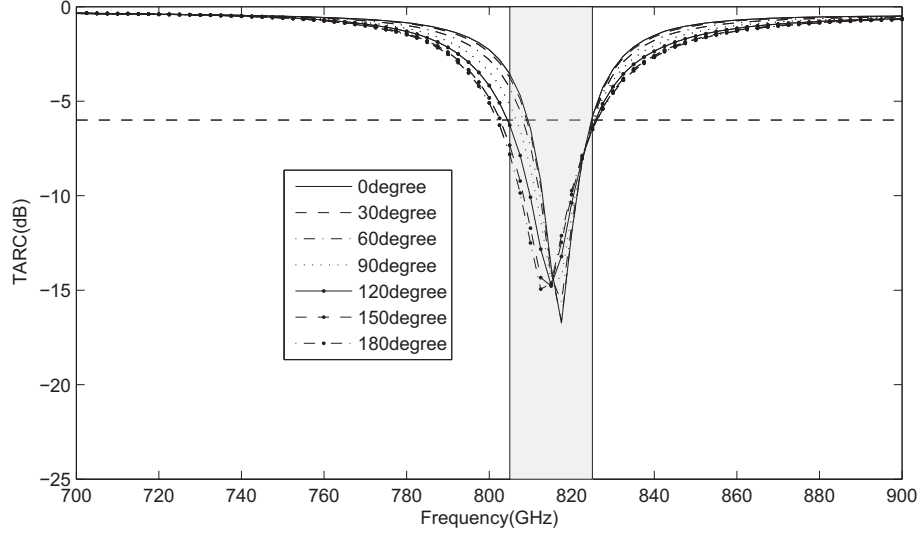


Figure 5.11: Low band TARC for Model_B.

The correlation coefficient is also calculated using Equation (2.2). These curves are shown in Figures 5.13 and 5.14 for both bands. These figures show that the correlation coefficient is within the allowable range throughout the band of operation. Improvement in correlation coefficient can be observed from 0.35 to 0.23 as compared to high band of Model_A (Figure 4.8).

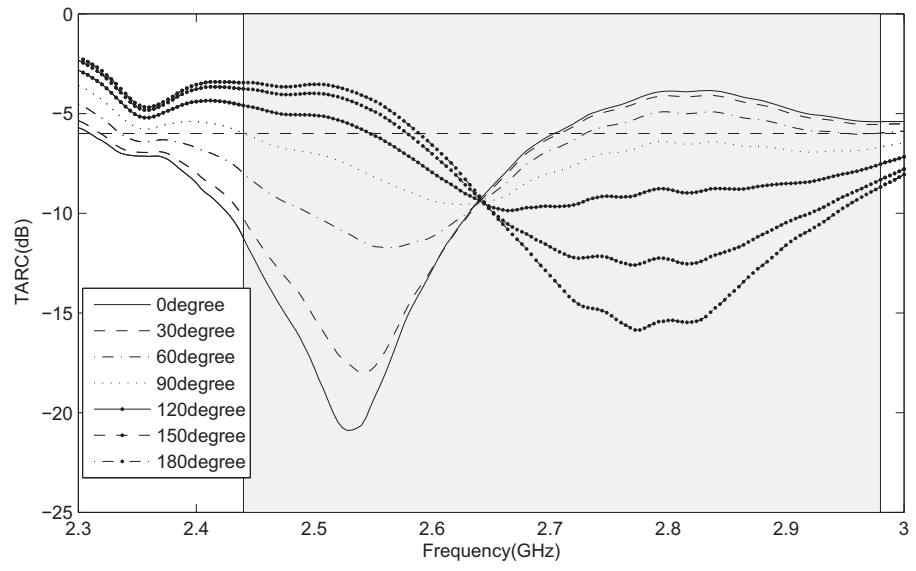


Figure 5.12: High band TARC for Model.B.

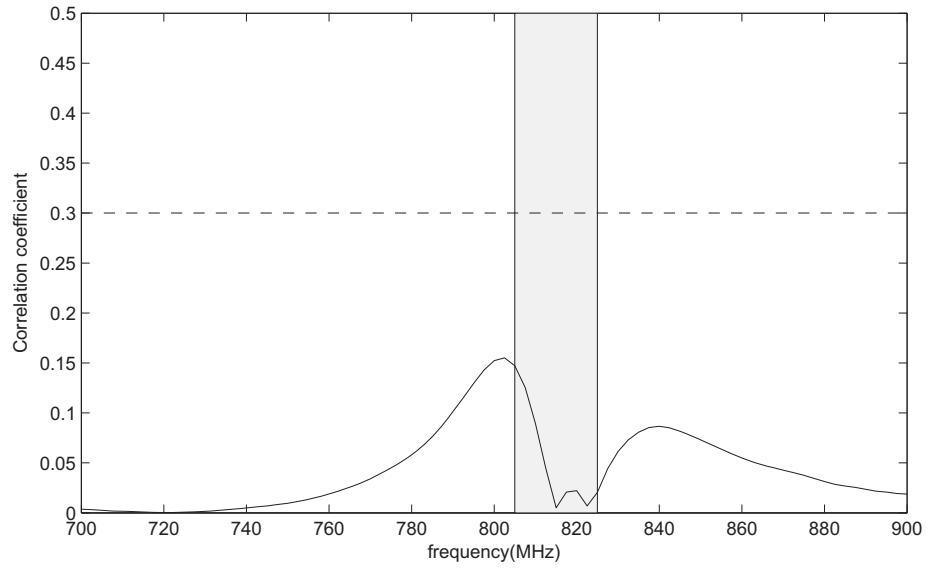


Figure 5.13: Low band correlation coefficient for Model.B.

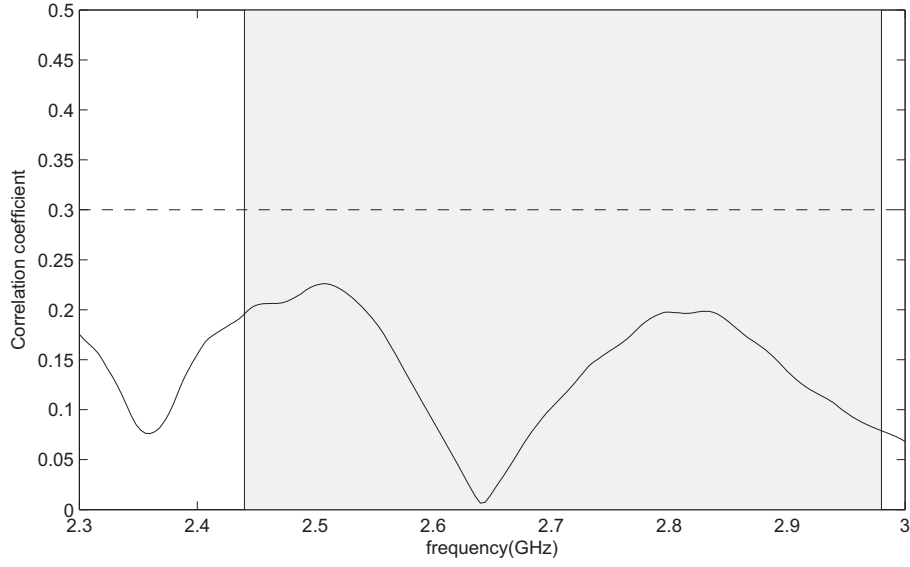


Figure 5.14: High band correlation coefficient for Model_B.

The current distribution of Model_B is shown in Figures 5.15 and 5.16 at $820MHz$ and $2.65GHz$. In comparison with the current distribution of Model_A, significant difference can be observed. For low band, the current distribution is almost identical for both 4-shaped radiators in case of Model_A (Figure 4.9) where as in Figure 5.15, the current distribution on the terminated radiator is much less (darker) as compared to the current distribution on the excited radiator. This reduction in current on the terminated radiator has improved the isolation. Same argument also applies to high band current distribution comparison of Model_A (Figure 4.10) and Model_B (Figure 5.16).



Figure 5.15: Current distribution for Model_B at $820MHz$.



Figure 5.16: Current distribution for Model_B at $2.65GHz$.

The 2D cuts of the measured gain pattern are shown in Figure 5.17. The maximum measured gain was -4dBi and 2.4dBi for the low band and high band respectively. Figures 5.17(a) and 5.17(b) show the principle plane cuts of the measured gain patterns for Element 1 and 2 for co-polarization (gain theta) and cross polarization (gain phi) at 820MHz . Similarly Figures 5.17(c) and 5.17(d) show the principle plane cuts of the measured gain patterns for Element 1 and 2 for co-polarization and cross polarization at 2.65GHz . The measurements were conducted at an outdoor antenna range facility at Oakland University, Michigan, USA.

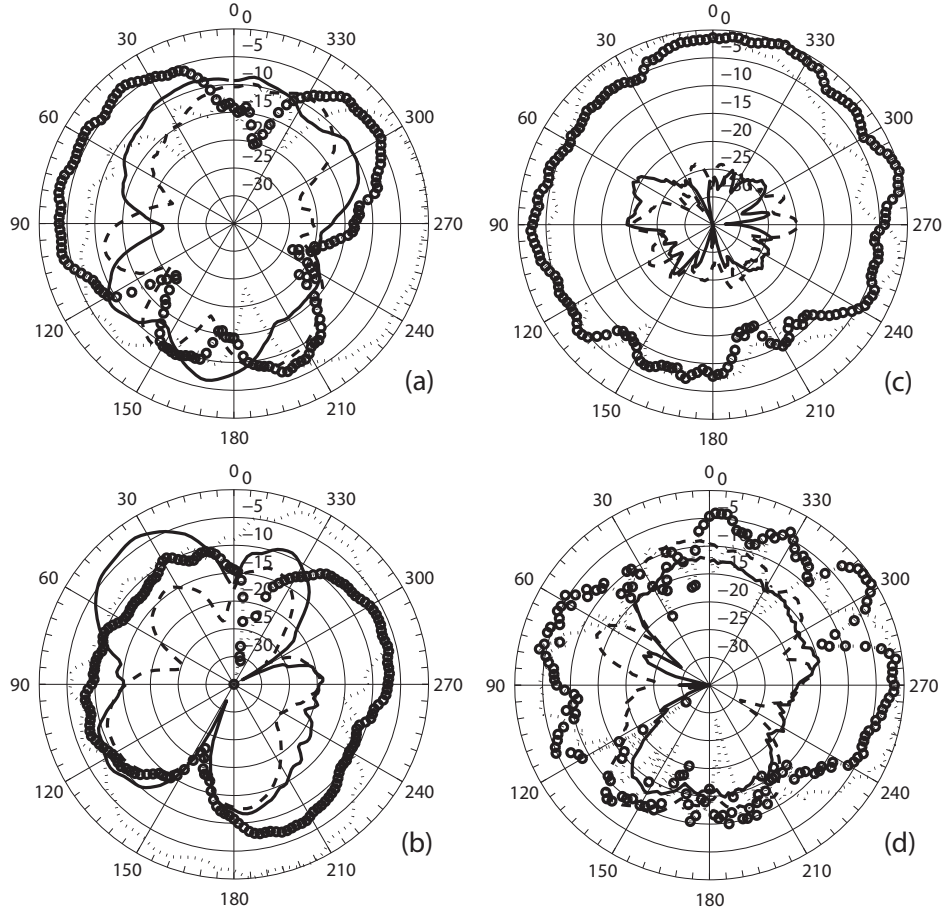


Figure 5.17: Measured gain patterns for Model B. Dots:vertical polarization for element 1, Circles:vertical polarization for element 2, Solid:horizontal element 1, Dashes:horizontal polarization element 2.

MEG values are calculated according to Equation (2.8) using simulated gain patterns. The calculated MEG for Model_B for the low band with cross-polarization discrimination (Γ) of $0dB$ were $MEG1_{LOW} = -1.24dB$ and $MEG2_{LOW} = -1.265dB$, for elements 1 and 2, respectively. For the high band, the values were $MEG1_{HIGH} = -1.27dB$ and $MEG2_{HIGH} = -1.1848dB$, for elements 1 and 2, respectively. With a Γ value of $6dB$, the values were $MEG1_{LOW} = -1.233dB$, $MEG2_{LOW} = -1.258dB$, $MEG1_{HIGH} = -1.279dB$ and $MEG2_{HIGH} = -1.1933dB$, for the low and high bands of elements 1 and 2. It is evident that the ratio of $MEG1/MEG2 < 3dB$ at both bands of operation with both Γ values that provides acceptable diversity gain. The performance parameters for Model_B are summarized in Table 5.1.

Table 5.1: Summary for Model_B performance parameters

Parameters	Low-Band	High-Band
Bandwidth (-6dB)	805-825MHz	2.45-2.98GHz
Maximum Gain	-4dBi	2.4dBi
Minimum isolation	17dB	9dB
Efficiency(η)	40%	67%
Correlation Coefficient	0.15	0.23
MEG1($\Gamma = 0$)	-1.24dB	-1.27dB
MEG1($\Gamma = 6dB$)	-1.233dB	-1.279dB
MEG2($\Gamma = 0$)	-1.265dB	-1.1848dB
MEG2($\Gamma = 6dB$)	-1.258dB	-1.1933dB

5.3 Neutralization Line (NL) based Isolation Enhancement Structure

As mentioned in Section 3.5, the NL can enhance the isolation by eliminating the coupling currents on the structure of the radiating elements. Consider a two radiating elements MIMO antenna system in which one element is excited and the other is terminated to a matched load. The excited element may induce currents on the terminated radiator. This induction of the currents can increase the correlation between the signals received by the two radiators. If the isolation is reduced by the induction of the currents due to nearby excited radiating element then the isolation can be improved by cancelling these currents. NL is such a technique in which we take current at a specific location on excited radiating element, invert its phase by selecting appropriate length for NL and then feeding this current to nearby radiator to enhance its isolation.

The selection of the point is critical in this technique. The point should be selected that is at minimum impedance so that it has maximum current. The effective bandwidth of the NL technique depends on the variation of impedance of the selected point. So a low impedance point on the structure of the radiating element with stable impedance throughout the band of operation is selected as a starting point of the NL.

The NL technique is a very simple method to enhance the isolation but it has certain limitations. First, the selection of the point on the radiator structure is a complicated task. Detailed analysis of the current distribution on the radiator's

structure is required to properly select this point. Secondly, radiation mechanism of the radiator may also limit the effectiveness of this technique. In some cases, in addition to the structure of the radiating element, the ground plane also plays a major role in the radiation. So cancelling currents only on the radiating structure does not have any effect on the overall isolation of the antenna system.

5.3.1 MIMO Antenna System with NL Based Isolation Enhancement Structure

Model_A with neutralization line is shown in Figure 5.18. The location of NL is selected by studying the current distribution profile of the radiating elements. Point with maximum current and minimum variation of the current throughout the band of operation is selected to be connected through NL. The dimensions of reference model with NL are (in mm): $W = 50$, $L = 100$, $W_t = 2.2$, $H = 2.5493$, $L_1 = 40.75$, $L_2 = 27$, $Y_s = 5.5$, $X_{a2} = 1.6716$, $L_f = 15.8$, $X_s = 0.6716$, $X_f = 2.6716$, $W_f = 2.5$, $W_s = 1$, $Y_f = 15.5$, $W_1 = 10$, $Y = 46$, $W_2 = 17$, $W_{nl}=0.2$, $H_{ax}=0$, $H_{nl}=8$, $L_{nl}=37.86$. The substrate used is an FR-4 with $1.56mm$ thickness and 4.4 dielectric constant. The antenna model was optimized using $HFSS^{TM}$ for the high band. This model is denoted by Model_C from now onwards.

5.3.2 Results and Discussion

Before analyzing the results it is important to understand the radiation mechanism of the 4-shaped MIMO antenna system. The antenna radiates at approximately

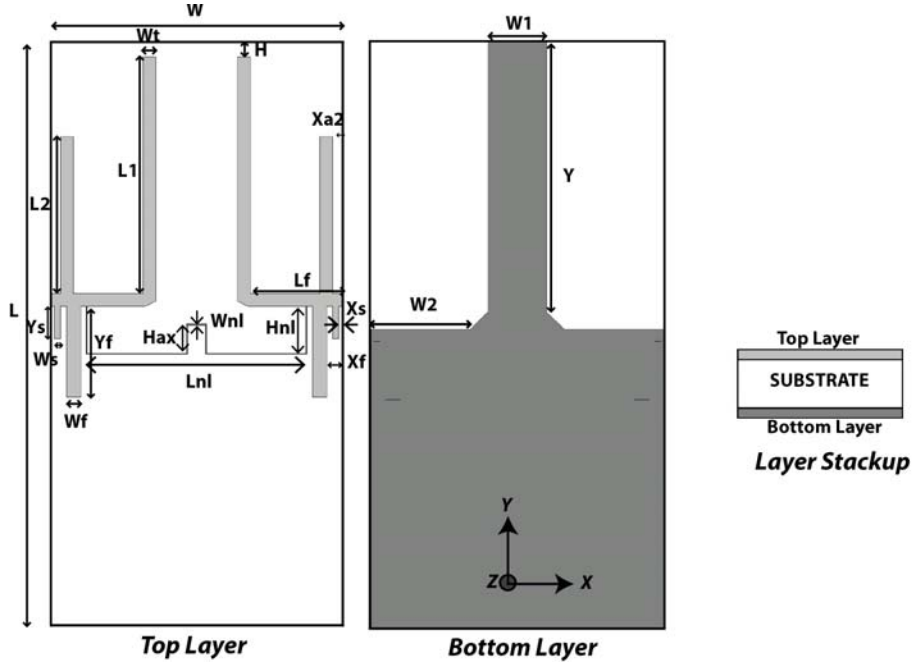


Figure 5.18: Antenna model with neutralization line (Model.C)

775MHz and 2.54GHz. At the lower resonance frequency, the antenna system behaves as an electrically small antenna ($ka < 1$). So at this resonance frequency the ground plane becomes a part of radiating structures along with the 4-shaped structures. So it is expected that the NL technique will not be able to enhance the isolation at the low resonance frequency.

More meaningful conclusions can be drawn if the S-parameters are analyzed along with the current distribution. The S-parameter curves are shown in Figures 5.19 and 5.20 for low-band and high-band, respectively.

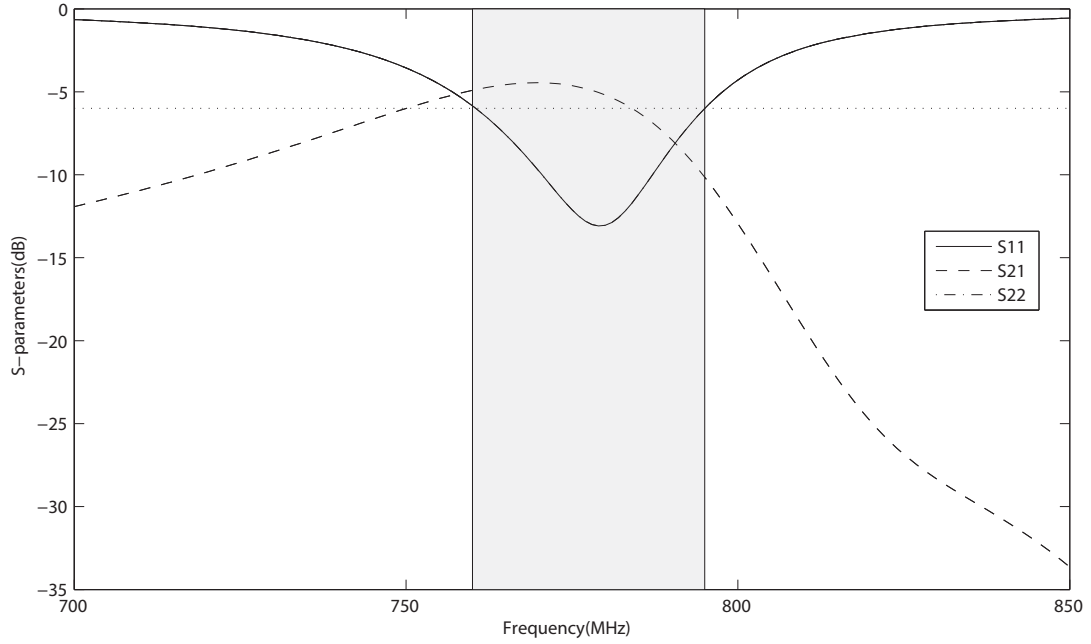


Figure 5.19: Low band S-parameters for Model_C.

It can be observed that there is no improvement in low band isolation but high band isolation is improved from 7.2dB (Figure 4.4) to approximately 11dB (Figure 5.20). The operation of the NL can be understood using the current distribution on 4-shaped radiators' structures at high resonance frequency as shown in Figure 5.21. In this figure, each antenna system (with or without NL) consists of one excited radiator (right radiator) and one terminated radiator (left radiator). The amount of current on the unexcited radiator is less (darker) for Model_C as compared to Model_A. This reduction in current gives 4dB isolation improvement.

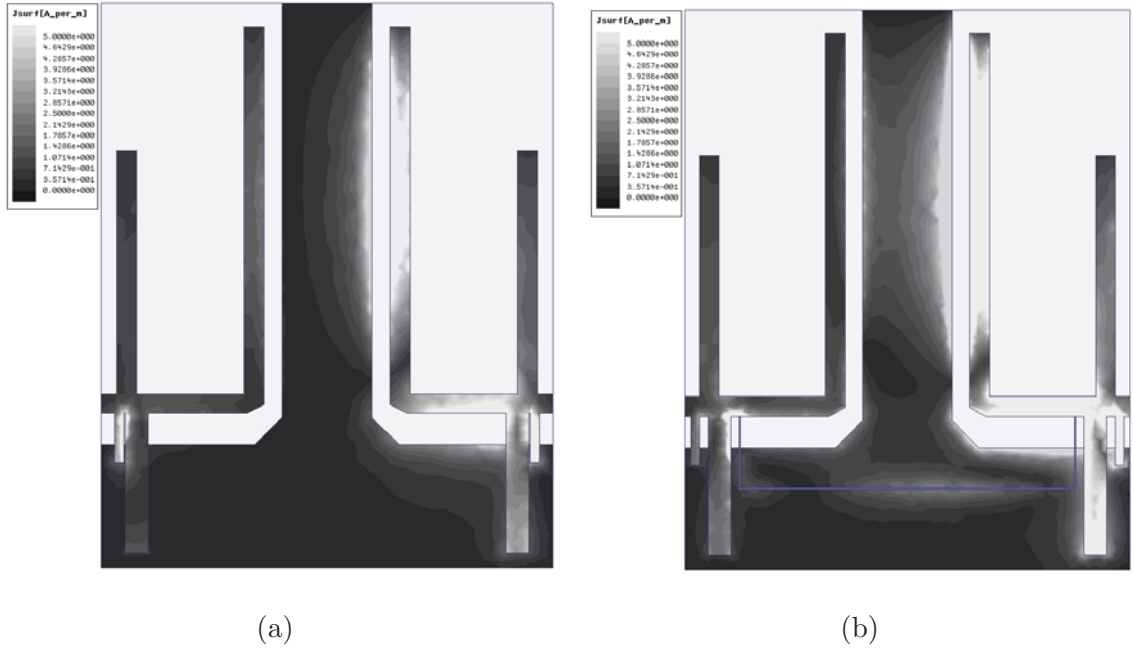


Figure 5.21: Current distribution at $2.54GHz$, (a) Model_A (b) Model_C

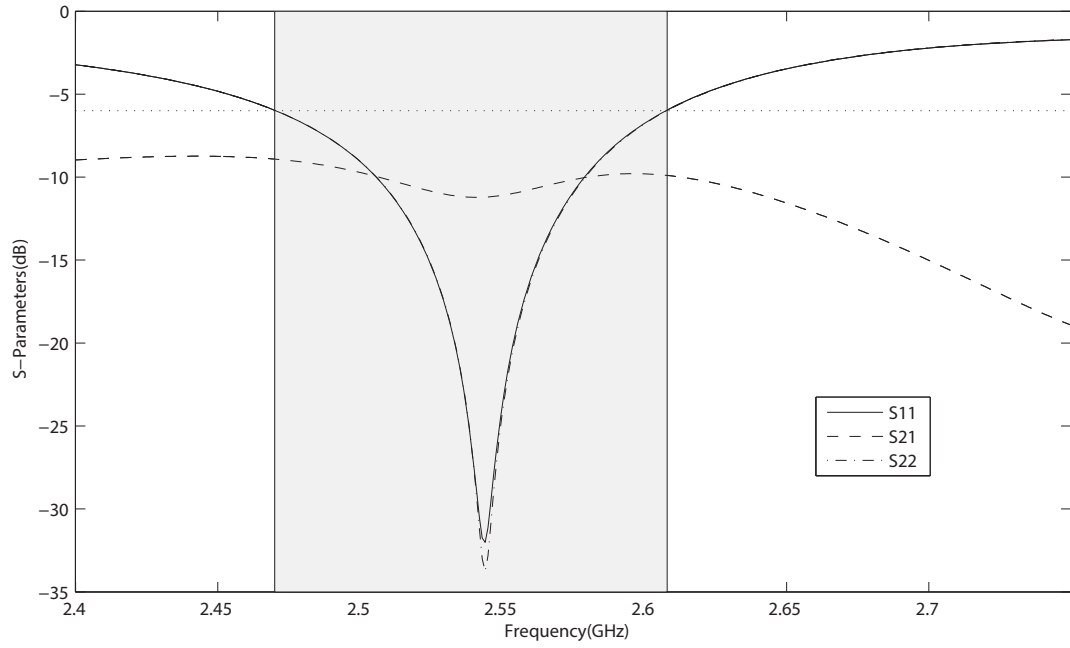


Figure 5.20: High band S-parameters for Model_C.

The failure of the NL technique for enhancing isolation at low-band can be ob-

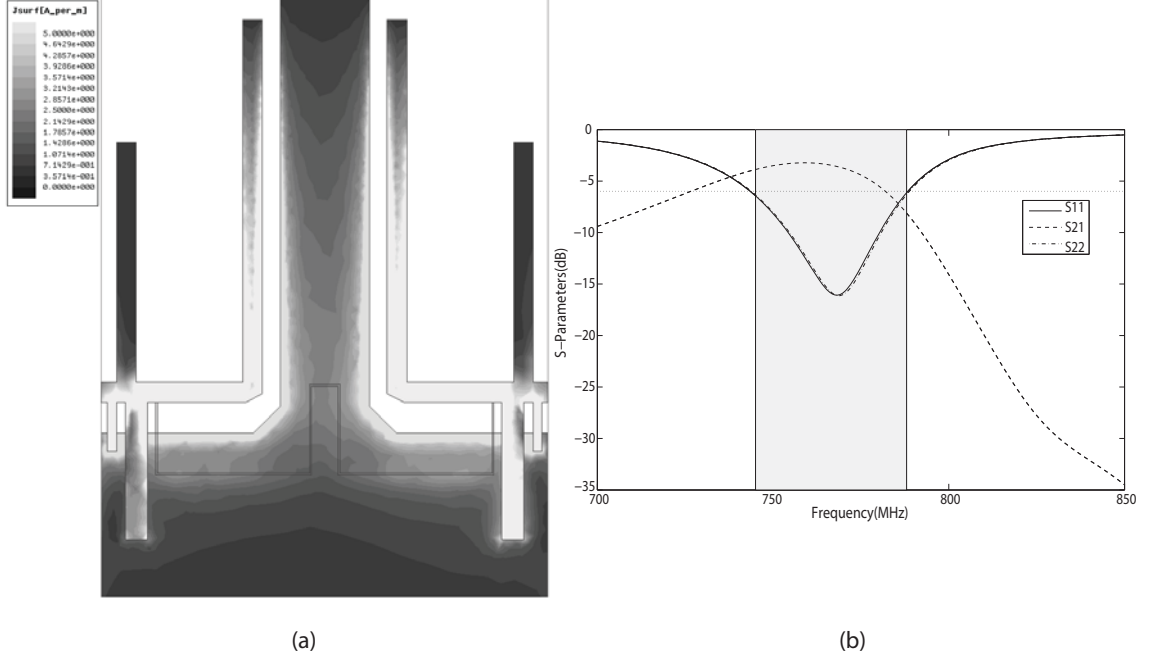


Figure 5.22: Response of Model_C at $774MHz$, $H_{ax}=10mm$, (a) Current distribution (b) S-parameters

served in Figures 5.22-5.24. These figures show that in spite of the significant reduction of current in the terminated radiating element, there is no improvement in isolation. This verifies that the 4-shaped radiating elements are not the only structures contributing to radiation at the low-band and hence the ground plane is also a part of the radiating structure. So in order to improve the isolation, ground plane currents should also be considered.

The antenna parameters are extracted from the simulation model. The minimum isolation level is 4.45 and $11.2dB$ for the low and high band. The isolation at the low band is not acceptable for MIMO application. The range of the low band is 760 to $795MHz$ providing $-6dB$ bandwidth of $35MHz$. For high band, the range is 2.47 to $2.6GHz$ with $-6dB$ bandwidth of approximately $130MHz$. The maximum correlation coefficient, calculated using simulated S-parameters in

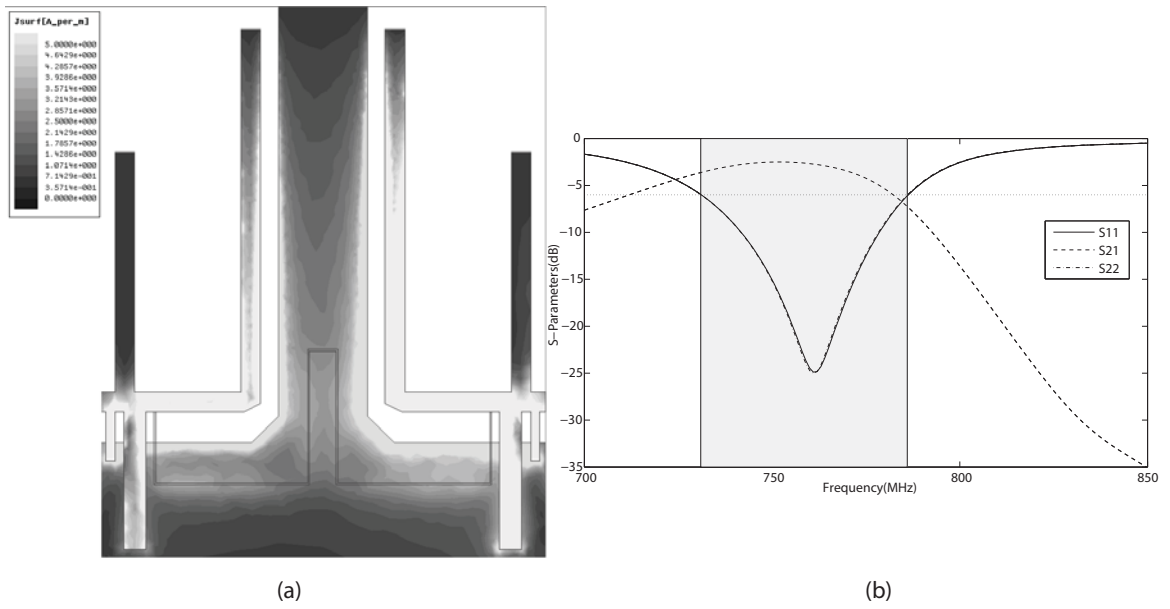


Figure 5.23: Response of Model_C at 774MHz , $H_{ax}=15\text{mm}$, (a) Current distribution (b) S-parameters

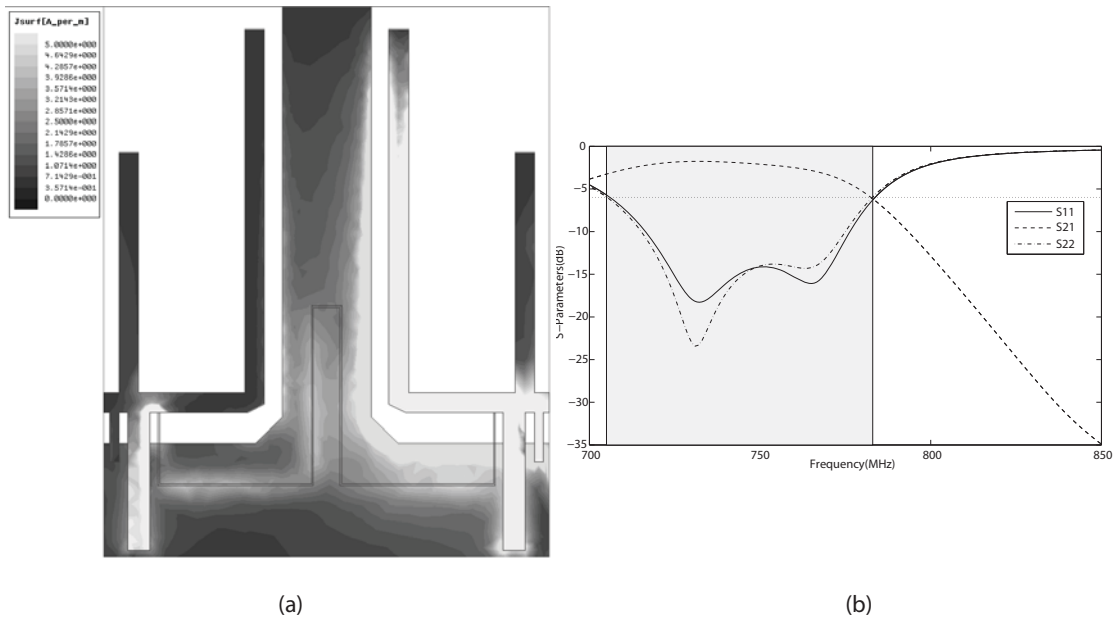


Figure 5.24: Response at of Model_C 774MHz , $H_{ax}=20\text{mm}$, (a) Current distribution (b) S-parameters

Equation (2.2), values are 0.27 and 0.23 for the low and high bands. The high correlation coefficient, especially at the low band, is due to low isolation. The simulated maximum gain is -0.3dBi and 4dBi for the low and high bands, respectively. Maximum simulated radiation efficiency is 37% and 68% for low and high bands, respectively.

MEG values are calculated using Equation (2.8) and simulated gain patterns. The calculated MEG for Model_C for the low band with cross-polarization discrimination (Γ) of 0dB were $MEG1_{LOW} = -1.86\text{dB}$ and $MEG2_{LOW} = -1.886\text{dB}$, for elements 1 and 2, respectively. For the high band, the values were $MEG1_{HIGH} = 0.8543\text{dB}$ and $MEG2_{LOW} = 0.7891\text{dB}$, for elements 1 and 2, respectively. With a Γ value of 6dB , the values were $MEG1_{LOW} = -1.8474\text{dB}$, $MEG2_{LOW} = -1.874\text{dB}$, $MEG1_{HIGH} = 0.8394\text{dB}$ and $MEG2_{HIGH} = 0.7742\text{dB}$, for the low and high bands of elements 1 and 2. Significant high value of MEG for high band is due to the radiation pattern of Model_C. The simulated radiation pattern of this model shows high antenna gain value at $\theta_1 = 0^\circ$ that, when used in Equation (2.8), results in high value of MEG as compared to low band and other models. The performance parameters for Model_C are summarized in Table 5.2.

5.4 Summary

In this chapter, we analyzed two non-metamaterial based isolation structures. The first structure was a defected ground structure (DGS) and the second one was a neutralization line (NL). Model_A with DGS is denoted as Model_B and

Table 5.2: Summary for Model_C performance parameters

Parameters	Low-Band	High-Band
Bandwidth(-6dB)	760-795MHz	2.47-2.6GHz
Maximum Gain	-0.3dBi	4dBi
Minimum isolation	4.45dB	11.2dB
Efficiency(η)	37%	68%
Correlation Coefficient	0.27	0.23
MEG1($\Gamma = 0$)	-1.86dB	0.8543dB
MEG1($\Gamma = 6dB$)	-1.8474dB	0.8394dB
MEG2($\Gamma = 0$)	-1.886dB	0.7891dB
MEG2($\Gamma = 6dB$)	-1.874dB	0.7742dB

Model_A with NL is denoted as Model_C. The DGS is a modified dumbbell shaped structure. The parametric analysis of the DGS is also presented to provide the understanding of the behaviour of the DGS and how it was optimized to cover both bands of Model_A to improve its isolation.

Insertion of the DGS improved the minimum isolation level from $9.5dB$ to $17dB$ whereas the isolation level degraded from approximately $7dB$ (simulated) to $4.45dB$ (simulated) for the case of the NL. The DGS has improved the isolation by approximately $2dB$ in the higher band as well. The DGS did not effect the radiation efficiency at the low band whereas approximately 8% reduction in the radiation efficiency is observed at the high band. On the other hand, the NL reduced the radiation efficiency by approximately 3% and 7% for low and high bands, respectively. The DGS reduced the $-6dB$ bandwidth by approximately $10MHz$ for the low band whereas significant improvement in the bandwidth is observed in the high band. In addition to these performance parameters correlation coefficient, total active reflection (TARC), maximum antenna gain and mean effective gain (MEG) are also analyzed to evaluate the performance of the antenna

system with non-metamaterial based isolation enhancement structures.

CHAPTER 6

METAMATERIAL BASED ISOLATION ENHANCEMENT STRUCTURES

6.1 Introduction to Metamaterials

Metamaterials are artificially engineered structures that have unique properties that are not found in nature i.e. negative permittivity and/or negative permeability. Negative permeability means that the material is forcing the magnetic field density (B) to be opposite in direction relative to magnetic field intensity (H). Similarly negative permittivity material causes the electric field density (D) to be opposite in direction relative to electric field intensity (E). These properties force the wave passing through the material to follow the left hand rule instead of the right hand rule that governs the propagation of the wave in natural materials and

hence these materials are known as left hand (LH) materials.

Periodic repetition of any structure that exhibits these unique properties, can realize a metamaterial. The periodic repetition is a general but not an essential condition for the formation of metamaterials. These structures are basic building blocks for the metamaterials and hence known as the unit element (UE) or the unit cell (UC) of the metamaterial. Split Ring Resonators (SRRs) and Capacitively Loaded Loops (CLLs) are common examples of such structures. Along with these, chiral materials can also be used to make the materials refractive index negative without making the permittivity and permeability simultaneously negative [51]. A resonating structure can also be used as a UE to realize a metamaterial [52].

Existing SRRs require a time varying magnetic field to be perpendicular to the structure of the SRR. The varying magnetic field induces time varying currents in the SRR that flow in circular rings of the structure thus create an inductive effect. The time varying currents vanish at the open gap of the SRR and opposite sign charges appear at the other end of the gap. So the gap resembles the introduction of capacitance in the structure. The introduction of an appropriate capacitance and inductance in the structure can make the material a metamaterial. Similarly, the CLLs can also be used to generate negative permeability material [53].

Metamaterials exhibit band gaps that can be used to realize stop-band filters. This property can also be used to isolate closely packed antennas. Metamaterials are used to improve the isolation as described in Chapter 3. In addition to isolation, metamaterials are also used to reduce the antenna dimensions for handheld

and mobile devices [27], i.e. miniaturize antennas.

6.2 Design of an Isolation Enhancement Structure using Capacitively Loaded Loop (CLL) based Metamaterial

6.2.1 Selection of the Unit Element(UE)

The design of a metamaterial starts with proper selection of a UE for the material. In this particular application, the requirements are dual-band with low-band operations and limited size. The selection of the UE depends on the antenna structure size. As the MIMO antenna system cannot exceed a certain size ($50 \times 100mm^2$), the UE should be compact especially at low frequency to fulfill the strict area constraints for MIMO antenna systems.

The isolation structure should increase the isolation in both bands for this particular application. To make the isolation structure dual-band, complementary metamaterial was used on the ground plane to cover the low-band and normal metamaterial was used on the top layer containing the radiating elements to cover the high-band. Complementary metamaterial means that the metamaterial structure is etched out of the ground plane.

6.2.2 The Proposed CLL UE

As described earlier, the UE should be compact and it should have the tendency to be tuned for sub-GHz frequencies. The selected UE was a double spiral array formed by the CLLs due to simple and planar structure[54].

CLLs were introduced in [54]-[55]. They were modeled in [56] using method of moment (MoM) and an interpolation scheme. The resonance frequency is determined by the configuration and physical dimensions of the loops. A metamaterial can be realized by periodically placing copies of the UE. The dimensions of CLL determine the behavior of the metamaterial.

6.2.3 Dispersion Diagram for UE

The UE is characterized by a dispersion diagram. The dispersion diagram describes the relation between propagation constant and frequency along a certain length. Using this dispersion diagram, the band gaps can be identified and the structure dimensions can be tuned to get a band gap at the proper location in the frequency spectrum.

Analytical expression for the Dispersion Diagram [57]

Consider a structure that is periodically repeated after distance “ p ”. For such a structures the fields, after the distance “ p ”, repeat with difference of a complex constant $C = e^{-\gamma p}$ where $\gamma = \gamma(\omega) = \alpha(\omega) + j\beta(\omega)$. α represents the attenuation constant where as β represents the phase constant. Mathematically this

phenomena can be expresses as

$$\frac{\psi(z+p)}{\psi(z)} = \frac{\psi(z+2p)}{\psi(z+p)} = \frac{\psi(z+np)}{\psi(z+[n-1]p)} = C = e^{-\gamma p}, \forall n. \quad (6.1)$$

where $\psi(z)$ is the wave function. Generally this can be written as

$$\psi(z+np) = C^n \psi(z) = e^{-\gamma np} \psi(z) \quad (6.2)$$

This relation represents a periodic boundary condition that is characteristic for a periodic structure. The wave function $\psi(z)$ may be written as

$$\psi(z) = \psi(z+np)e^{\gamma np} \quad (6.3)$$

When multiplied by $e^{\gamma z}$, this expression becomes $\psi(z)e^{\gamma z} = \psi(z+np)e^{\gamma(z+np)}$, which indicates that the left hand side (LHS)

$$\xi_\gamma(z) = \psi(z)e^{+\gamma z} \quad (6.4)$$

is a periodic function of period “ p ” for any complex propagation constant γ .

Consequently, this function can be expanded using the Fourier series

$$\xi(z) = \sum_{-\infty}^{+\infty} \xi_{\gamma n} e^{-j(2n\pi/p)z} \quad (6.5)$$

with the Fourier expansion coefficients

$$\xi_{\gamma n} = \frac{1}{2\pi} \int_{-\pi}^{+\pi} \xi_{\gamma}(z) e^{+j(2n\pi/p)z} dz \quad (6.6)$$

By inserting Equation (6.5) into Equation (6.3) we obtain the expression for the waveform in a periodic structure with period “ p ”

$$\psi_{\gamma}(z) = e^{-\alpha(\omega)z} \sum_{n=-\infty}^{+\infty} \xi_{\gamma n} e^{-j[\beta(\omega)+2n\pi/p]z} = e^{-\alpha(\omega)z} \sum_{n=-\infty}^{+\infty} \xi_{\gamma n} e^{-j\beta_n z} \quad (6.7)$$

where

$$\beta_n = \beta(\omega) + \frac{2n\pi}{p} \quad (6.8)$$

In Equation (6.7), the wave is assumed to propagate in $+z$ direction. However, in general, the wave moves in both directions. Equation (6.7) incorporates this generality

$$\psi_{\gamma}(z) = e^{-\alpha(\omega)z} \sum_{n=-\infty}^{+\infty} \xi_{\gamma n}^+ e^{-j\beta_n z} + e^{+\alpha(\omega)z} \sum_{n=-\infty}^{+\infty} \xi_{\gamma n}^- e^{+j\beta_n z} \quad (6.9)$$

This expression is the mathematical representation for the Bloach-Floquet’s theorem which states that “A wave in a periodic structure consists of the superposition of an infinite number of plane waves, called space harmonic or Bloach-Floquet’s wave”.

Equation (6.9) represents the wave function in 1D. For a general expression,

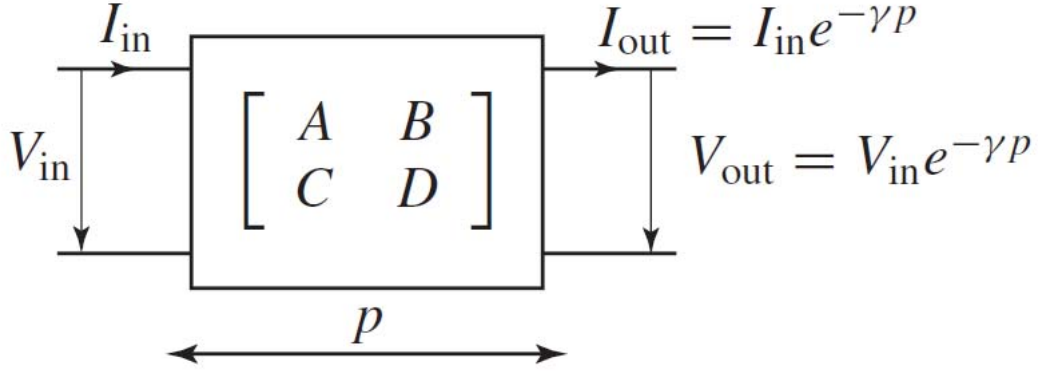


Figure 6.1: Unit Element with [ABCD] parameters [57]

the equation can be written as

$$\psi_{\vec{\gamma}(\vec{r})} = e^{-\vec{\alpha} \cdot \vec{r}} \sum_{\vec{G}} \psi_{\vec{\beta} + \vec{G}} e^{j(\vec{\beta} + \vec{G})} \quad (6.10)$$

where \vec{G} is general lattice vector. The lattice vector represents periodicity in all dimensions. For example a lattice vector in 2D will be a two dimensional vector where each component of the vector represents periodicity in a given direction. The complex propagation constant is also a vector given by $\vec{\gamma} = \vec{\alpha} + j\vec{\beta}$.

To determine the analytic expression for the dispersion diagram, consider a unit element with known [A B C D] matrix as shown in Figure 6.1. The output quantities are related with input quantities through following relation

$$\begin{bmatrix} A & B \\ C & D \end{bmatrix} \begin{bmatrix} V_{in} \\ I_{in} \end{bmatrix} = \psi \begin{bmatrix} V_{in} \\ I_{in} \end{bmatrix} \quad (6.11)$$

This is an eigenvalue system with eigenvalues $\psi_n = e^{+\gamma p}$.

To determine the dispersion relation we need to know the expression for the [A B C D] matrix and solve Equation (6.11) which can be written as

$$\begin{bmatrix} A - e^{\gamma p} & B \\ C & D - e^{\gamma p} \end{bmatrix} \begin{bmatrix} V_{in} \\ I_{in} \end{bmatrix} = \begin{bmatrix} 0 \\ 0 \end{bmatrix} \quad (6.12)$$

For a nontrivial solution, the determinant of this system should be zero. So

$$AD - (A + D)e^{\gamma p} + e^{2\gamma p} - BC = 0 \quad (6.13)$$

The [A B C D] depends on the UE. The matrix for symmetric and asymmetric unit elements of metamaterial formed by an LC ladder network is given in [57].

The general dispersion relation is given by

$$\gamma = \frac{1}{p} \cosh^{-1} \left(1 - \frac{\chi}{2} \right) \quad (6.14)$$

where

$$\chi = \left(\frac{\omega}{\omega_R} \right)^2 + \left(\frac{\omega_L}{\omega} \right)^2 - \kappa(\omega_L)^2 \quad (6.15)$$

$$\omega_R = \frac{1}{\sqrt{L_R C_R}} \text{ rad/s} \quad (6.16)$$

$$\omega_L = \frac{1}{\sqrt{L_L C_L}} \text{ rad/s} \quad (6.17)$$

$$\kappa = L_R C_L + L_L C_R \text{ (rad/s)}^2 \quad (6.18)$$

where ω_R is right hand resonance frequency and ω_L is left hand resonance fre-

quency and κ is a constant defined in Equation (6.18) using L and C shown in Figure 6.2. So the attenuation constant and phase constant are determined by the sign of χ that defines the real and imaginary part of the propagation constant (γ) given in Equation 6.14.

$$\alpha = \frac{1}{p} \cosh^{-1} \left(1 - \frac{\chi}{2} \right) \quad \text{if } \chi < 0 \quad (6.19)$$

$$\beta = \frac{1}{p} \cos^{-1} \left(1 - \frac{\chi}{2} \right) \quad \text{if } \chi > 0 \quad (6.20)$$

where α and β are real and imaginary part of γ defined in Equation (6.14). For very small sized UE for which $\beta p \ll 1$ the propagation constant can be approximated as

$$\beta = \frac{s(\omega)}{p} \sqrt{\left(\frac{\omega}{\omega_R} \right)^2 + \left(\frac{\omega_L}{\omega} \right) - \kappa \omega_L^2} \quad (6.21)$$

Where the terms ω_R , ω_L and κ are given in Equations (6.16) - (6.18) and $s(\omega)$ depends on the frequency of operation and the inductance and capacitance related to the structure as

$$s(\omega) = \begin{cases} -1, & \text{if } \omega < \min(\omega_{se}, \omega_{sh}) \quad \text{LH Range} \\ +1, & \text{if } \omega > \max(\omega_{se}, \omega_{sh}) \quad \text{RH Range} \end{cases} \quad (6.22)$$

where ω_{se} and ω_{sh} are series and shunt resonances that are defined as

$$\omega_{se} = \frac{1}{\sqrt{L'_R C'_L}} \text{ rad/s} \quad (6.23)$$

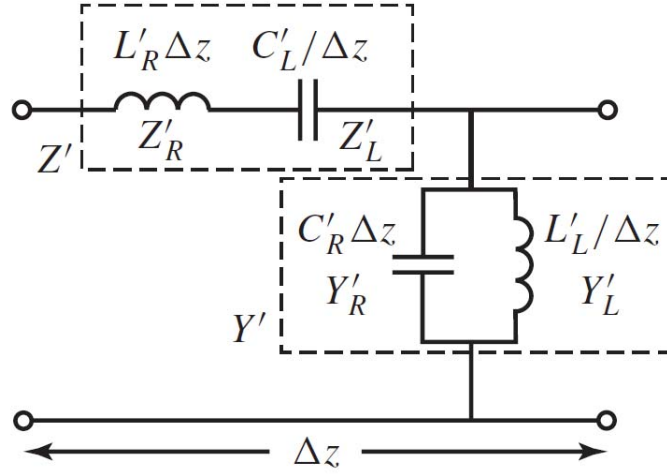


Figure 6.2: Circuit equivalent model for unit element [57]

$$\omega_{sh} = \frac{1}{\sqrt{L'_L C'_R}} \text{ rad/s} \quad (6.24)$$

where $C'_x = C_x/p$ and $L'_x = L_x/p$ are the capacitances and inductances per unit length. The inductance and capacitance locations for LH and RH sections are shown in Figure 6.2. The graphical representation of the dispersion relation depends on the inductance and capacitance of the metamaterial unit cell. A typical dispersion diagram is shown in Figure 6.3. This dispersion diagram is for an unbalanced metamaterial ($\omega_{se} \neq \omega_{sh}$) [57] that is required for isolation enhancement as it provides a bandgap.

The dispersion diagram provides the information about the phase and group velocities. Consider a point P on the dispersion diagram. The slope of a line from origin to point P gives the phase velocity (V_P) and the slope of dispersion curve at the point P provides the group velocity as shown in Figure 6.3. The group velocity and phase velocity are opposite in direction at low frequency (β_{LH} in Figure 6.3) indicating the LH behaviour in that frequency range. For high frequency, the

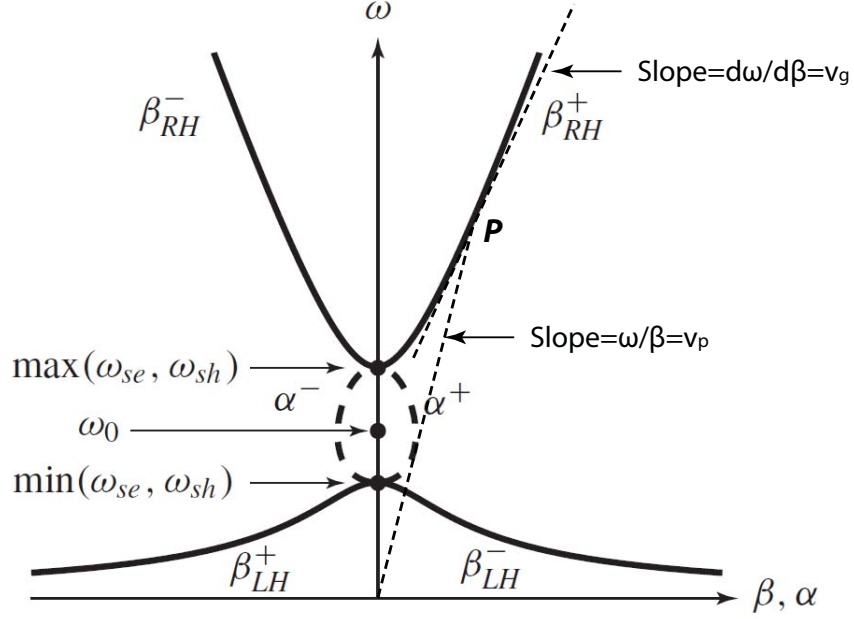


Figure 6.3: Typical dispersion diagram for unbalanced metamaterial unit element [57]

slopes have same sign. So the material is behaving as a RH material for the high frequency. Between the LH and RH behaviour, there is frequency band where only the attenuation constant exists and there is no phase constant. This is the bandgap offered by the material that will be used to suppress the coupling signal between the radiating elements in our proposed work.

Dispersion Diagram extraction for practical UE

Analytical expressions for dispersion diagram provides insight to the behaviour of the material. However it is not always possible to extract the inductance and capacitance associated with the UE of the metamaterial. Full-wave simulators are used to extract the dispersion diagram for practical structures. In case of full-wave simulation, Maxwell's equations are solved for the structure with specific

boundary conditions.

It was mentioned earlier that metamaterials are usually periodic structures where the fields and material parameters repeat after the lattice vector. Such a periodic structures can be completely characterized by the analysis of the UE that is repeated to realize the material. In order to find the possible modes supported by a unit cell, we need to solve the Eigen value problem raised by Maxwell equations. The Maxwell equations can be written as [58]

$$\begin{aligned}
\nabla \cdot H(r, t) &= 0 \\
\nabla \cdot [\varepsilon(r)E(r, t)] &= 0 \\
\nabla \times H(r, t) - \varepsilon_o \varepsilon(r) \frac{\partial E(r, t)}{\partial t} &= 0 \\
\nabla \times E(r, t) + \mu_o \frac{\partial H(r, t)}{\partial t} &= 0
\end{aligned} \tag{6.25}$$

In these equations linear dielectric medium is assumed in which relative dielectric permittivity is function of space and relative permeability is unity. If we assume time harmonic fields then the solution of these equations will be in the form of exponentials.

$$\begin{aligned}
H(r, t) &= H(r)e^{j\omega t} \\
E(r, t) &= E(r)e^{j\omega t}
\end{aligned} \tag{6.26}$$

The curl equations become

$$\begin{aligned}\nabla \times H(r, t) + jw\varepsilon_o\varepsilon(r)E(r, t) &= 0 \\ \nabla \times E(r, t) - jw\mu_oH(r, t) &= 0\end{aligned}\tag{6.27}$$

By decoupling these equations we have the equation for the magnetic field [58]

$$\nabla \times \left(\frac{1}{\varepsilon(r)} \nabla \times H(r) \right) = \left(\frac{w}{c} \right)^2 H(r) \tag{6.28}$$

This is an Eigen value problem that states that the differential operator applied on the magnetic field $H(r)$ should give a constant times the same magnetic field $H(r)$. Different modes are associated with different Eigen values of $H(r)$. w is a function of the wave vector (k). Hence the complete analysis of the modes of a UE require to take all possible non-redundant values of the wave vector and get the fields associated with that wave vector.

To take all possible non-redundant values of the wave vector, a specific region is required to be identified that defines a complete set of wave vectors. Consider the magnetic field in a periodically repetitive dielectric medium.

$$\vec{H}_k(\vec{r}) = e^{ik \cdot r} u(\vec{r} + R) \tag{6.29}$$

Here R is lattice vector and $\vec{H}_k(\vec{r})$ represents a magnetic field associated with a specific mode defined by k wave vector. Different values of k will lead to magnetic

fields of different modes. The k defines the phase component of the field as shown in the Equation (6.29). The phase is the same if it is incremented by $2\pi N$ where N is an integer. So increment in k does not always result in a new mode. A space for which k is not repeated by incrementing or decrementing the $2\pi N$ term where N is integer is known as Brillouin Zone. This type of symmetry is known as reciprocal symmetry [59].

Once the Brillouin Zone is determined (that is equivalent to a UE), Brillouin established that there exist symmetry even within the Brillouin Zone, the Brillouin Zone is further divided into multiple zones. After utilizing the rotation, reflection and inversion symmetry, a specific zone is established within the Brillouin Zone known as irreducible Brillouin Zone or first Brillouin Zone[59]. This zone contains all possible modes and modes repeat themselves in other zones within the Brillouin zone. So analyzing the UE only for the irreducible Brillouin Zone will give all possible modes supported by the UE. The Brillouin zone and irreducible Brillouin zone are shown in Figure 6.4 for a general periodic structure. The Brillouin zone and the irreducible Brillouin zone for the CLL used to define the isolation structure metamaterial is shown in Figure 6.5. The M, X and Γ conventionally represent the vertices for irreducible Brillouin zone, k is wave vector and vector r is an arbitrary vector.

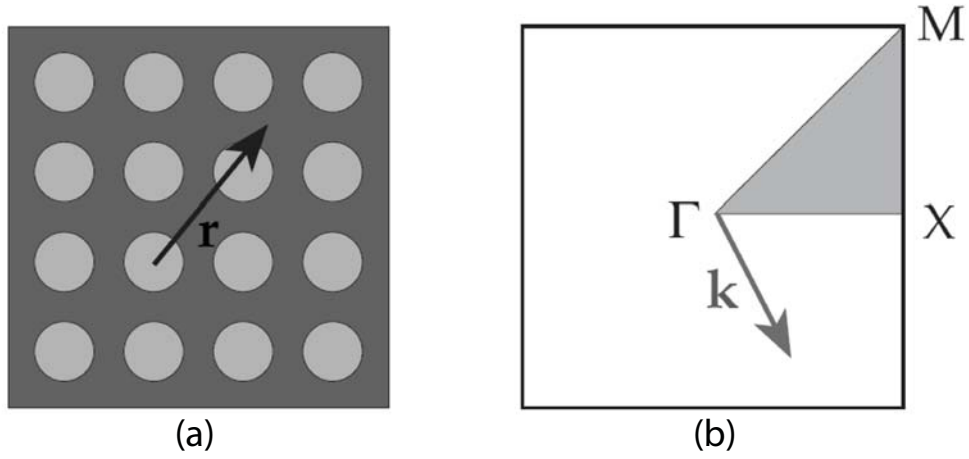


Figure 6.4: Brillouin Zone (a) and irreducible (first) brillouin zone (b)

6.2.4 Parametric Analysis of the Proposed UE

In the CLL unit cell of this metamaterial, shown in Figure 6.5, the spacing between the spirals (Gap), the dimensions of the unit cell (UL and UW) and the number of edges in the spirals of the unit cell are the controlling factors to tune the frequency response of the UE. In this subsection we investigate the effects of these parameters on the dispersion diagram and this is used to identify the resulting bandgap.

Increasing the spacing between the spirals raises the resonance frequency. The resonant frequency is inversely proportional to the capacitance of the structure. The capacitance depends on the spacing between the spirals. Increasing the spacing lowers the capacitance and increases the resonance frequency. This can be observed in the curves in Figure 6.6. These dispersion diagram curves are generated for the unit cell of size $9mm \times 4.5mm$, the dimensions of one square CLL is $4.4mm$, the distance between the two square CLLs is $0.1mm$, the number of spiral

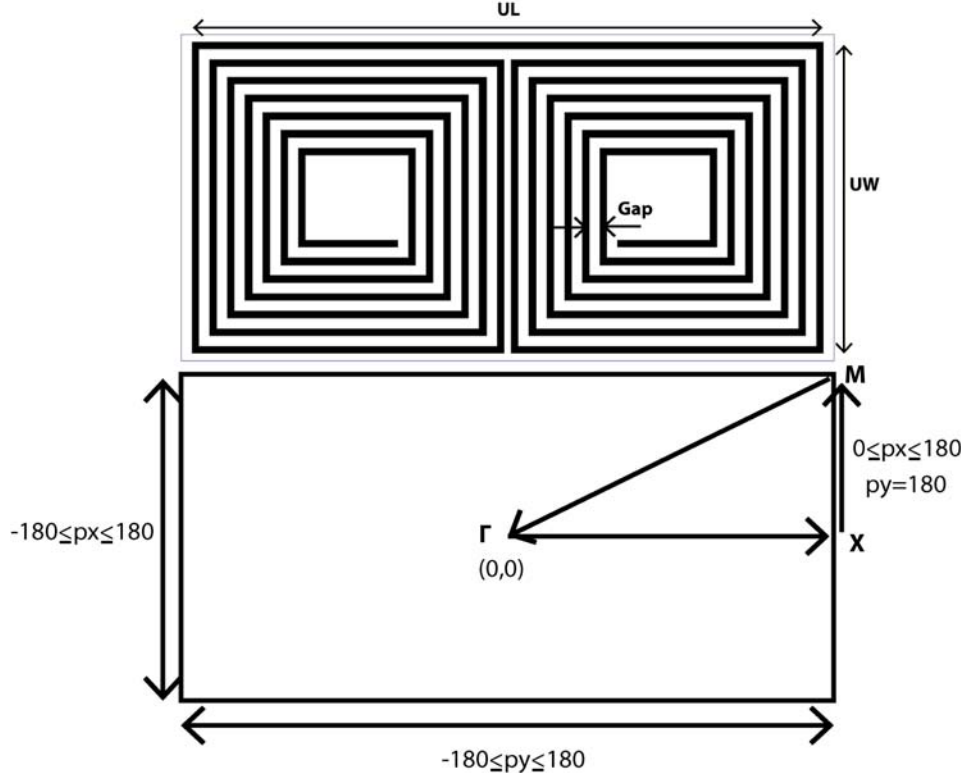


Figure 6.5: UE (top) and Brillouin Zone and irreducible Brillouin Zone (bottom) for metamaterial

edges is 27 and the spacing is varied between the metallic traces of the unit cell. Increasing the structure size reduces the resonance frequency. By increasing the structure size, the coupling length of the spiral edges increases. This will increase the associated L and C and lowers the frequency as the resonance frequency is inversely proportional to the square root of the L times C . Figure 6.7 shows the effect of changing the size of the structures. The response in Figure 6.7 is for the CLL unit cell with 0.15mm spacing between the spiral traces and the number of edges is 27. Increasing the number of spiral edges with constant structure size lowers the resonating frequency. Increasing the spiral edges increases the coupling length between the spiral arms. As the number of spiral edges increases, the size

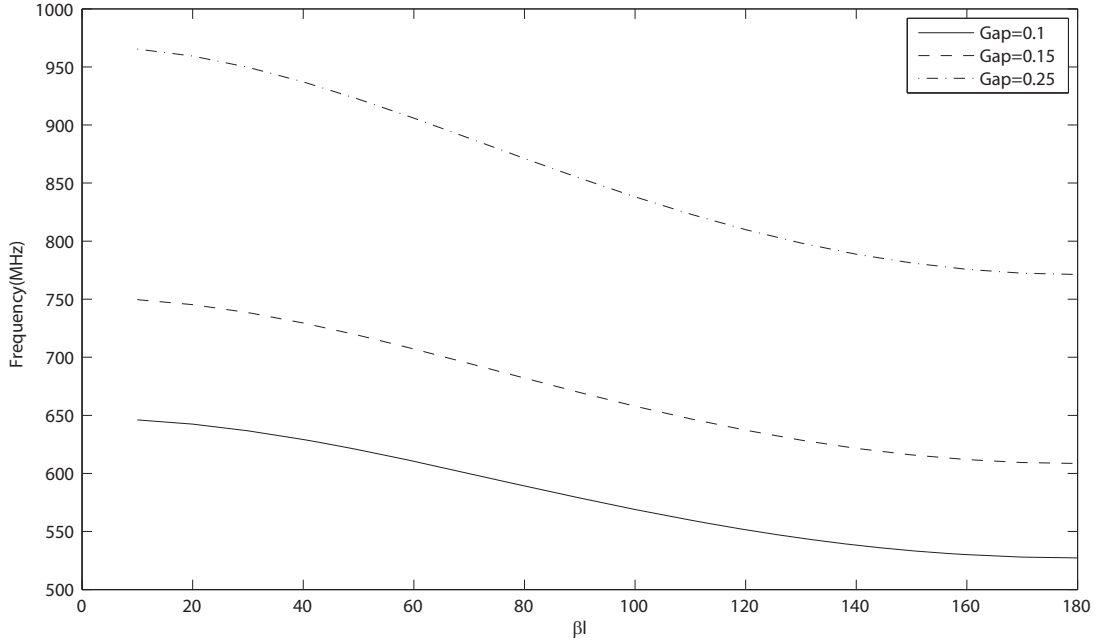


Figure 6.6: Effect of spacing on the fundamental mode; $UL=9, UW=4.5$, $edges=27$ of the edge is reduced due to circular nature of the structure. This reduced size adds less coupling between spirals. Therefore the effect of adding spiral edges reduces as the number of edges is increased. Figure 6.8 illustrates the effect of the additional spiral edges on the band-gap.

6.2.5 Test Setup for the Proposed Structure

In order to test the material, a test setup was developed as devised in [54]. This setup consists of an array of the unit cells of the metamaterial (gray) on the top layer of the substrate. The complementary metamaterial (black) is etched out from the ground plane (white). To transfer energy across the metamaterial, another thin ($0.07mm$) layer of substrate is placed on the metamaterial and a TL (gray) is placed on this thin layer as shown in Figure 6.9. Ports are defined on

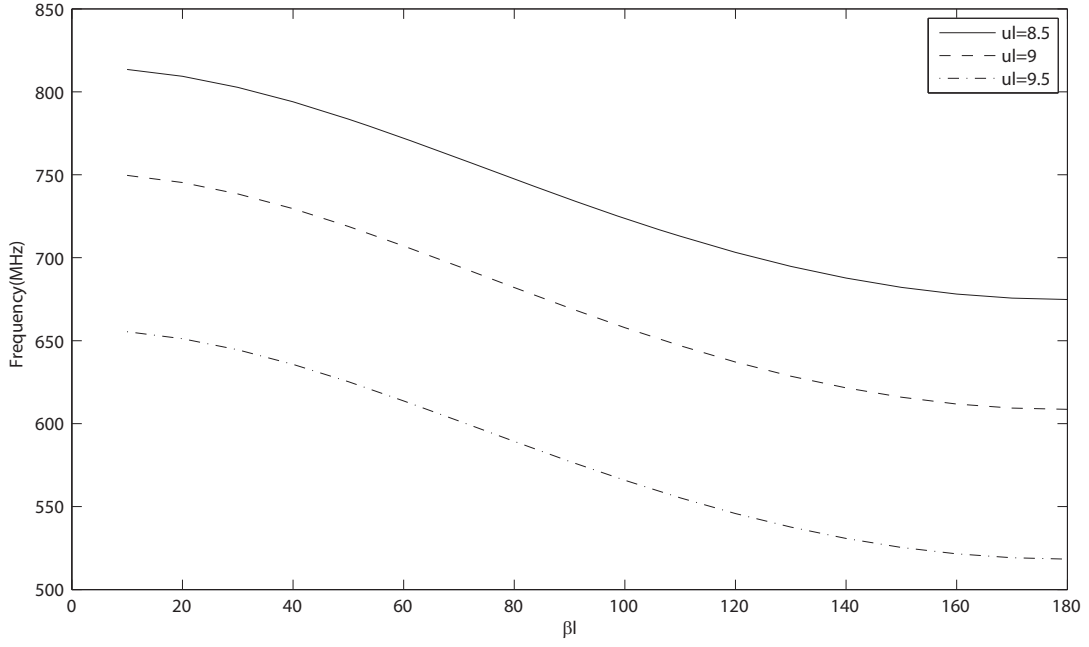


Figure 6.7: Effect of structure size on the first mode; spacing= $0.15mm$; spiral edges=27

both edges of the TL.

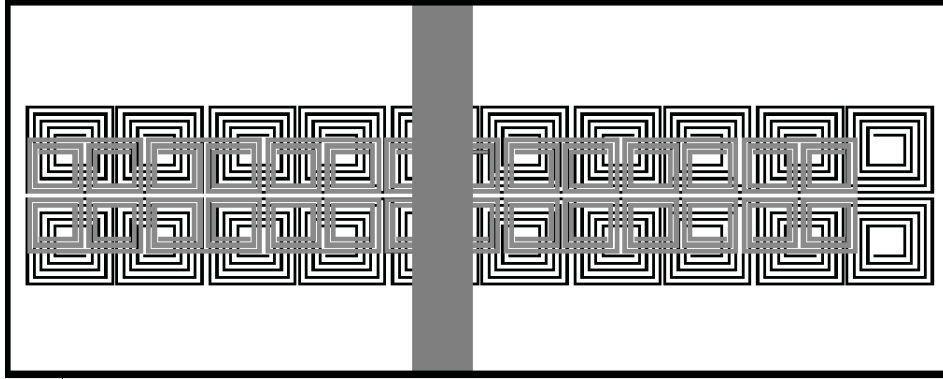


Figure 6.9: Test setup for metamaterial.

The transmission coefficient is shown in Figure 6.10. Here we can see a dip in $|S_{21}|$ at $0.76GHz$ and $2GHz$ which are the approximate frequencies at which the isolation is required. There is another dip at $2.5GHz$ that can be the result of

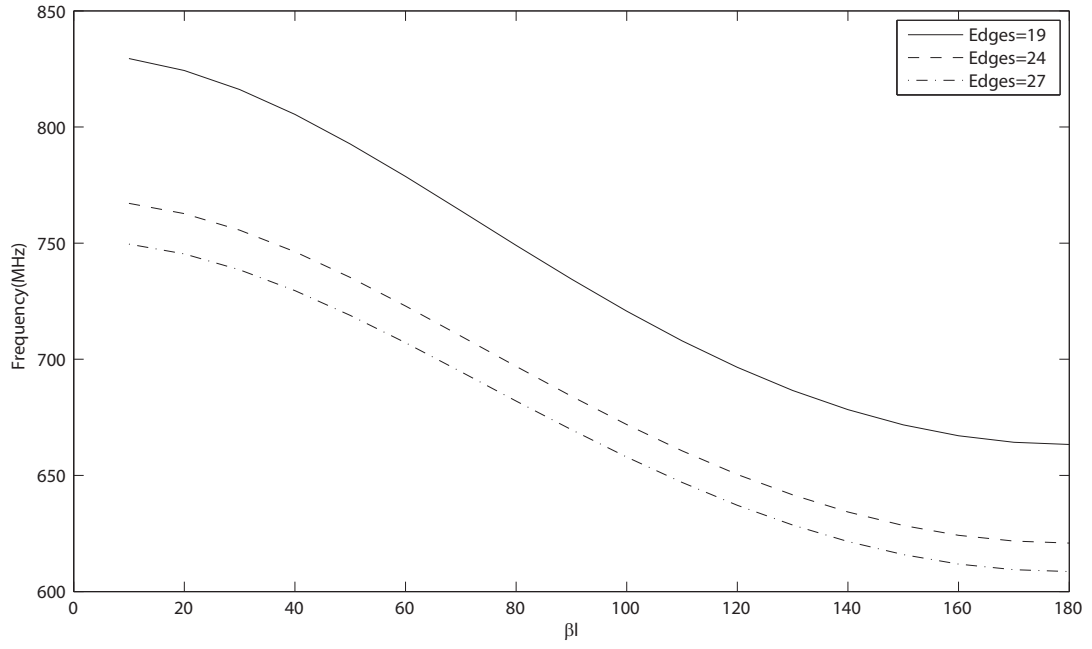


Figure 6.8: Effect of spiral edges on the fundamental mode; $UL=9mm$; $Gap=0.15mm$

higher order modes generated by the metamaterial. Two rows of this metamaterial are placed between the antennas to get the required isolation.

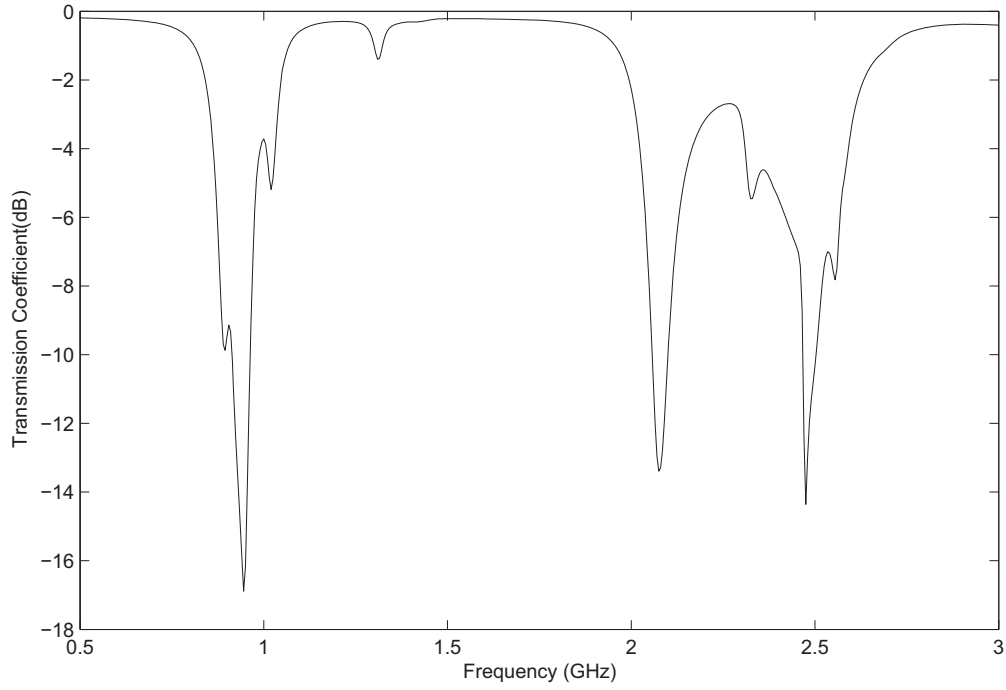


Figure 6.10: Transmission coefficient of the test setup.

The dispersion diagram of the designed structure is shown in Figure 6.11. This dispersion diagram shows that there is a frequency bandgap between two modes in which wave propagation is not supported by the material. Figure 6.11(a) is for the high band. This diagram states that waves with frequency ranges between $1.4 - 1.75 GHz$ are supported by the first mode and the second mode supports the frequency range of $2.22 - 2.5 GHz$. Both bands show Left Hand (LH) behavior as the slope of the curves is negative. The fundamental mode is studied in [60] showing that it is predominately TE mode in desired direction of propagation. The Figure 6.11(b) shows the dispersion diagram for the low band. It is clear that there is a bandgap between $750 - 842 MHz$.

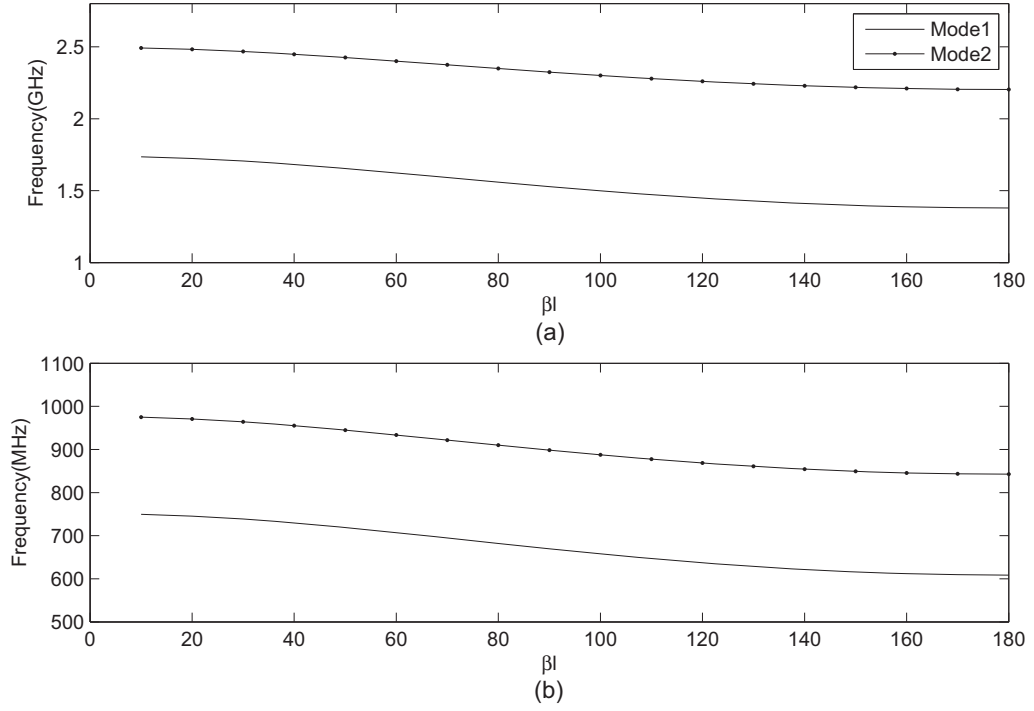


Figure 6.11: Dispersion diagrams for the proposed structures (a) High band (b) Low band

6.2.6 MIMO Antenna System with Metamaterial based Isolation Enhancement Structure

The antenna model with the metamaterial is shown in Figure 6.12. The antenna dimensions are (in mm): $W=50$, $L=100$, $W_t=2.2$, $H=6.9635$, $L_1=35.3$, $L_2=26$, $Y_s=5.5$, $X_{a2}=4.0716$, $L_f=14.7$, $X_s=0.3716$, $X_f=1.5716$, $W_f=2.5$, $W_s=1$, $W_{tr}=1.4$, $W_{50}=3$, $Y_{f1}=13.35$, $Y_{f2}=13.5$, $Y_{f3}=28.65$, $UE_W1=5.727$, $UE_L1=5.8$, $L_3=35.8$, $W_1=12.2$, $UE_W=9$, $UE_L=8.927$, $Y_1=64.127$, $Y=44$, $W_2=15.9$, $Y_{dist}=0.273$, $Gap=0.127$, $X_{dist}=0.2$, $W_{trace}=0.25$, $Y_{dist1}=0.2$, $X_{dist1}=0.127$, $GAP1=0.36$ and $W_{trace1}=0.2$. The fabricated model is shown in Figure 6.13. This model is denoted as Model_D from now onwards.

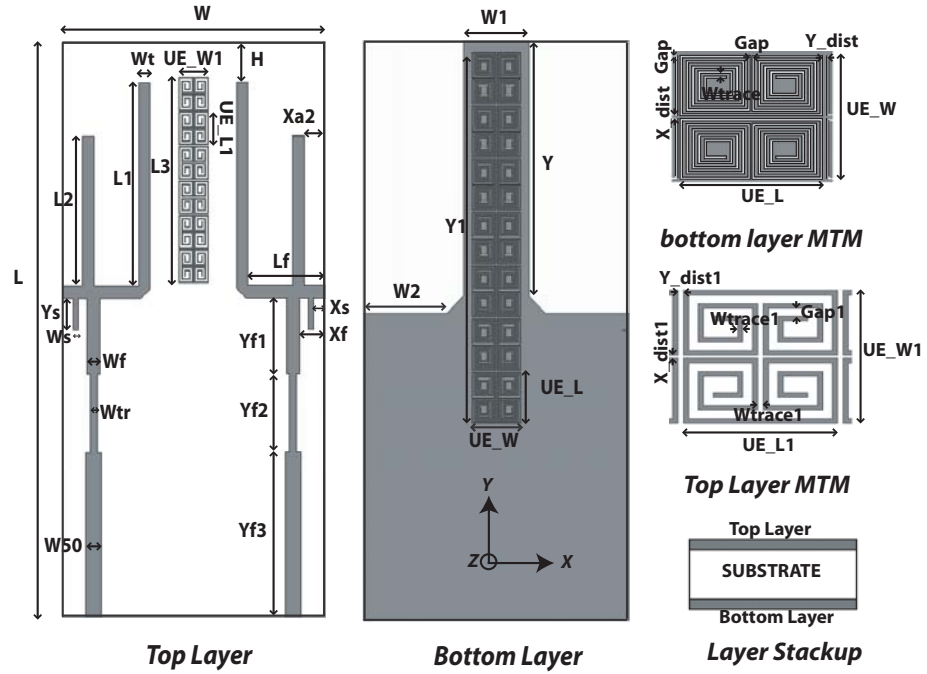


Figure 6.12: Simulation model for Model_D

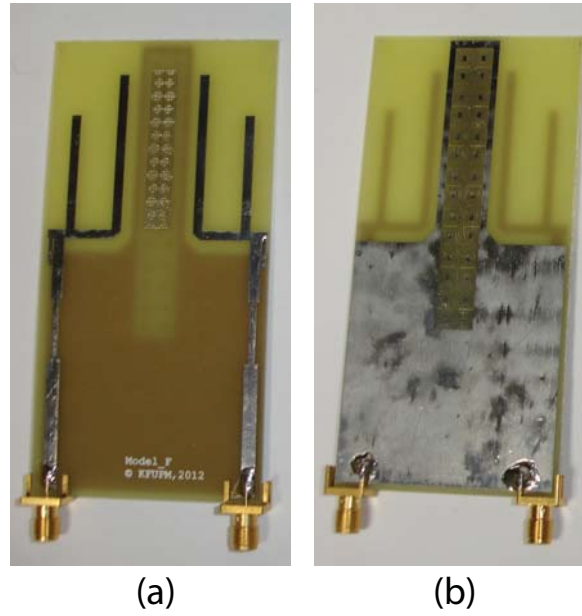


Figure 6.13: Fabricated prototype for Model_D, (a) Top side (b) Bottom side.

The prototype is practically fabricated and experimental data is presented in this section except the radiation efficiency that is determined using simulator due

to lack of resources to accurately measure the radiation efficiency. Measured S-parameters are shown in Figures 6.14 and 6.15 for the low-band and high-band, respectively. The low-band covered the $827 - 853\text{MHz}$ and $831 - 856\text{MHz}$ frequency range for element1 and element2, respectively. The minimum -6dB bandwidth was 25MHz . The high band covered the $2.3 - 2.98\text{GHz}$ frequency range. The -6dB bandwidth was more that 640MHz . The minimum isolation in the low band is 18.9dB and 9.8dB for the low-band and high-band, respectively.

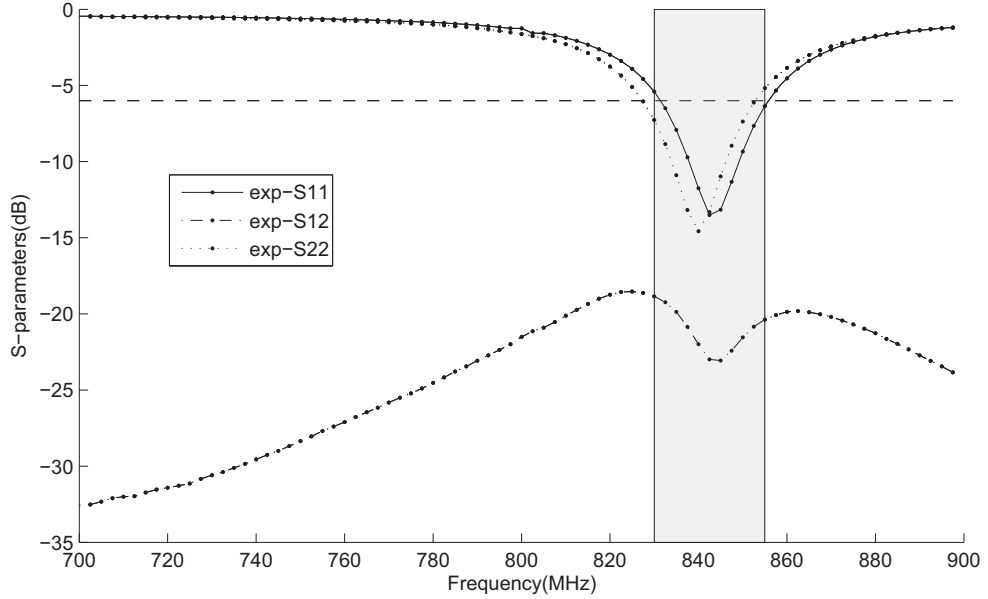


Figure 6.14: Low band S-parameters for Model_D.

The TARC figures are shown in Figures 6.16 and 6.17. These curves were calculated using Equation (2.11). The low-band TARC is stable for the change in the input phase whereas the center resonance frequency shifts for the high-band by changing the input phase.

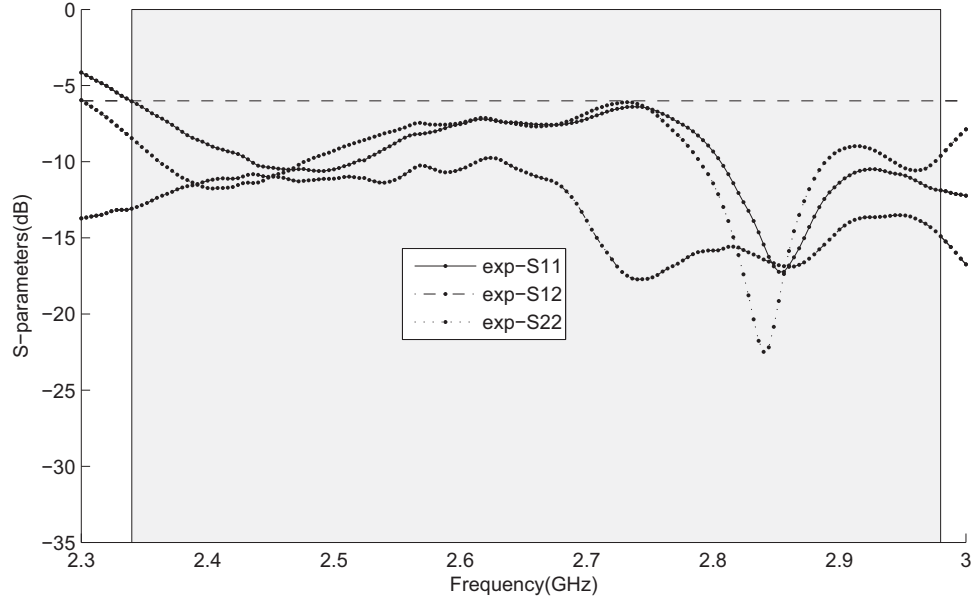


Figure 6.15: High band S-parameters for Model_D.

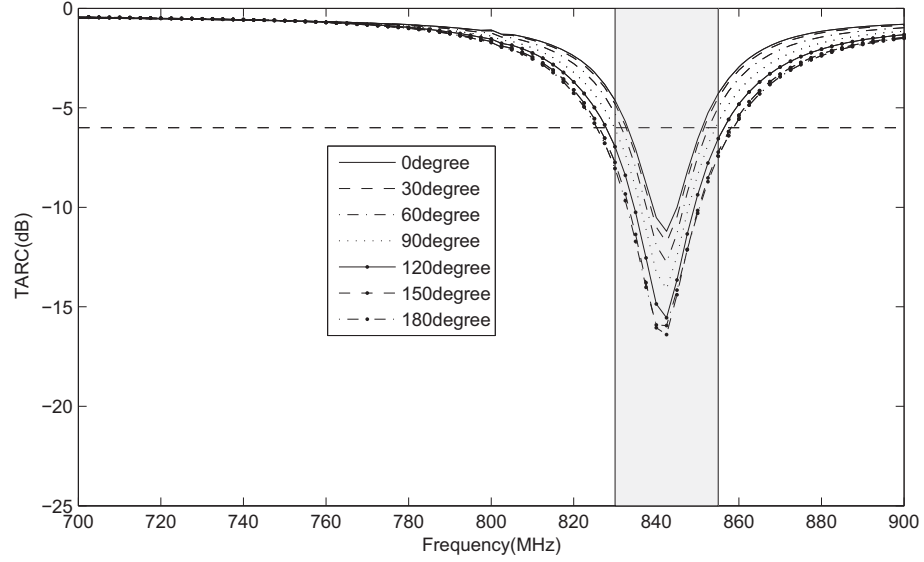


Figure 6.16: Low band TARC for Model_D.

The correlation coefficient curves are also shown in Figures 6.18 and 6.19 for both bands. Both curves conform that the correlation coefficient is below 0.3 threshold

set for the MIMO antenna systems. Equation (2.2) is used to calculate these curves. The curves were created based on the radiation efficiency values of 35% and 67% for the low and high bands, respectively.

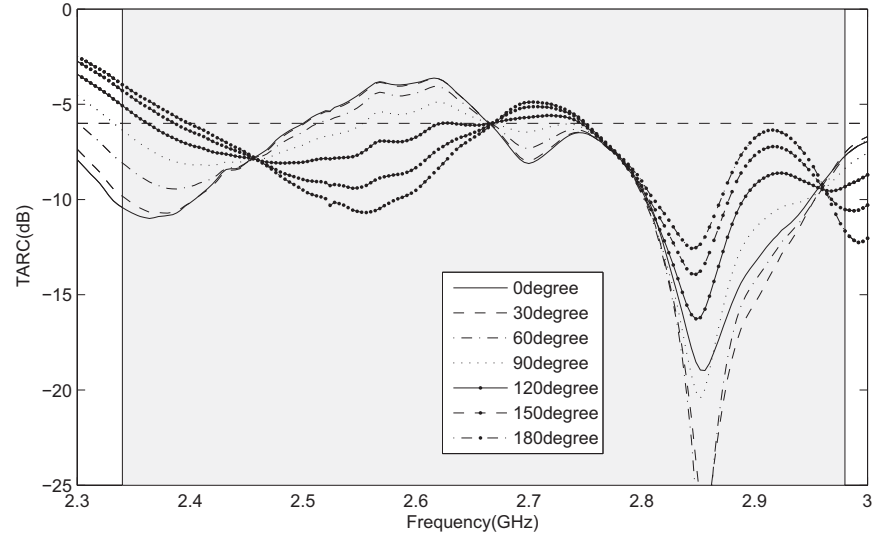


Figure 6.17: High band TARC for Model_D.

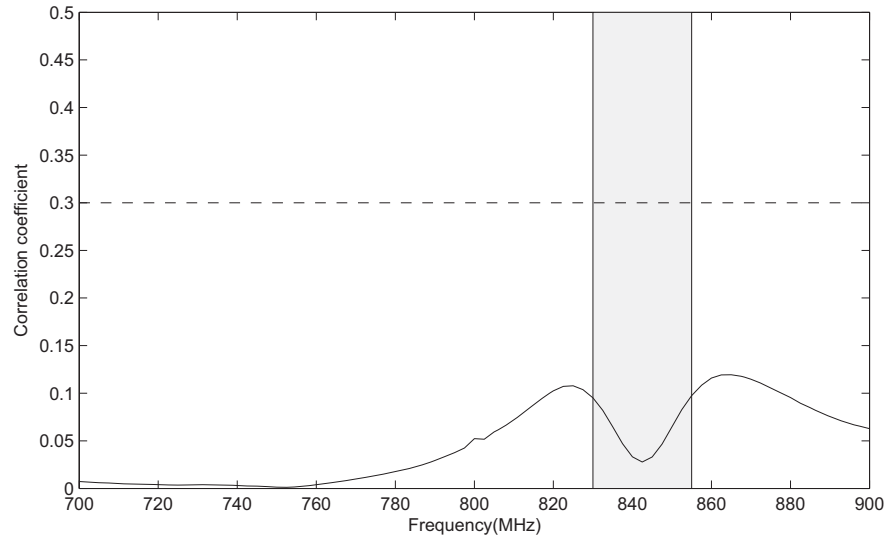


Figure 6.18: Low band Correlation coefficient for Model_D.

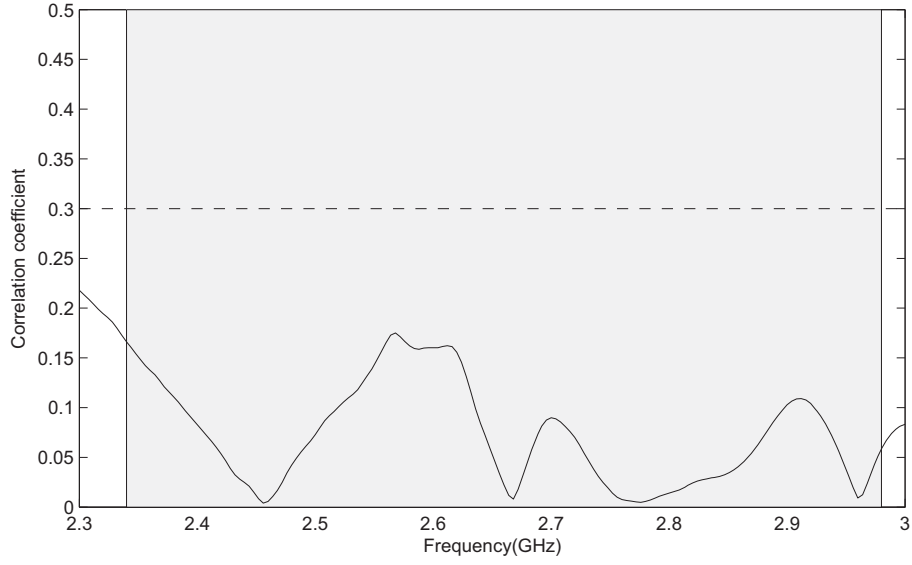


Figure 6.19: High band Correlation coefficient for Model_D.

The current distribution of Model_B is shown in Figures 6.20 and 6.21 at $820MHz$ and $2.65GHz$. In comparison with the current distribution of Model_A, significant difference can be observed. For low band, the current distribution is almost identical for both 4-shaped radiators in case of Model_A (Figure 4.9) where as in Figure 6.20, the current distribution on the terminated radiator is much less (darker) as compared to the current distribution on the excited radiator. This reduction in current on the terminated radiator has improved the isolation. Same argument also applies to high band current distribution comparison of Model_A (Figure 4.10) and Model_D (Figure 6.21).

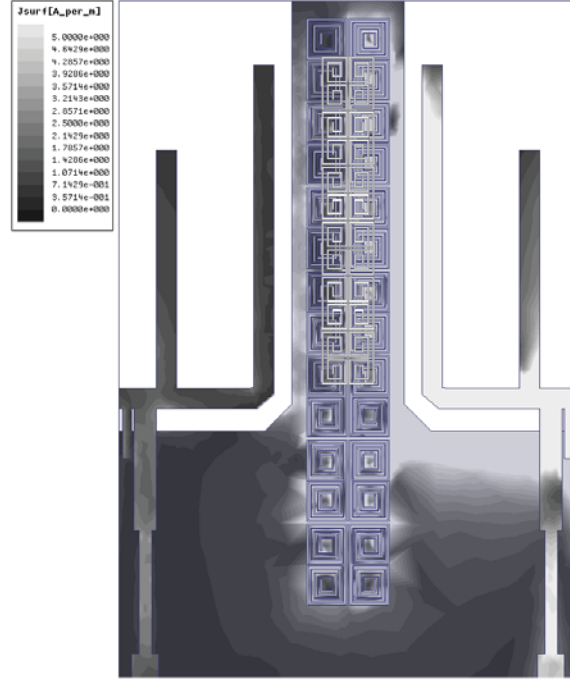


Figure 6.20: Current distribution for Model_D at $840MHz$.

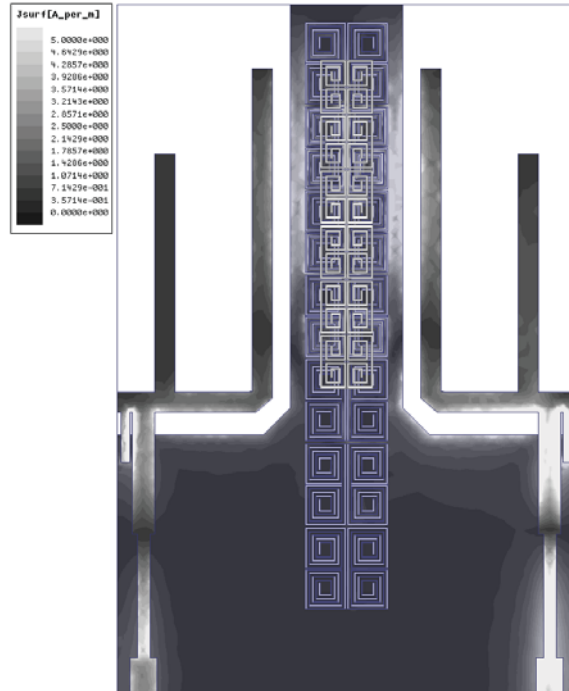


Figure 6.21: Current distribution for Model_D at $2.85GHz$.

The 2D cuts of the measured gain pattern are shown in Figure 6.22. The maximum measured gain was -2.8dBi and 6.7dBi for the low band and high band respectively. Figures 6.22(a) and 6.22(b) show the principle plane cuts of the measured gain patterns for Element 1 and 2 for co-polarization (gain theta) and cross polarization (gain phi) at 840MHz . Similarly Figures 6.22(c) and 6.22(d) show the principle plane cuts of the measured gain patterns for Element 1 and 2 for co-polarization and cross polarization at 2.85GHz . The measurements were conducted at an outdoor antenna range facility at Oakland University, Michigan, USA.

MEG values are calculated according to Equation (2.8) using simulated gain patterns. The calculated MEG for Model_D for the low band with cross-polarization discrimination (Γ) of 0dB were $MEG1_{LOW} = -2.304\text{dB}$ and $MEG2_{LOW} = -2.33\text{dB}$, for elements 1 and 2, respectively. For the high band, the values were $MEG1_{HIGH} = -7.9038\text{dB}$ and $MEG2_{HIGH} = -7.9\text{dB}$, for elements 1 and 2, respectively. With a Γ value of 6dB , the values were $MEG1_{LOW} = -2.29\text{dB}$, $MEG2_{LOW} = -2.31\text{dB}$, $MEG1_{HIGH} = -7.92\text{dB}$ and $MEG2_{HIGH} = -7.935\text{dB}$, for the low and high bands of elements 1 and 2. As mentioned in Section 2.3 that the value of MEG is dependent on the incident wave angle (θ_1) that is taken as 0° in this work. The gain patterns of Model_D show that gain value is very low at $\theta = 0^\circ$ for high band. The low gain value of gain at the incident angle resulted a low MEG_{HIGH} value. It is evident that the ratio of $MEG1/MEG2 < 3\text{dB}$ at both bands of operation with both Γ values that pro-

vides acceptable diversity gain. Model_D performance parameters are summarized in Table 6.1.

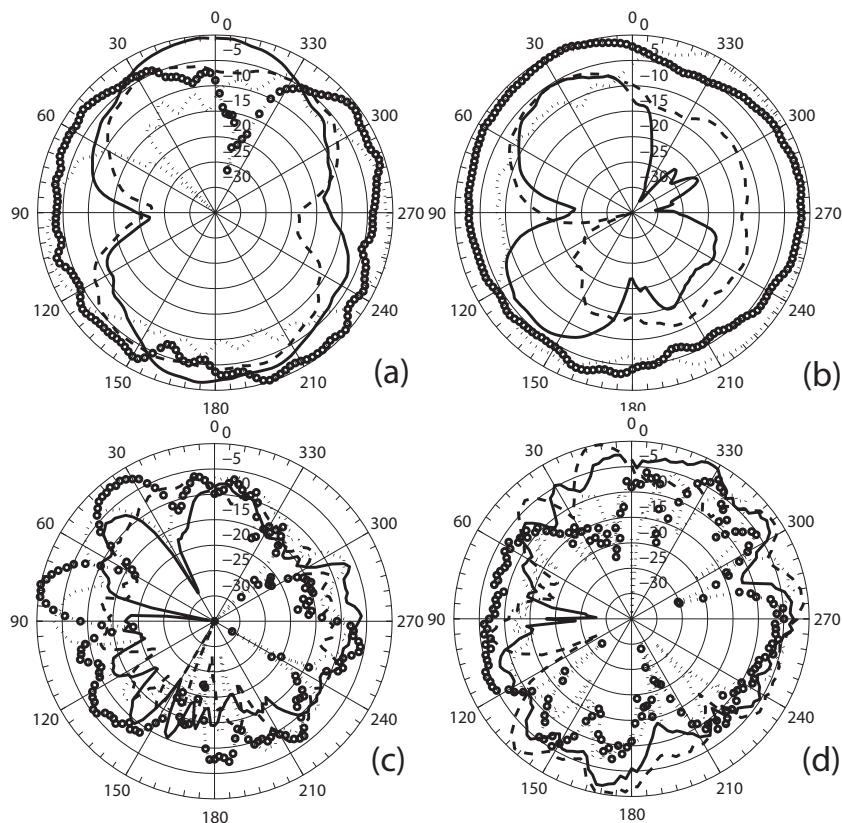


Figure 6.22: Measured gain patterns for Model_D. Dots:vertical polarization for element 1, Circles:vertical polarization for element 2, Solid:horizontal element 1, Dashes:horizontal polarization element 2.

6.3 Magnetic Wall based Isolation Enhancement structure

A metamaterial based novel isolation technique was proposed in [43]. The authors named the proposed isolation structure a channel isolator. The channel isolator

Table 6.1: Summary for Model_D performance parameters

Parameters	Low-Band	High-Band
Bandwidth (-6dB)	827-853MHz	2.3-2.98GHz
Maximum Gain	-2.8dBi	6.7dBi
Minimum isolation	18.9dB	9.8dB
Efficiency(η)	35%	67%
Correlation Coefficient	0.11	0.18
MEG1($\Gamma = 0$)	-2.304dB	-7.9038dB
MEG1($\Gamma = 6dB$)	-2.29dB	-7.92dB
MEG2($\Gamma = 0$)	-2.33dB	-7.9dB
MEG2($\Gamma = 6dB$)	-2.31dB	-7.935dB

suppresses the coupling surface currents within the dielectric layer. This type of structure provides a magnetic wall between the radiators. This magnetic wall does not allow magnetic fields to be coupled between the radiators and hence improve the isolation.

6.3.1 UE for Magnetic Wall

The UE proposed in [43] is shown in Figure 6.23. This UE consists of an interdigital capacitor connected to the ground plane through vias. The surface waves that are targeted to be suppressed using an array of this UE, exist in TM mode with zero cutoff frequency. This means that these surface waves exists at all frequencies. The orientation of the UE should be such that these waves pass through the UE. As they pass through the UE, these waves create currents on the vias of the UE. This current excites the UE and if the UE is designed to resonate at a desired frequency, the UE cancels the incident magnetic field by generating a magnetic field that is opposite in direction to the applied field. This cancellation property of the array of these UE allows the channel isolator to act as a magnetic

wall within the antenna structure.

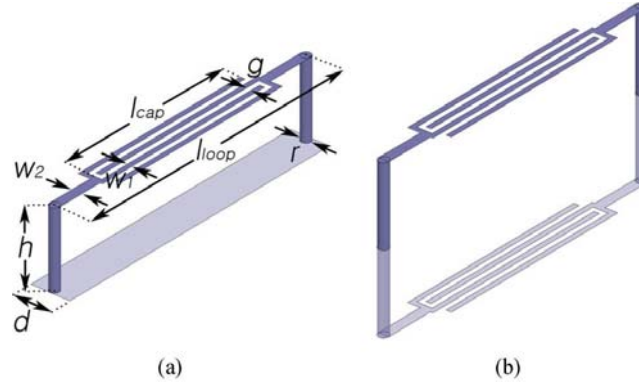


Figure 6.23: UE for the magnetic wall[43].

However there are certain limitations associated with this UE. The UE covers a large area when designed for low frequency. The frequency at which the array of UE acts as a magnetic wall depends on the resonance frequency of the UE. The resonance frequency is related to the UE inductance and capacitance through following formula

$$f_r = \frac{1}{4\pi\sqrt{LC}} \quad (6.30)$$

where f_r is resonance frequency and L and C are inductance and capacitance of the UE structure

To reduce the resonance frequency, the inductance and capacitance have to be increased. The Capacitance can be increased by either increasing the length of interdigital capacitor fingers or by reducing the gap between them. The first option increases the size and the other option is limited by the fabrication process. Similarly inductance can be increased either by increasing the overall length of the UE or placing them closer (increase coupling between the adjacent UEs). Again

the first option leads to larger sized UEs and the second option is limited by fabrication process.

In addition, the channel isolator is effective only for limited types of antennas. As mentioned earlier, a magnetic field passing through the UE is required to excite the UE. Hence such type of isolation structures are useful on antenna systems where the magnetic field is a major cause of high coupling between the radiating elements, such as the case with spiral antennas.

6.3.2 MIMO Antenna System with Magnetic Wall

Model_A with magnetic wall is shown in Figure 6.24. The dimensions of this model are (in mm): $W = 50$, $L = 100$, $W_t = 2.2$, $H = 2.5493$, $L_1 = 40.75$, $L_2 = 27$, $Y_s = 5.5$, $X_{a2} = 1.6716$, $L_f = 15.8$, $X_s = 0.6716$, $X_f = 2.6716$, $W_f = 2.5$, $W_s = 1$, $Y_f = 15.5$, $W_1 = 10$, $Y = 46$, $W_2 = 17$. The dimensions for UE shown in Figure 6.23 are (in mm): $h=1.56$, $d=0.81$, $r=0.1$, $W_2=0.2$, $W_1=0.1$, $g=0.1$, $l_{loop} = 6.25$, $l_{cap} = 5.45$. This model is denoted as Model_E.

6.3.3 Results and Discussion

The simulated S-parameters for Model_E are shown in Figures 6.25 and 6.26. According to these figures, there is no improvement in isolation. This is due to the fact that this isolation enhancement mechanism does not match with radiation mechanism of the 4-shaped MIMO antenna system.

The magnetic wall is effective only when the magnetic field is the coupling signal between the radiating elements. The magnetic field distribution for 4-shaped MIMO antenna system is shown in Figure 6.27 for better understanding of the field distribution.

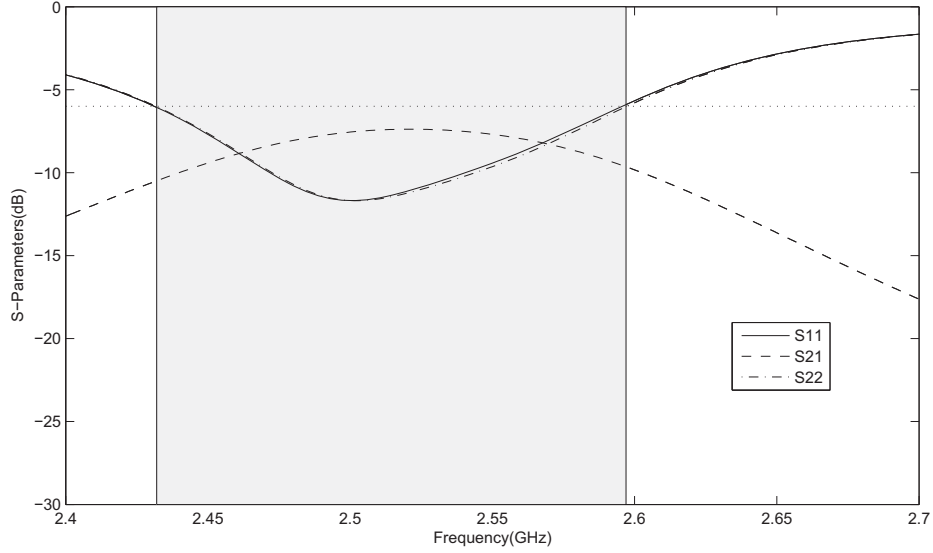


Figure 6.26: High band S-parameters for Model_E.

According to Figure 6.27, there is no magnetic field between the radiators at the higher resonance to excite the channel isolator. Hence the channel isolator is not effective in the case of 4-shaped MIMO antenna system. Thus this method is not investigated further.

The antenna parameters were extracted from the simulation model. The minimum isolation level was 6.6 and 7.4 dB for the low and high band. The range of the low band was 772 to 798 MHz providing -6 dB bandwidth of 26 MHz. For the high band, the range was 2.43 to 2.596 GHz with -6 dB bandwidth of approximately 166 MHz. The maximum correlation coefficient values, calculated using

Equation (2.2), were 0.32 and 0.35 for the low and high bands. The simulated maximum gain was $-0.8dBi$ and $4.57dBi$ for the low and high bands, respectively. Maximum simulated radiation efficiency was 40% and 70% for low and high bands, respectively.

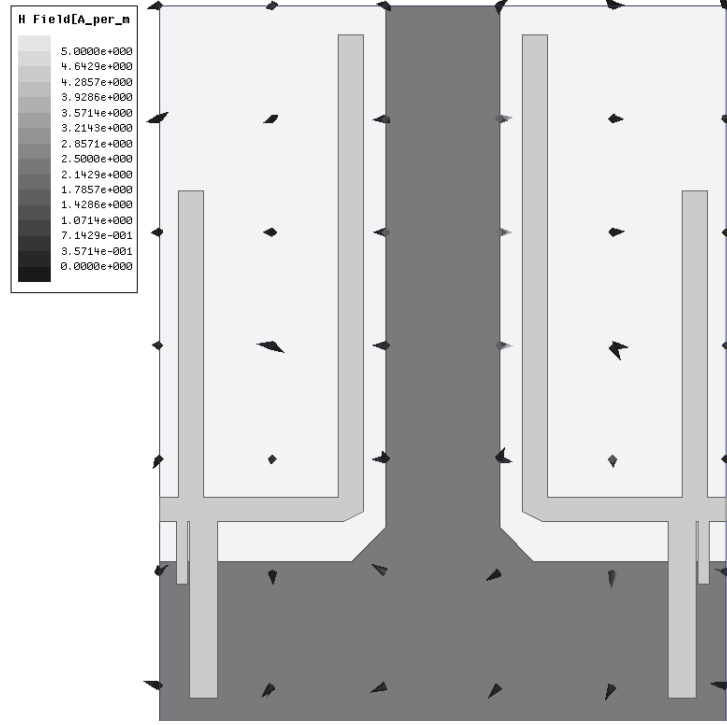


Figure 6.27: Magnetic field distribution between 4-shaped radiators at 2.54GHz.

MEG values were calculated according to Equation (2.8) using simulated gain patterns. The calculated MEG for Model_E for the low band with cross-polarization discrimination (Γ) of $0dB$ were $MEG1_{LOW} = -1.544dB$ and $MEG2_{LOW} = -1.476dB$, for elements 1 and 2, respectively. For the high band, the values were $MEG1_{HIGH} = -1.01dB$ and $MEG2_{HIGH} = -0.85dB$, for elements 1 and 2, respectively. With a Γ value of $6dB$, the values were $MEG1_{LOW} = -1.53dB$, $MEG2_{LOW} = -1.465dB$, $MEG1_{HIGH} = -1.024dB$ and $MEG2_{HIGH}$

$= -0.86\text{dB}$, for the low and high bands of elements 1 and 2. The performance parameters for Model_E are listed in Table 6.2.

Table 6.2: Summary for Model_E performance parameters

Parameters	Low-Band	High-Band
Bandwidth(-6dB)	772-798MHz	2.43-2.596GHz
Maximum Gain	-0.8dBi	4.57dBi
Minimum isolation	6.6dB	7.4dB
Efficiency(η)	40%	70%
Correlation Coefficient	0.32	0.35
MEG1($\Gamma = 0$)	-1.544dB	-1.01dB
MEG1($\Gamma = 6\text{dB}$)	-1.53dB	-1.024dB
MEG2($\Gamma = 0$)	-1.476dB	-0.85dB
MEG2($\Gamma = 6\text{dB}$)	-1.465dB	-0.86dB

6.4 Comparison between the proposed isolation methods

Table 6.3 shows complete comparison between the reference MIMO antenna and four isolation enhancement models. All MIMO antenna performance metrics are summarized in a single table for ease of comparison.

This table shows that the bandwidth is reduced for MIMO antenna systems with effective isolation enhancement structures (DGS and CLL based metamaterial). The bandwidth is reduced by approximately 10MHz and 5MHz for Model_B and Model_D, respectively. The bandwidth of these models at high band is very high. It is due to the application of the impedance transformer, introduced in the structure to improve the impedance matching of the antenna and the feed point. The antenna radiation pattern changed by applying the isolation enhance-

ment structures. But since these antennas are designed for use in multipath environment, the introduction of nulls in the radiation pattern is not considered an issue. The dual-band isolation is highest for Model_D followed by Model_B. Model_C exhibited high isolation only for high band whereas Model_E did not show any improvement in the isolation. Efficiency was minimum for Model_D due to its design complexity. This model consists of two arrays of CLLs on both sides of the substrate. Energy is required to excite these complex structures. As this energy is consumed within the structure, the efficiency of this model is low as compared to the other models. However it is within the acceptable ranges. As Model_D has maximum isolation for both bands, the correlation coefficient is also minimum for this model. The correlation coefficient values are high for the antenna models that exhibit low isolation levels.

As mentioned earlier, the MEG values are strong functions of the angle θ_1 that is taken as 0° in this work. Equation (2.8) with incident angle perpendicular to the plane of the printed antenna is widely used in the research community to calculate the MEG values. In this work, MEG values are calculated using the simulated data as the experimental 3D radiation patterns are not available due to lack of resources. Only 2D measured radiation patterns were obtained in collaboration with Oakland University, USA. In simulation, the antenna structure lied in the xy-plane and $\theta = 0^\circ$ is the angle that is perpendicular to the plane of the antenna structure. For the high band, Model_D had a very low gain in the direction perpendicular to the plane of antenna structure. So its MEG values

are very low as compared to the other models. Similarly a maxima is located in direction $\theta = 0^\circ$ for Model_C. This is the reason of high MEG values for this model.

Table 6.3: Antenna parameters comparison

Parameters		Model_A	Model_B	Model_C	Model_D	Model_E
Bandwidth (-6dB)	Low band (MHz)	762-792	805-825	760-795	827-853	772-798
	High band (GHz)	2.465-2.615	2.45-2.98	2.47-2.6	2.3-2.98	2.43-2.596
Maximum Gain	Low band (dBi)	-4	-4	-0.3	-2.8	-0.8
	High band (dBi)	0	2.4	4	6.7	4.57
Minimum Isolation	Low band (dB)	9.5	17	4.45	18.9	6.6
	High band (dB)	7.1	9	11.2	9.8	7.4
Efficiency η	Low band (%)	40	40	37	35	40
	High band (%)	75	67	68	67	70
Correlation Coefficient	Low band	0.35	0.15	0.27	0.11	0.32
	High band	0.15	0.23	0.23	0.18	0.35
MEG1 ($\Gamma = 0dB$)	Low band (dB)	-1.511	-1.24	-1.86	-2.304	-1.544
	High band (dB)	-1.7937	-1.27	0.8543	-7.9083	-1.01
MEG1 ($\Gamma = 6dB$)	Low band (dB)	-1.496	-1.233	-1.8474	-2.29	-1.53
	High band (dB)	-1.804	-1.279	0.8394	-7.92	-1.024
MEG2 ($\Gamma = 0dB$)	Low band (dB)	-1.53	-1.265	-1.886	-2.33	-1.476
	High band (dB)	-1.585	-1.1848	0.7891	-7.9	-0.85
MEG2 ($\Gamma = 6dB$)	Low band (dB)	-1.516	-1.258	-1.874	-2.31	-1.465
	High band (dB)	-1.5973	-1.1933	0.7742	-7.935	-0.86

6.5 Summary

This chapter presents two metamaterial based isolation enhancement techniques. The first technique involves the realization of an unbalanced metamaterial between the radiating elements using Capacitively Loaded Loops (CLLs) as its unit element. The dispersion diagram is used to characterize the the metamaterial. Parametric analysis of the proposed metamaterial is used to illustrate the behaviour of the material with the variation of the dimensions of the unit cell. The transmission coefficient for the metamaterial is also presented in this chapter. Loading Model_A with the designed metamaterial resulted in approximately $9dB$ and $2dB$ minimum isolation improvement for low and high bands, respectively. The efficiency for Model_D is reduced by at least 5% due to complex isolation enhancement structure. The bandwidth is also reduced by $5MHz$ in the low band. For the high band, increase in the bandwidth is observed due to the use of the impedance transformer applied at the feed of the 4-shaped antenna. Current distributions for Model_D (Model_A with metamaterial) are also presented in this chapter to provide a comparison with the current distributions of Model_A.

The second technique involves the realization of a magnetic wall between the radiators using a metamaterial. Model_A with a magnetic wall is denoted as Model_E. The unit element of the metamaterial and magnetic field distribution are also included in this chapter. This model provides minimum isolation of $4.57dB$ and $6.6dB$ for low and high bands, respectively. The radiation efficiency and bandwidth for both bands are approximately the same as Model_A. Hence this

isolation enhancement technique did not prove efficient for the 4-shaped MIMO antenna system. At the end of the chapter, a comparison table is presented to summarize the characteristics of all five antenna models presented in Chapters 4, 5 and 6.

CHAPTER 7

CONCLUSIONS AND FUTURE WORK

MIMO technology utilizes multiple channels in the multi-path environment, between the transmitter and receiver to increase the data rate and reliability of the received signals. Hence, the presence of multiple channels is one of the basic requirements for an efficient MIMO system. For wireless systems, multiple channels are established using multiple radiating elements in the transmitter and receiver antenna systems. Data transmitted by one radiator is received by possibly all the radiators in the receiver antenna system. The output at the receiver is the weighted sum of the transmitted data, received at each receiver radiator where the weights are assigned by the multi-path environment. This weighted sum of the data transmitted by all the radiators in the transmitter antenna system is decoded using a MIMO algorithm and a priori knowledge of the channel at the receiver.

Multiple channels can be established between the transmitter and receiver only if each radiator of the antenna system is independent of the neighbouring radiators. If they are not independent then the signal received by multiple radiators will have high correlation and hence independent channels cannot be established. The correlation between the received signals can be significantly decreased by increasing the electrical length between the radiators. However for compact systems, it is not possible to place the radiators far apart due to the space constraints. So different methods are required to increase the isolation between the closely packed radiating elements in an antenna system.

Different isolation enhancement techniques are studied in this work. Four different techniques are applied to a 4-shaped printed dual-band dual-element MIMO antenna system. The effectiveness of these techniques is discussed based on the performance metrics used to benchmark MIMO antenna systems. These techniques were divided into two major categories. The first category, that is discussed in Chapter 5, covers non-metamaterial based isolation enhancement structures. Two techniques are discussed in this category. The first is a Defected Ground structure (DGS) based isolation enhancement structure and the other is based on the use of a neutralization line. The results show that the DGS based structure is effective at both bands of operation whereas the neutralization based isolation enhancement technique is effective only in the high band. In case of the DGS based isolation enhancement structure, the isolation improved from $9.5dB$ to $17dB$ in the low band. Similarly for high, band the isolation improvement went

from $7.1dB$ to $9dB$. This proves that the isolation enhancement structure covers both bands of operation for the 4-shaped MIMO antenna system. Other MIMO antenna performance metrics were evaluated such as TARC, correlation coefficient and MEG.

The neutralization line techniques is effective only in the high band. The reason lies in the radiation mechanism of the antenna system. The neutralization line cancels the localized currents induced by adjacent radiating elements. These currents lower the isolation and increase the correlation coefficients. In case of the 4-shaped MIMO antenna system operating in the low band, the induced currents are not localized. At this frequency the ground plane also plays significant role in radiation. So the ground plane currents should be altered to enhance isolation at this frequency. The neutralization line cannot modify the ground plane currents. This is why the DGS is more effective as compared to the neutralization line.

The second category covers the isolation techniques that are based on metamaterials. In this category, two different techniques are studied. The first technique utilizes capacitively loaded loops (CLLs) based metamaterial to suppress the coupling signal. In the second technique, a magnetic wall is realized using a metamaterial and its effect is studied on the isolation enhancement for a 4-shaped MIMO antenna system. The CLL based metamaterial is an unbalanced metamaterial that provides band gaps. A band gap is a frequency range that cannot allow signal propagation through the material. So if properly designed, a metamaterial placed between the radiating elements can suppress the coupling.

The second technique realizes a magnetic wall between the radiators. The magnetic wall that is realized using a metamaterial, suppresses the coupling magnetic fields. The results show that the magnetic wall based isolation structure is not effective for the 4-shaped MIMO antenna system. Observation of the coupling signals show that the magnetic field does not contribute in coupling signals. So blocking magnetic field has no effect on the MIMO antenna performance. The minimum isolation enhancement for the CLL based metamaterial was $9dB$ in low band and $2dB$ in high band while no significant improvement was obtained from the magnetic wall.

7.1 Future Work

Some future work that can extend the results obtained in this work can be:

1. Testing the proposed isolation technique on a four element MIMO antenna system that fit within the $100 \times 50 \times 1.56mm^3$ substrate.
2. Investigate active MIMO antenna elements and come up with new isolation enhancement techniques.
3. Apply the proposed isolation structures on different antenna geometries and types and assess their performance.

REFERENCES

- [1] C. E. Shannon, “Communication in the presence of noise,” *Institute of Radio Engineers*, vol. 37, no. 1, pp. 10–21, Jan. 1947.
- [2] R. Mathar and A. Schmeink, “Increasing signaling power not necessarily improves channel capacity,” in *International conference on signal processing and communication systems (ICSPCS)*, 2010, pp. 1–5.
- [3] V. Hinostroza and S. Salous, “Frequency Selective Fading on Wideband Mobile Radio Channels,” in *IEEE Vehicular Technology Conference*. IEEE, Sep. 2006, pp. 1–4.
- [4] D. Gesbert, M. Shafi, P. Smith, and A. Naguib, “From theory to practice: an overview of MIMO space-time coded wireless systems,” *IEEE Journal on Selected Areas in Communications*, vol. 21, no. 3, pp. 281–302, Apr. 2003.
- [5] M. Sharawi, M. Jan, and D. Aloï, “Four-shaped 2x2 multi-standard compact multiple-inputmultiple-output antenna system for long-term evolution mobile handsets,” *IET Microwaves, Antennas & Propagation*, vol. 6, no. 6, p. 685, 2012.

- [6] S. Blanch, J. Romeu, and I. Corbella, “Exact representation of antenna system diversity performance from input parameter description,” *Electronics Letters*, vol. 39, no. 9, p. 705, 2003.
- [7] P. Hallbjorner, “The Significance of Radiation Efficiencies When Using S-Parameters to Calculate the Received Signal Correlation From Two Antennas,” *Antennas and Wireless Propagation Letters*, vol. 4, no. 1, pp. 97–99, Dec. 2005.
- [8] M. Pelosi, M. Knudsen, and G. Pedersen, “Multiple antenna systems with inherently decoupled radiators,” *Antennas and Propagation, IEEE Transactions on*, vol. 60, no. 2, pp. 503–515, feb. 2012.
- [9] J. Nielsen, G. Pedersen, K. Olesen, and I. Kovacs, “Computation of mean effective gain from 3D measurements,” in *1999 IEEE 49th Vehicular Technology Conference (Cat. No.99CH36363)*, vol. 1. IEEE, pp. 787–791.
- [10] T. Taga, “Analysis for mean effective gain of mobile antennas in land mobile radio environments,” *IEEE Transactions on Vehicular Technology*, vol. 39, no. 2, pp. 117–131, May 1990.
- [11] A. Ando, T. Taga, A. Kondo, K. Kagoshima, and S. Kubota, “Mean Effective Gain of Mobile Antennas in Line-of-Sight Street Microcells With Low Base Station Antennas,” *IEEE Transactions on Antennas and Propagation*, vol. 56, no. 11, pp. 3552–3565, Nov. 2008.

- [12] A. Alayon Glazunov, A. Molisch, and F. Tufvesson, “Mean effective gain of antennas in a wireless channel,” *IET Microwaves, Antennas & Propagation*, vol. 3, no. 2, p. 214, 2009.
- [13] M. Manteghi and Y. Rahmat-Samii, “Broadband characterization of the total active reflection coefficient of multiport antennas,” in *IEEE Antennas and Propagation Society International Symposium*, vol. 3. IEEE, pp. 20–23.
- [14] S.-W. Su, C.-T. Lee, and F.-S. Chang, “Printed MIMO-Antenna System Using Neutralization-Line Technique for Wireless USB-Dongle Applications,” *IEEE Transactions on Antennas and Propagation*, vol. 60, no. 2, pp. 456–463, Feb. 2012.
- [15] Z. Li, Z. Du, M. Takahashi, K. Saito, and K. Ito, “Reducing Mutual Coupling of MIMO Antennas With Parasitic Elements for Mobile Terminals,” *IEEE Transactions on Antennas and Propagation*, vol. 60, no. 2, pp. 473–481, Feb. 2012.
- [16] J. B.-A. Rodney Vaughan, *Channels, Propagation and Antennas for Mobile Communications*. IET Digital Library.
- [17] D. Yuan, Z. Du, K. Gong, and Z. Feng, “A novel dual-band printed diversity antenna for mobile terminals,” *Antennas and Propagation, IEEE Transactions on*, vol. 55, no. 7, pp. 2088–2096, July.
- [18] C. A. Balanis, *Antenna Theory: Analysis and Design, 3rd Edition*. Wiley-Interscience, 2005.

- [19] H. Carrasco, H. D. Hristov, R. Feick, and D. Cofre, “Mutual coupling between planar inverted-F antennas,” *Microwave and Optical Technology Letters*, vol. 42, no. 3, pp. 224–227, Aug. 2004.
- [20] K.-L. Wong, J.-H. Chou, S.-W. Su, and C.-M. Su, “Isolation between GSM/DCS and WLAN antennas in a PDA phone,” *Microwave and Optical Technology Letters*, vol. 45, no. 4, pp. 347–352, May 2005.
- [21] I. Yeom, J. Kim, and C. Jung, “Compact dual-band mimo antenna with high isolation performance,” in *Microwave Conference Proceedings (APMC), 2010 Asia-Pacific*, dec. 2010, pp. 766 –769.
- [22] M. K. T. Al-Nuaimi and W. G. Whittow, “Performance investigation of a dual element IFA array at 3 GHz for MIMO terminals,” in *2011 Loughborough Antennas & Propagation Conference*. IEEE, Nov. 2011, pp. 1–5.
- [23] C. Volmer, J. Weber, R. Stephan, K. Blau, and M. A. Hein, “An Eigen-Analysis of Compact Antenna Arrays and Its Application to Port Decoupling,” *IEEE Transactions on Antennas and Propagation*, vol. 56, no. 2, pp. 360–370, 2008.
- [24] J. Andersen and H. Rasmussen, “Decoupling and descattering networks for antennas,” *IEEE Transactions on Antennas and Propagation*, vol. 24, no. 6, pp. 841–846, Nov. 1976.
- [25] S.-C. Chen, Y.-S. Wang, and S.-J. Chung, “A Decoupling Technique for Increasing the Port Isolation Between Two Strongly Coupled Antennas,” *IEEE*

- Transactions on Antennas and Propagation*, vol. 56, no. 12, pp. 3650–3658, Dec. 2008.
- [26] R. Bhatti, “Compact Antenna Array With Port Decoupling for LTE-Standardized Mobile Phones,” *IEEE Antennas and Wireless Propagation Letters*, vol. 8, pp. 1430–1433, 2009.
- [27] Seongryong Yoo and Sungtek Kahng, “A Compact MIMO Antenna using ZOR Split Ring Resonator Radiators with a Decoupling Structure,” *Microwave Journal*, vol. 54, pp. S26–S31, 2011.
- [28] A. Mak, C. Rowell, and R. Murch, “Isolation enhancement between two closely packed antennas,” *Antennas and Propagation, IEEE Transactions on*, vol. 56, no. 11, pp. 3411–3419, nov. 2008.
- [29] K.-s. Min, D.-J. Kim, and Y.-M. Moon, “Improved MIMO Antenna by Mutual Coupling Suppression Between Elements,” in *The European Conference on Wireless Technology, 2005*. IEEE, pp. 135–138.
- [30] C.-H. Lee, S.-Y. Chen, and P. Hsu, “Integrated Dual Planar Inverted-F Antenna With Enhanced Isolation,” *IEEE Antennas and Wireless Propagation Letters*, vol. 8, pp. 963–965, 2009.
- [31] T.-W. Kang and K.-L. Wong, “Isolation improvement of WLAN internal laptop computer antennas using dual-band strip resonator,” in *2009 Asia Pacific Microwave Conference*. IEEE, Dec. 2009, pp. 2478–2481.

- [32] C.-Y. Chiu, C.-H. Cheng, R. D. Murch, and C. R. Rowell, "Reduction of Mutual Coupling Between Closely-Packed Antenna Elements," *IEEE Transactions on Antennas and Propagation*, vol. 55, no. 6, pp. 1732–1738, Jun. 2007.
- [33] D. Ahn and T. Itoh, "High isolation dual-polarized patch antenna using integrated defected ground structure," *IEEE Microwave and Wireless Components Letters*, vol. 14, no. 1, pp. 4–6, Jan. 2004.
- [34] F. Zhu, J. Xu, and Q. Xu, "Reduction of mutual coupling between closely-packed antenna elements using defected ground structure," in *2009 3rd IEEE International Symposium on Microwave, Antenna, Propagation and EMC Technologies for Wireless Communications*. IEEE, Oct. 2009, pp. 1–4.
- [35] H. Li, J. Xiong, and S. He, "A compact planar mimo antenna system of four elements with similar radiation characteristics and isolation structure," *Antennas and Wireless Propagation Letters, IEEE*, vol. 8, pp. 1107 –1110, 2009.
- [36] A. K. Arya, A. Patnaik, and M. V. Kartikeyan, "A compact array with low mutual coupling using defected ground structures," in *2011 IEEE Applied Electromagnetics Conference (AEMC)*. IEEE, Dec. 2011, pp. 1–4.
- [37] J.-F. Li, Q.-X. Chu, and T.-G. Huang, "A Compact Wideband MIMO Antenna With Two Novel Bent Slits," *IEEE Transactions on Antennas and Propagation*, vol. 60, no. 2, pp. 482–489, Feb. 2012.

- [38] A. Habashi, J. Nourinia, and C. Ghobadi, "A rectangular defected ground structure (DGS) for reduction of mutual coupling between closely-spaced microstrip antennas," in *20th Iranian Conference on Electrical Engineering (ICEE2012)*. IEEE, May 2012, pp. 1347–1350.
- [39] A. Diallo, C. Luxey, P. Le Thuc, R. Staraj, and G. Kossiavas, "Study and Reduction of the Mutual Coupling Between Two Mobile Phone PIFAs Operating in the DCS1800 and UMTS Bands," *IEEE Transactions on Antennas and Propagation*, vol. 54, no. 11, pp. 3063–3074, Nov. 2006.
- [40] S. Ranvier, C. Luxey, P. Suvikunnas, R. Staraj, and P. Vainikainen, "Capacity enhancement by increasing both mutual coupling and efficiency: a novel approach," in *2007 IEEE Antennas and Propagation International Symposium*. IEEE, Jun. 2007, pp. 3632–3635.
- [41] Z. Li, M.-S. Han, X. Zhao, and J. Choi, "MIMO antenna with isolation enhancement for wireless USB dongle application at WLAN band," in *Asia-Pacific Microwave Conference Proceedings (APMC)*, 2010, pp. 758–761.
- [42] Y. Lee, H. Chung, J. Ha, and J. Choi, "Design of a MIMO antenna with improved isolation using meta-material," in *2011 International Workshop on Antenna Technology (iWAT)*. IEEE, Mar. 2011, pp. 231–234.
- [43] K. Sarabandi and Y. J. Song, "Subwavelength Radio Repeater System Utilizing Miniaturized Antennas and Metamaterial Channel Isolator," *IEEE*

- Transactions on Antennas and Propagation*, vol. 59, no. 7, pp. 2683–2690, Jul. 2011.
- [44] H. S. Lee and H. M. Lee, “Isolation improvement between loop antennas with absorber cells,” in *2011 IEEE International Symposium on Antennas and Propagation (APSURSI)*. IEEE, Jul. 2011, pp. 1735–1738.
- [45] C.-C. Hsu, K.-H. Lin, H.-L. Su, H.-H. Lin, and C.-Y. Wu, “Design of MIMO antennas with strong isolation for portable applications,” in *2009 IEEE Antennas and Propagation Society International Symposium*. IEEE, Jun. 2009, pp. 1–4.
- [46] Youngki Lee, Deukhyeon Ga and J. Choi, “Design of a MIMO Antenna with Improved Isolation Using MNG Metamaterial,” *International Journal of Antennas and Propagation*, vol. 2012, Jul. 2012.
- [47] M. A. Jan, D. N. Aloï, and M. S. Sharawi, “A 2x1 compact dual band MIMO antenna system for wireless handheld terminals,” in *2012 IEEE Radio and Wireless Symposium*. IEEE, Jan. 2012, pp. 23–26.
- [48] C. Oikonomopoulos-Zachos and B. Rembold, “On the realization of 4-port antennas for MIMO antenna systems,” in *3rd European Conference on Antennas and Propagation*, 2009, pp. 1123–1126.
- [49] M. Zhou, C.-m. Tong, S.-h. Fu, L.-n. Wu, and X.-m. Li, “A novel spiral defected ground structure and its application to the design of dual bandstop

- filter,” in *2010 International Symposium on Signals, Systems and Electronics*.
IEEE, Sep. 2010, pp. 1–3.
- [50] Y. Yu, J. Ji, W. Seong, and J. Choi, “A compact mimo antenna with improved isolation bandwidth for mobile applications,” *Microwave and Optical Technology Letters*, vol. 53, no. 10, pp. 2314–2317, 2011.
- [51] Z. Wu, J. Zhu, M. Jia, H. Lu, and B. Zeng, “A double-layer metamaterial with negative refractive index originating from chiral configuration,” *Microwave and Optical Technology Letters*, vol. 53, no. 1, pp. 163–166, Jan. 2011.
- [52] S. N. Burokur, M. Latrach, and S. Toutain, “Study of the effect of dielectric split-ring resonators on microstrip-line transmission,” *Microwave and Optical Technology Letters*, vol. 44, no. 5, pp. 445–448, Mar. 2005.
- [53] S. Hrabar, Z. Eres, and J. Bartolic, “Capacitively Loaded Loop as Basic Element of Negative Permeability Meta-material,” in *32nd European Microwave Conference, 2002*. IEEE, Oct. 2002, pp. 1–4.
- [54] Y. Guo and R.-M. Xu, “PLANAR METAMATERIALS SUPPORTING MULTIPLE LEFT-HANDED MODES,” *Progress In Electromagnetics Research*, vol. 66, pp. 239–251, 2006.
- [55] G. Goussetis, A. P. Feresidis, S. Wang, Y. Guo, and J. C. Vardaxoglou, “Uniplanar left-handed artificial metamaterials,” *Journal of Optics A: Pure and Applied Optics*, vol. 7, no. 2, p. S44, 2005.

- [56] G. Goussetis, A. Feresidis, and J. Vardaxoglou, “Efficient modeling of novel uniplanar left-handed metamaterials,” *IEEE Transactions on Microwave Theory and Techniques*, vol. 53, no. 4, pp. 1462–1468, Apr. 2005.
- [57] C. Caloz and T. Itoh, *Electromagnetic Metamaterials: Transmission Line Theory and Microwave Applications*. Wiley-IEEE Press, 2005.
- [58] HFSS, “Left-Handed Material Design Guide,” Tech. Rep.
- [59] J. D. Joannopoulos, S. G. Johnson, J. N. Winn, and R. D. Meade, *Photonic Crystals: Molding the Flow of Light (Second Edition)*. Princeton University Press, 2008.
- [60] Y. Guo, G. Goussetis, A. Feresidis, and J. Vardaxoglou, “Efficient modeling of novel uniplanar left-handed metamaterials,” *IEEE Transactions on Microwave Theory and Techniques*, vol. 53, no. 4, pp. 1462–1468, 2005.

Vitae

- Name: Ahmed Bilal Numan
- Nationality: Pakistan
- Date of Birth: 26-June-1987
- Email: *numan252@yahoo.com*
- Permenant Address: 138-B Phase III G.E.C.H.S., Model Town Link Road,
Lahore, Pakistan